Title

High-Pressure Behavior and Chemical Reactions of Volatile-Bearing Minerals in Earth's Mantle

Permalink

https://escholarship.org/uc/item/5df7q493

Author

Sawchuk, Krista Lynn Sierra

Publication Date

2021

Peer reviewed|Thesis/dissertation

UNIVERSITY OF CALIFORNIA

Los Angeles

High-Pressure Behavior and Chemical Reactions of

Volatile-Bearing Minerals in Earth's Mantle

A dissertation submitted in partial satisfaction of the

requirements for the degree Doctor of Philosophy

in Geochemistry

by

Krista Lynn Sierra Sawchuk

2021

ABSTRACT OF THE DISSERTATION

High-Pressure Behavior and Chemical Reactions of

Volatile-Bearing Minerals in Earth's Mantle

by

Krista Lynn Sierra Sawchuk

Doctor of Philosophy in Geochemistry

University of California, Los Angeles, 2021

Professor Abby Kavner, Chair

The deep Earth volatile cycle has far-reaching impacts on the atmosphere, climate, hydrologic cycle, and biosphere of our planet. Volatile species in minerals are exchanged between Earth's surface and interior. Earth's interior contains the largest reservoir of volatiles on the planet. However, our understanding of this reservoir is limited. The deep Earth cannot be directly sampled, so we rely on models and laboratory experiments to simulate analogous conditions. Prior experiments have determined equations of state and the phase stabilities of many abundant mineral species at deep Earth conditions, however less work has been done on volatile-bearing minerals. Determining the behavior of volatile-bearing minerals using high pressure and temperature experiments can resolve which mineral phases store volatiles in the deep Earth. These experiments give additional insight into chemical processes in the deep Earth, and will help to shed light on the formation and chemical evolution of our planet.

In this dissertation, I use Raman and infrared spectroscopy to investigate the high-pressure behavior of the lead sulfate, anglesite ($PbSO_4$), in the diamond anvil cell. This work gives insights into the behavior of sulfates, commonly subducted sulfur-bearing minerals, at mantle pressures. I produce the first high-pressure infrared spectroscopy measurements on anglesite, extend the pressure range studied with Raman spectroscopy, and discover a previously unknown phase transition.

I make measurements of the bulk modulus and its pressure derivative for anglesite using X-ray diffraction and the Birch-Murnaghan equation of state. This study confirms previous observations of a phase transition in anglesite and produces a thorough X-ray diffraction dataset to 50 GPa.

Using X-ray diffraction and Raman spectroscopy, I measure the bulk modulus and Grüneisen parameters of the nickel carbonate, gaspéite ($NiCO_3$). These experiments produce the first high-pressure Raman measurements on gaspéite and greatly extend the pressure range studied with X-ray diffraction. This work reveals systematic trends among the transition metal carbonates: gaspéite, having the smallest cation radius, is the most stable at high pressures.

To aid our understanding of the relative phase stability of mantle minerals, I perform a pioneering set of experiments to determine the reaction products of CO_2 and manganese metal. The results of these experiments inform us of the relative stabilities between carbonates and oxides and give insights into minerals that could store carbon in the deep Earth.

The dissertation of Krista Lynn Sierra Sawchuk is approved.

Craig Manning

Edwin Schauble

Mackenzie Day

Abby Kavner, Committee Chair

University of California, Los Angeles

2021

For my family

Table of Contents

List of Tables

Acknowledgements

I thank my advisor, Abby Kavner, for her guidance throughout my PhD and for helping me develop into a better scientist.

Thanks to my colleague, Chris McGuire, for help with data analysis, running experiments, and for always being there to give me support and advice. Thanks to Elise Knittle and Quentin Williams who started my mineral physics career in their lab at UCSC, I am grateful for the all the guidance they have given me. Thanks to Cara Vennari and Earl O'Bannon for their mentorship during my time at the UCSC mineral physics lab and for their continued support. Thanks to Rupini Kamat for help with running experiments. I am grateful to the beamline scientists: Martin Kunz, Andrew Doran, Eran Greenberg, Vitali Prakapenka, and Sergey Tkachev whose support at their respective beamlines made my research possible. I thank my committee members for their advice and guidance throughout my projects. Thanks to Craig Manning for helpful advice about my projects and life in general. Thanks to Lars Stixrude for constructive discussions about my projects. Thanks to the friends and colleagues in the Earth, Planetary, and Space Sciences department for their camaraderie and enjoyable discussions. I am especially grateful for the friendship and support I received from Ashley Schoenfeld, Heather Kirkpatrick, and Ashna Aggarwal, passionate women in science who were a constant source of inspiration to me.

I thank my parents for fostering my curiosity and interest in geology. I am grateful for their continuous love and support. I would not be where I am today without them.

Thank you Jason, for your support, kindness, and encouragement. I am grateful for the discussions about my research, manuscript edits, and the adventures that allowed me to escape to the outdoors when I needed a break. You made achieving this PhD immensely more enjoyable.

A version of Chapter 2 was published as: "An infrared and Raman spectroscopic study of PbSO4-anglesite at high pressures" by K. Sawchuk, E.F. O'Bannon, C. Vennari, A. Kavner, E. Knittle, & Q. Williams, (2019), Physics and Chemistry of Minerals

A version of Chapter 3 is being prepared for submission as: "An X-Ray Diffraction Study of High-Pressure and Temperature Structural Changes of Anglesite ($PbSO_4$)" by K. Sawchuk, C. McGuire, and A. Kavner

A version of Chapter 4 was published as: "An X-ray diffraction and Raman spectroscopic study of the high-pressure behavior of gaspéite ($Ni_{0.73}$,$Mg_{0.27}CO_3$)" by K. Sawchuk, R. Kamat, C. McGuire, & A. Kavner, (2021), Physics and Chemistry of Minerals

A version of Chapter 5 is being prepared for submission as: "High Pressure and Temperature Reactions of Manganese Metal and CO_2" by K. Sawchuk, C. McGuire, and A. Kavner

Vita

2019   C. Phil., Geochemistry, UCLA, Los Angeles, California

2017-2021   Graduate Student Researcher, UCLA. Equation of state measurements in the diamond anvil cell. Experiments performed at the Advanced Light Source, Berkeley National Lab and Advanced Photon Source, Argonne National Lab

2016-2020   Teaching Assistant. Earth, Planetary, and Space Sciences Department, UCLA. Taught lab and discussion sections

2016   B.A., Earth Sciences, Departmental Honors, University of California, Santa Cruz, California

Publications

McGuire C, **Sawchuk K**, Kavner A (2018) Measurements of thermal conductivity across the B1-B2 phase transition in NaCl. Journal of Applied Physics 124 (11), 115902

Sawchuk K, O'Bannon EF, Vennari C, Kavner A, Knittle E, Williams Q (2019) An infrared and Raman spectroscopic study of PbSO4-anglesite at high pressures. Physics and Chemistry of Minerals 46 (6), 623-637

Sawchuk K, Kamat R, McGuire C, Kavner A (2021) An X-ray diffraction and Raman spectroscopic study of the high-pressure behavior of gaspéite ($Ni_{0.73}$,$Mg_{0.27}CO_3$). Physics and Chemistry of Minerals 48 (7).

Chapter 1 - Introduction

1.1 Overview

The interior of Earth makes up approximately 99% of our planet by volume. It extends

from the base of the crust to the core and is divided into several layers based on mechanical

properties and composition (Figure 1.1). While the interior of Earth, which we will call the deep

Earth, accounts for the vast majority of the planet, we know surprisingly little about it. This is

not without good reason, as its study poses some immense challenges. The extreme pressures and

temperatures that exist within the deep Earth make direct observations of the mineral phases that

exist there nearly impossible. Attempts at drilling into the deep Earth have only achieved depths

of 12.2 km (Smythe et al., 1994). A different approach is needed if we are to learn about the

behavior of mineral phases in the deep Earth. One way to accomplish this is with laboratory

experiments.

To better understand the behavior of Earth materials at deep Earth conditions, we can

simulate those conditions in the lab and make measurements of their material properties. The

high pressures that exist in the deep Earth can be simulated with diamond anvil cells (Figure

1.2). This apparatus uses two diamonds mounted to metal backing plates, which are squeezed

together in axial compression to generate high pressures. The sample is placed between the

diamonds and contained using a metal gasket during experiments. This is an effective way to

generate high pressures because of the relation between pressure and force:

$$Pressure = \frac{Force}{Area}$$

The small surface area of contact between the diamonds, about 250 microns in diameter, allows

high pressures to be generated with relatively little force. The transparency of the diamonds

permits *in situ* investigations of high-pressure behavior using spectroscopic and diffraction techniques. The high temperatures that exist within the Earth can be simulated in the lab using infrared lasers, which can pass through the diamonds and couple with the sample, generating temperatures up to 3000 K.

Laboratory experiments have helped us understand the major mineral phases that comprise the deep Earth (Figure 1.3). From experiments, we know that the mineral olivine, an iron-magnesium silicate and major constituent of the upper mantle, converts to different phases (Figure 1.4) before ultimately breaking down into two separate minerals at lower mantle pressures (Katsura et al., 2004; Ishii et al., 2018; Tsujino et al., 2019). However, while we have a good idea of the major phases that make up the deep Earth, we do not have as good of an understanding of some of the minor phases. The behavior of volatile-bearing mineral species at deep Earth conditions is of particular interest due to their impact on other Earth processes.

1.2 The Deep Earth's Volatile Cycle

Volatiles are elements and molecules that readily vaporize and are an important part of Earth's chemical systems. The volatile cycle has far-reaching impacts on the atmosphere, climate, hydrologic cycle, biosphere, and geologic processes of our planet. Megatonnes of volatile species in minerals, such as SO_4^{2-}, and CO_3^{2-}, are exchanged between the surface and Earth's interior each year (Dasgupta and Hirschmann, 2010; Evans, 2012; Kelemen and Manning, 2015). Volatiles enter the deep Earth through subduction and can be released to the surface through volcanic processes. While the concentration of volatiles in the deep Earth is probably low compared to other reservoirs, the deep Earth's sheer size makes it Earth's largest reservoir. Our understanding of this reservoir of volatiles is limited. Earth's transport and

storage of volatile elements is not well understood and the amount the deep Earth currently

stores is undetermined. We also have only a rudimentary understanding of the specific mineral

phases that store volatiles in the deep Earth. Studying volatile species at mantle and core

conditions will greatly aid in our understanding of the mineral phases that store volatiles in the

deep Earth.

In order to improve our understanding of volatile-bearing mineral species in the deep

Earth, we must make thermodynamic measurements of both the formation of volatile-bearing

minerals and their properties. In this dissertation, I focus on two important volatile elements:

carbon and sulfur. I present measurements of the high-pressure behavior of previously unstudied

volatile-bearing mineral species, and novel measurements of reactions between volatile species

and transition metals.

1.3 Sulfur in the Deep Earth

Sulfur is an abundant volatile element and is important to life on Earth. Its presence in the

atmosphere affects the climate and it is necessary for life as a component in amino acids. Sulfur

also plays a critical role in geologic processes such as volcanic activity, the formation of ore

deposits, and the redox state of the mantle (Evans et al., 2014; Li et al, 2018; Li et al., 2020). In

minerals, sulfur commonly takes the form of sulfides or sulfates. These sulfur-bearing minerals

enter the deep Earth via the subduction of tectonic plates; sulfur can then be released back to the

surface through volcanic activity, or accumulate in the deep Earth. Both sulfides and sulfates are

found in subducting slabs. In the deep Earth, sulfur is thought to reside primarily as sulfide

mineral phases, however, it is thought that sulfates, such as anhydrite, are present in large

enough quantities in subducting slabs to play a major role in sulfur contribution to the mantle

(Fujii et al., 2016; Li et al, 2018; Chowdhury & Dasgupta, 2020). It is likely that more sulfur ends up sequestered in the deep Earth than is released, creating a deep Earth sulfur reservoir (Evans, 2012; Evans et al., 2014). Evans (2012) estimates 77 megatonnes of sulfur are added to the mantle every year (Figure 1.5).

Once sulfate minerals enter the deep Earth through subduction, their behavior is not well understood. One hypothesis is that sulfates, once subducted, will quickly release the bulk of their sulfur back to the surface (Tomkins and Evans, 2015). However, sulfates have been found in diamond inclusions, suggesting that some sulfates survive subduction and persist into the mantle (Wirth et al., 2009). To determine the fate of subducted sulfates, we need to understand how they behave under high pressures. In Chapter 2, I use infrared and Raman spectroscopy to study the high-pressure behavior of the lead sulfate anglesite as an analogue for other baryte-structured sulfates. In Chapter 3, I continue the high-pressure study of anglesite using X-ray diffraction and determine its high-pressure phase.

1.4 Carbon in the Deep Earth

Carbon plays many important roles on the surface of our planet. As CO_2 and CH_4, it traps heat in the atmosphere, helping to regulate the planet's climate. Carbon's ability to form a variety of bonds led to its becoming a basic building block of life. Without carbon, Earth would likely be uninhabitable and devoid of life. Carbon is important for many geologic processes as well. Earth's surface contains many carbon-bearing mineral species. Of these, oxidized carbonate species are common. One example is calcite ($CaCO_3$), which belongs to the carbonate group of minerals and is a primary component of limestone; an abundant ocean floor sediment (Manning et al., 2013). Carbonate minerals are carried into the deep Earth through the

subduction of oceanic crust and can be released back to the surface through volcanism. There is

general consensus that not all the subducted carbon is released back to the surface: some

becomes sequestered in the deep Earth (Dasgupta and Hirschmann, 2010; Kelemen and

Manning, 2015). Dasgupta and Hirchmann (2010) estimate the amount of carbon added to the

deep Earth to be 24-48 megatonnes of carbon per year while Kelemen and Manning (2015)

estimate between 0.0001-52 megatonnes of carbon per year (Figure 1.6).

We have a poor understanding of carbon cycling in the deep Earth: the mineral phases

that store carbon, how they cycle, and how they interact with other phases. While the

concentration of carbon in the deep Earth is not well constrained, its presence there can lower

melting temperatures, leading to heterogeneous zones in the mantle and changing the amount of

CO_2 in the atmosphere (Dasgupta and Hirschmann, 2006). The phases that store carbon in the

deep Earth are dependent on oxygen fugacity: they include oxidized phases such as carbonates,

and reduced phases such carbides and diamonds (McCammon, 2005; Dasgupta and Hirschmann,

2006). To better understand the stability of carbon-bearing phases in the deep Earth, high-

pressure and temperature experiments on their behavior and reactions are necessary. In Chapter

4, I study the high-pressure behavior of the nickel carbonate, gaspéite, to better understand phase

stability of carbonates in the mantle. In Chapter 5, I investigate reactions between carbon

dioxide and transition metals to determine relative phase stability between carbonates and

oxides.
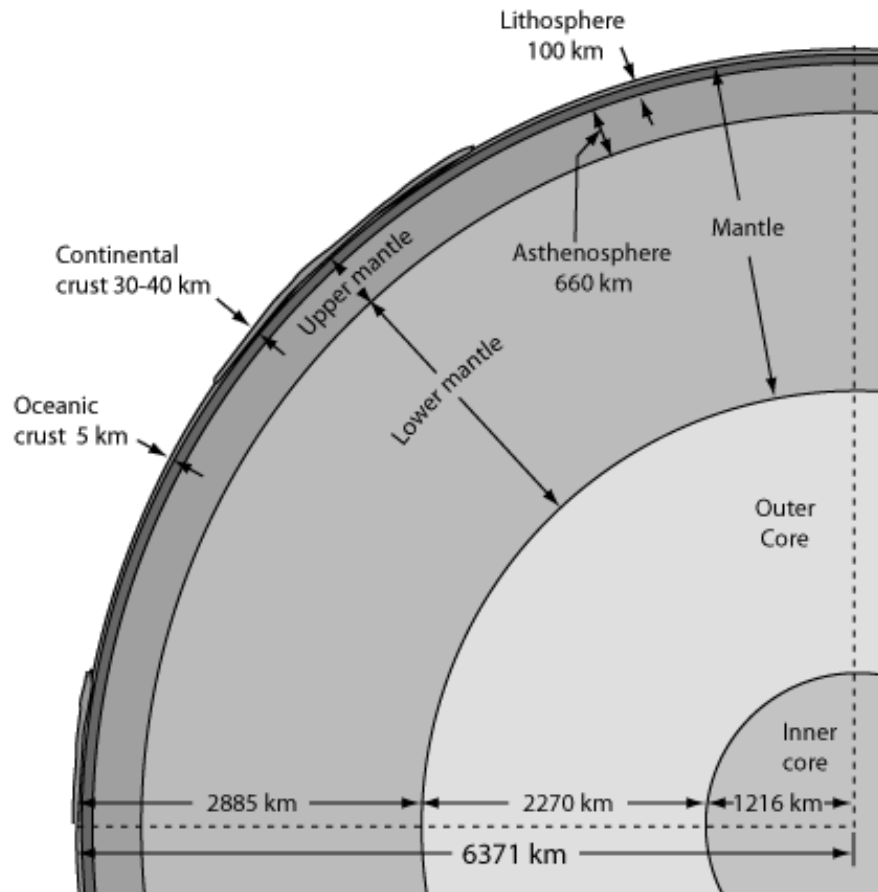
Figure 1.1 Structure of the Earth from Anderson (1989)
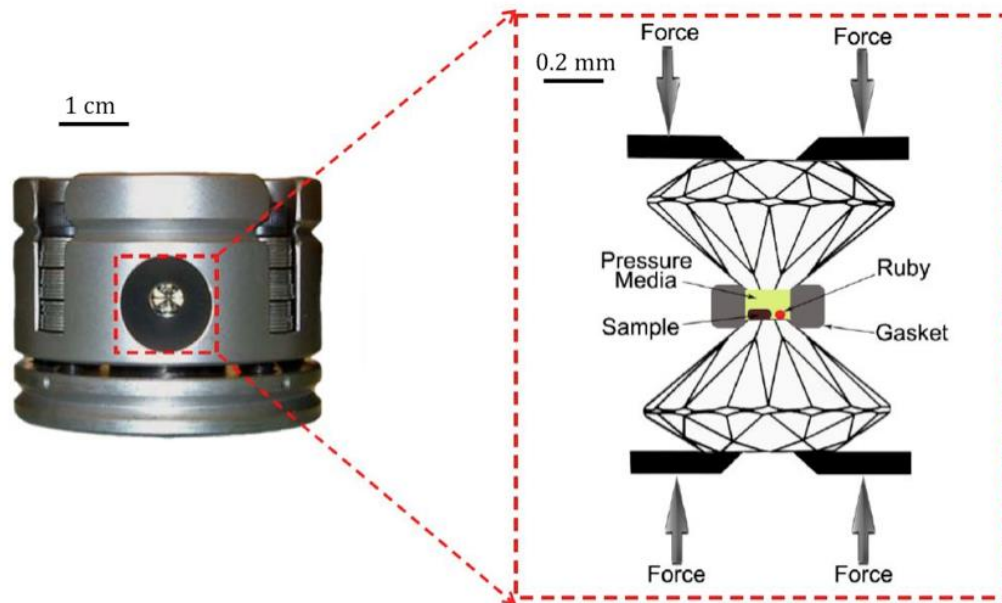
Figure 1.2 Diamond anvil cell schematic by Dong and Song (2011)
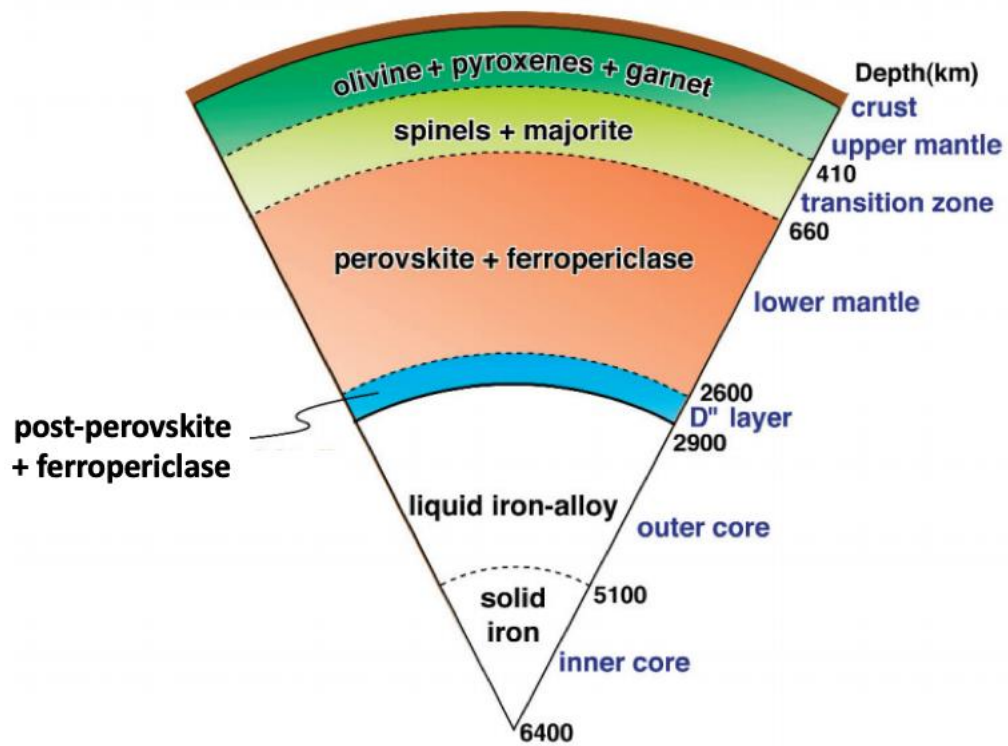
Figure 1.3 Major mineral phases of the deep Earth. Modified from Hirose and Lay (2008)
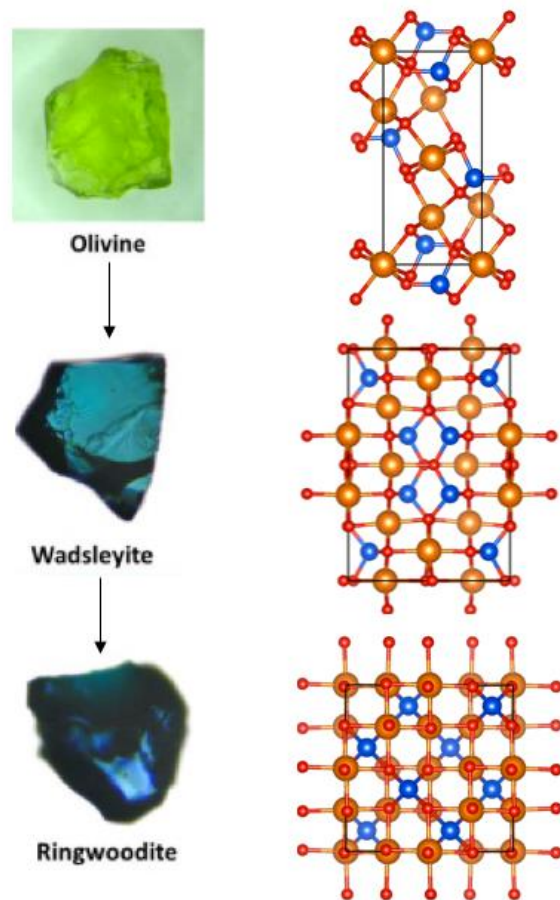
Figure 1.4 Evolution of the olivine structure with increasing pressure. Mineral images from Takaaki Kawazoe. Crystal structures made in VESTA (Momma K and Izumi F, 2011)
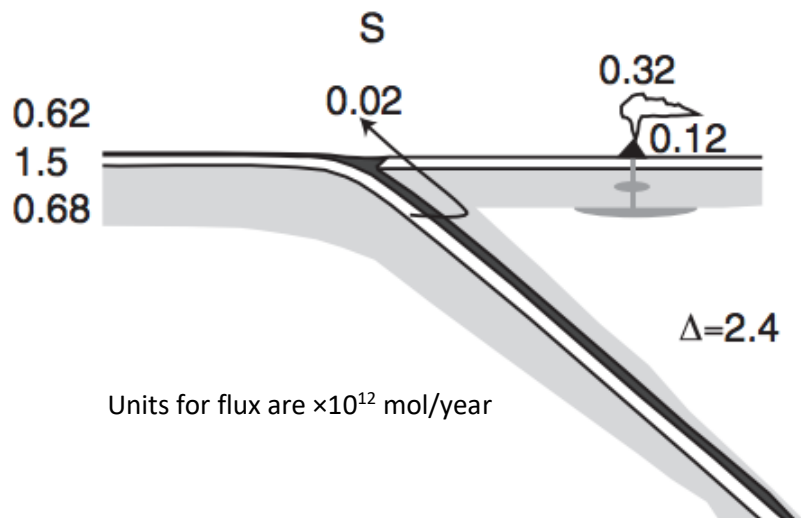
Figure 1.5 Estimates of sulfur fluxes in the deep Earth. Modified from Evans (2012)
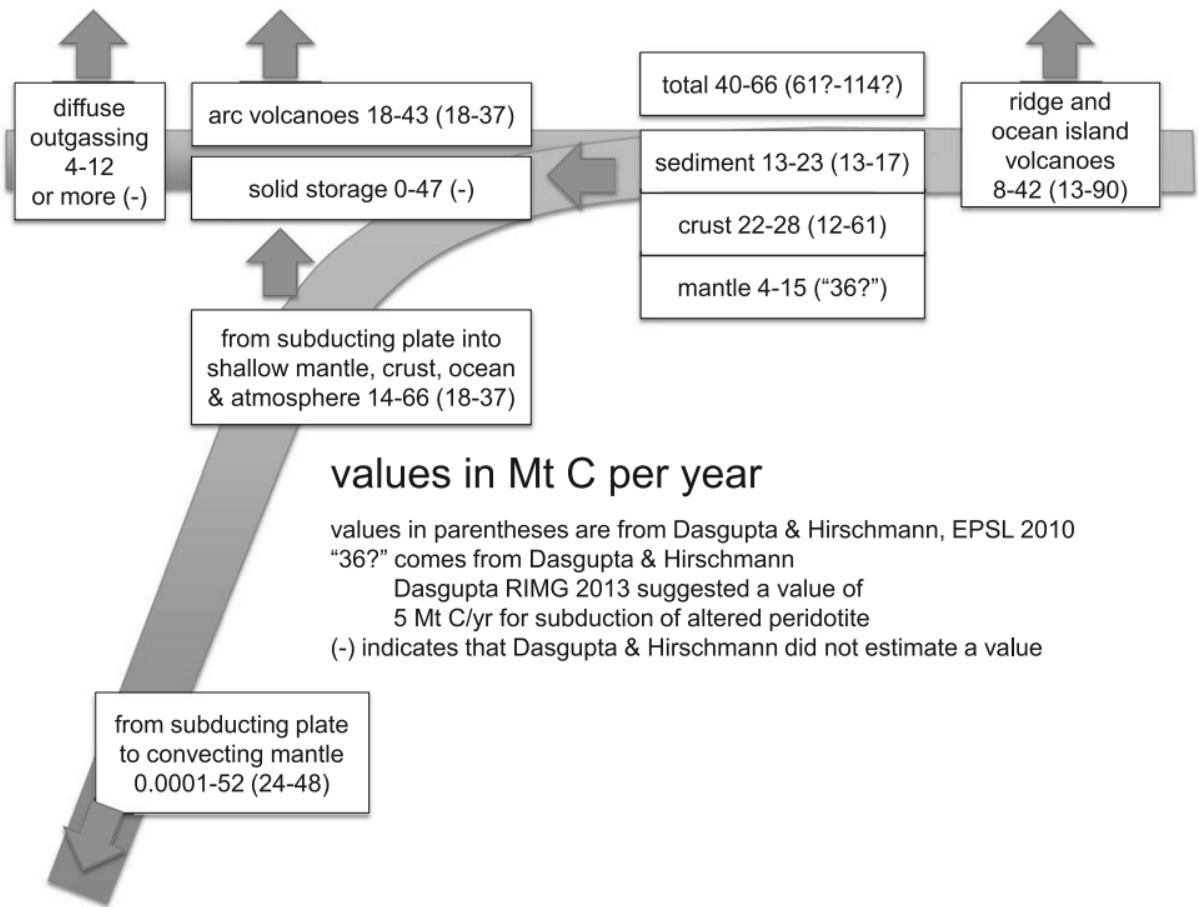
Figure 1.6 Estimates of carbon fluxes in the deep Earth. Figure from Kelemen and Manning (2015)

1.5 References

Anderson D (1989) *New Theory of the Earth*. Cambridge University Press

Chowdhury P and Dasgupta R (2020) Sulfur extraction via carbonated melts from sulfide-
    bearing mantle lithologies – Implications for deep sulfur cycle and mantle redox.
    Geochimica et Cosmochimica Acta 269, 376-397

Dasgupta R and Hirschmann (2006) Melting in the Earth's deep upper mantle caused by carbon
    dioxide. *Nature*, 440, 659-662

Dasgupta R and Hirschmann MM (2010) The deep carbon cycle and melting in Earth's interior.
    Earth and Planetary Science Letters 298: 1-13

Dong Z and Song Y (2011) Novel pressure-induced structural transformations of inorganic
    nanowires. *Nanowires – Fundamental Research*, 10.5772/17084

Evans KA (2012) The redox budget of subduction zones. *Earth-Science Reviews* 113: 11-32.

Evans KA, Tomkins AG, Cliff J, Fiorentini ML (2014) Insights into subduction zone sulfur
    recycling from isotopic analysis of eclogite-hosted sulfides. *Chemical Geology* 365: 1-19.

Fujii T, Ohfuji H, Inoue T, (2016) Phase relation of CaSO4 at high pressure and temperature up
    to 90 GPa and 2300 K. Physics and Chemistry of Minerals, 43(5), 353–361.
    doi:10.1007/s00269-016-0799-4

Hirose K, Lay T (2008) Discovery of post-perovskite and new views on the core-mantle
    boundary region. *Elements*, vol. 4 pp 181-186

Ishii T, Huang R, Fei H, Koemets I, Liu Z, Maeda F, Yuan L, Wang L, Druzhbin D, Yamamoto
    T, Bhat S, Farla R, Kawazoe T, Tsujino N, Kulik E, Higo Y, Tange Y, Katsura T (2018)
    Complete agreement of the post-spinel transition with the 660-km seismic discontinuity.
    Sci Rep 8, 6358, https://doi.org/10.1038/s41598-018-24832-y

Katsura T, Yamda H, Nishikawa O, Song M, Kubo A, Shinmei T, Yokoshi S, Aizawa Y,
Yoshina T, Walter M, Ito E (2004) Olivine-wadsleyite transition in the system
(Mg,Fe)2SiO4. *Journal of Geophysical Research*, vol. 109, B02209

Kelemen P and Manning C (2015) Reevaluation carbon fluxes in subduction zones, what goes
down, mostly comes back up. *Proceedings of the National Academy of Sciences*, 112 (30)
E3997-E4006

Li B, Xu J, Chen W, Ye Z, Huang S, Fan D, Zhou W, Xie H (2018) Compressibility and
expansivity of anglesite ($PbSO_4$) using in situ synchrotron X-ray diffraction at high-
pressure and high-temperature conditions. *Physics and Chemistry of Minerals*:
doi.org/10.1007/s00269-018-0970-1

Li J-L, Schwarzenbach EM, John T, Ague JJ, Huang F, Gao J, Klemd, Whitehouse M, Wang X-
S (2020) Uncovering and quantifying the subduction zone sulfur cycle from the slab
perspective. *Nature Communications*, 11, 514

Manning C, Shock E, Sverjensky D (2013) The chemistry of carbon in aqueous fluids at crustal
and upper-mantle conditions: experimental and theoretical constrains. *Reviews in
Mineralogy and Geochemistry*, vol. 75, pp. 109-148

McCammon C (2005) The paradox of mantle redox. Science, vol. 308, pp. 807-808

Momma K and Izumi F (2011) VESTA 3 for three-dimensional visualization of crystal,
volumetric and morphology data. *J. Appl. Crystallogr* 44: 1272-1276

Smythe DK, Smithson SB, Gillen C, Humphreys C, Kristofferson Y, Karaev NA, Garipov VZ,
Pavlenkova NI (1994) Project images crust, collects seismic data in the world's largest
borehole. Eos, Transactions, *American Geophysical Union*, vol. 75, pg. 473-476

Tomkins A and Evans K (2015) Separate zones of sulfate and sulfide release from subducted

    mafic oceanic crust. *Earth and Planetary Science Letters*, vol. 428, pp. 73-83

Tsujino N, Yoshino T, Yamazaki D, Sakurai M, Sun W, Xu F, Tange Y, Higo Y (2019) Phase

    transition of wadsleyite-ringwoodite in the Mg_2SiO_4-Fe_2SiO_4 system. *American*

    Mineralogist, vol. 104, pgs. 588-594

Wirth R, Kaminsky F, Matsyuk S, Schreiber A (2009) Unusual micro- and nano- inclusions in

    diamonds from the Juina area, Brazil. *Earth and Planetary Science Letters* 289, 292-30,

    doi:10.1016/j.epsl.2009.06.043

Chapter 2 - An Infrared and Raman Spectroscopic Study of PbSO$_4$-Anglesite at High Pressures

2.1 Introduction

Anglesite (PbSO$_4$) is a member of the barite group that forms in acidic lead-bearing ore oxidation zones. The barite structure represents one of the more compactly packed sulfate structures known, with a coordination of lead of between 8 and 12 (Figure 2.1), so its behavior under pressure is relevant because sulfur might be stored in oxidized environments in the earth. In terms of the Earth's sulfur budget, the amount of sulfur subducted into the Earth likely exceeds the amount released from volcanic sources by about an order of magnitude, with the excess plausibly residing in the deep Earth (Evans 2012; Evans et al. 2014). Thus, our interest in this compound is oriented towards determining what structure sulfates relevant to the deep Earth sulfur cycle might ultimately convert to as possible post-barite structures at high pressures. PbSO$_4$ is also of interest because ABX$_4$ materials have applications to materials science that include their usage as scintillation detectors (Errandonea and Majon 2008), and PbSO$_4$ has been demonstrated to have non-linear optical properties (Kaminskii et al. 2011).

Among oxidized sulfates, CaSO$_4$-anhydrite converts to a monazite-structured phase at 300 K and 3 GPa (Bradbury and Williams 2009) prior to converting to a barite-structured phase at high temperatures and pressures above ~ 13 GPa (Fujii et al. 2016). In contrast, BaSO$_4$, which is isostructural with PbSO$_4$, undergoes a sluggish transition between 13 and 27 GPa (depending on pressure medium) to a distorted orthorhombic barite- like post-barite structure with space group $P2_12_12_1$ (Santamaría-Pérez et al. 2011; Santamaría-Pérez and Chuliá-Jordán 2012). Thus, one goal of this study is to constrain likely candidates for the post-barite structure of PbSO$_4$ in particular, and divalent cation-bearing sulfates in general. An additional goal of this study is to

evaluate the role of differing degrees of non-hydrostaticity on pressure-induced transitions in $PbSO_4$.

In terms of its crystal structure, anglesite ($PbSO_4$) has the barite structure, which is orthorhombic with the space group *Pnma* with $Z = 4$. It is comprised of SO_4 tetrahedra with Pb^{2+} in pseudo-eight to twelve-fold coordination with the oxygen ions (Figure 2.1). The coordination of lead in anglesite is highly irregular, with Pb–O distances varying between 2.61(2) and 3.27(1) Å, and the average distance being ~ 2.85 Å (Miyake et al. 1978; Antao 2012). Indeed, the oxygen coordination of Pb in $PbSO_4$ is not unambiguous (Antao 2012): depending on assumed bond-distance thresholds, it can be viewed as 8+4, 10+2 or 12-fold coordinate. The relatively large unit cell gives rise to a relatively complex (and hence rich) vibrational spectrum, with 36 Raman-active and 26 infrared- active vibrations.

Systematic trends of the high-pressure phase transitions of ABX_4 compounds have been characterized as a function of cation/anion radius ratios (Figure 2.2: Fukunaga and Yamaoka 1979; Bastide 1987; Errandonea and Majon 2008; Clavier et al. 2011), and $PbSO_4$ may function as an analogue for the higher pressure behavior of lighter divalent cation-bearing sulfates. Based on these systematics, it appears that $PbSO_4$ might convert to the scheelite structure under compression: given that the lead ion is highly compressible (and hence that the r_A / r_X ratio, where r_A *and* r_X are the radii of the A and X cations, may decrease under compression), there is also the possibility that the monazite structure could be accessed before converting to the scheelite structure. Either transition would be anomalous in that the formal coordination of lead might decrease (going from an irregular 8- to 12-fold coordinate in the *Pnma* $BaSO_4$ structure to eightfold) upon conversion to the high-pressure structure.

Previously, Lee et al. (2013) studied the sulfate vibrational modes of anglesite to 35 GPa using Raman spectroscopy in a 4:1 mixture of methanol:ethanol (M:E) pressure medium. In their study, they propose that a change in compressional mechanism occurs at 14 GPa based on 'kinks' in some modes, and changes in the pressure dependence of a subset of the Raman bands; no new peaks were observed at this pressure. These kinks at 14 GPa involve discontinuous decreases in most mode frequencies by 0 to ~ 5 cm^{-1}. Additionally, they suggest that a phase transition takes place at 21 GPa, where additional peaks associated with the symmetric and antisymmetric SO_4 stretching modes appear. They associate these with the onset of a distortion of the SO_4 tetrahedron caused by increased Pb–O bond strength. In this study, we probe anglesite to 43 GPa using both infrared and Raman spectroscopy to explore the nature of these transitions. More recently, Li et al. (2018) conducted an angle-dispersive powder X-ray diffraction study of $PbSO_4$ to 21.6 GPa using a neon pressure medium, in which monotonic compression of anglesite was observed throughout their pressure range, and no phase transitions were reported. Here, we present a vibrational spectroscopic study that (1) expands the pressure range over which anglesite has been studied; (2) incorporates results from different pressure media to characterize the effects of non-hydrostaticity on transitions in $PbSO_4$; (3) includes low frequency Raman lattice vibrations that were not measured by Lee et al. (2013) and resolves more Raman peaks in the sulfate bending and antisymmetric stretching regions; and (4) reports high-pressure infrared data on $PbSO_4$ for the first time.

2.2 Experimental Methods

The natural single crystals of anglesite used in this study are from Sardinia, Italy and were obtained from the Pendleton Mineral Collection (specimen #6523) at UCSC. Samples were

colorless, transparent, about 5 mm in diameter and coexisted with galena. Because these samples formed from oxidation of galena, the composition of anglesite from this locale is extremely close to stoichiometric (Jacobsen et al. 1998). The sample identity was confirmed using ambient pressure Raman and infrared spectra (Figure 2.3), which are in good agreement with previous measurements (Griffith 1970; Dawson et al. 1977; Lane 2007; Lee et al. 2013).

The high-pressure infrared measurements were collected using a symmetric type diamond anvil cell (DAC) with type IIa diamonds with 350-µm diameter 16-sided culets. The sample of anglesite was ground into power and mixed with spectroscopic-grade CsI in a ratio of 8% anglesite and 92% CsI by weight. The powder was then loaded into a spring steel gasket with a 150-µm hole. Grains of ruby were included in the sample chamber to determine pressure after every pressure increment using the standard ruby fluorescence technique (Mao et al. 1986). Mid-infrared absorbance spectra were collected from 400 to 8500 cm^{-1} to a pressure of ~40 GPa using a Bruker Vertex 70V evacuated Fourier transform infrared spectrometer (FTIR) equipped with a globar source, KBr- beamsplitter and a liquid nitrogen cooled mercury–cadmium–telluride (MCT) detector. All infrared spectra were collected with a resolution of 4 cm^{-1}, and overlapping peaks were deconvolved using the Levenberg–Marquardt algorithm, with peak shapes allowed to vary between Gaussian and Lorentzian. The number of peaks utilized in fits was determined based on the numbers of peaks and shoulders observed in the spectra themselves: this minimalist criterion does not resolve accidentally degenerate modes. However, even single crystal reflectance studies are unable to resolve all the accidentally degenerate modes in barite-structured sulfates (Dawson et al. 1977). Typical pressure variations at peak pressure conditions are estimated to be ± 8% for the infrared experiments and due to the small area of sampling, substantially less for the Raman results.

The high-pressure Raman measurements were collected using a symmetric type DAC with type Ia diamonds with 350-μm diameter 16-sided culets. Single crystals of anglesite were loaded into a spring steel gasket with a 150-μm hole using both 4:1 methanol:ethanol (M:E) and neon as pressure media. 2–5 small grains of ruby were included in the sample chamber to determine pressures using the standard ruby fluorescence technique (Mao et al. 1986). Raman spectra were collected from room pressure to 42.5 GPa using a Horiba LabRam HR Evolution Raman spectrometer with a spectrometer focal length of 800 mm, and an 1800 lines/ mm grating. An excitation wavelength of 633 nm was used to collect spectra from 50 to 1300 cm^{-1} for durations of 40–55 s averaged over 3–5 collections. The resolution of the Raman spectra was ~ 1 cm^{-1}, and spectra were fit using the same algorithms as for the infrared spectra. An Olympus BXFM-ILHS microscope equipped with a 50× long working distance objective was used to focus the laser onto the sample to a spot size of ~ 2 μm. The 4:1 methanol ethanol mixture is known to be hydrostatic up to ~ 10.5 GPa, while neon solidifies at 4.8 GPa, and becomes non-hydrostatic (but with substantially smaller stress gradients than M:E) above 15 GPa (Klotz et al. 2009). Thus, our results span a range of non-hydrostatic environments, with the infrared measurements being the least hydrostatic (conducted in a CsI matrix), and Raman spectra being collected in both M:E and neon matrices.

2.3 Results

2.3.1 Infrared Results

Infrared spectra of anglesite on both compression and decompression and the pressure shifts of the observed infra- red modes are shown in figures 2.4 and 2.5. Pressure shifts of the observed infrared modes are shown in table 2.1. The mid-frequency infrared modes of anglesite

were previously assigned by Dawson et al. (1977) and Lane (2007), with v_1 (the tetrahedral symmetric stretching mode) at 960 cm^{-1}, v_3 (the antisymmetric stretching mode) at 1054 and 1183 cm^{-1}, and v_4 (the antisymmetric bending mode) at 598 and 632 cm^{-1}. The v_2 vibration (the tetrahedral symmetric bend) is both weak in the infrared and at the edge of the spectral range that we measured; therefore, we do not resolve this mode. At ambient pressure, a third band associated with v_4 is observed at 612 cm^{-1}, which is also present in the spectra reported by Lane (2007) as a subtle shoulder.

No deviations from linear pressure shifts are resolved for any bands in the infrared spectra, but splittings, possible discontinuities, and band broadening are observed at high pressures (Figure 2.4). The three v_4 modes that are resolved at room pressure diverge under compression, with the two lower frequency modes having relatively low initial pressure shifts (less than 0.5 cm^{-1}/GPa: Table 2.1), while the higher frequency component shifts at over 1 cm^{-1}/GPa. This greater separation at high pressures is consistent with a larger degree of tetrahedral distortion at high pressures (e.g., Dawson et al. 1977). At ~ 13 GPa, the two low frequency v_4 components shift discontinuously to higher wave-numbers, at nearly the same pressure as discontinuous shifts were observed in prior Raman results within a M:E medium (Lee et al. 2013), while changes in the highest frequency v_4 component are not resolved. Also, at ~ 13 GPa, v_3 clearly splits into two peaks and the pressure shift of v_1 changes (Table 2.1; Figures 2.4, 2.5).

Among the v_4 vibrations, a new peak becomes resolvable at a higher frequency than the original two modes at ~ 29 GPa: its pressure shift indicates that it is produced by a splitting of the highest frequency vibration at ~ 23 GPa (Figure 2.5). Two new v_4 modes are resolved near 33 GPa, one of which lies to the higher frequency side and one to the lower frequency side of the doublet that is at ~ 620 cm^{-1} at room pressure and temperature. Correspondingly, the

antisymmetric stretching mode, v_3, splits into two peaks at ~ 13 GPa and further splits into three distinct peaks at ~ 23 GPa (Figures 2.4, 2.5). In both cases, the new peaks appear at higher frequency, and are initially resolved as lower intensity shoulders. The pressure shifts of these new peaks is typically larger than those at lower pressures (Figure 2.5), implying that sulfate group compaction may become progressively more important at higher pressures. The appearance of these peaks does not appear to be compatible with there being accidental degeneracy of these three peaks at low pressures, and pressure-induced peak separation. For example, if they were accidentally degenerate at low pressures, the first appearance of the intermediate frequency peak should have taken place at substantially lower pressures than 13 GPa (given the respective pressure shifts), but a nearly symmetric v_3 peak is observed near 7 GPa (Figure 2.4). Moreover, of the three group theoretically allowed v_3-associated bands, we resolve two at ambient pressures, with the lower frequency of the two being too weak to track under pressure (Figure 2.5). The relatively weak symmetric stretch, v_1, splits at ~ 23 GPa with a new component growing in at a lower frequency than the original mode. This is similar to the behavior of the main v_1 Raman mode, which is discussed in more detail below. All of the mode shifts and splittings observed in the infrared spectra under compression are reversible on decompression, but with hysteresis (Figure 2.4).

2.3.2 Raman Results

Raman spectra of anglesite were collected on both compression and decompression at room temperature (Figures 2.6, 2.7, 2.8, 2.9, 2.10) in both M:E and neon media. The Raman-active modes of anglesite have been previously assigned by Dawson et al. (1977), Jayasooriya et al. (1991), Alia et al. (2000) and Buzgar et al. (2009), with the v_1 (symmetric stretch of the

$(SO_4)^{-2}$ tetrahedra) mode at 977 cm^{-1}, the v_2 (tetrahedral symmetric bend) mode with two components at 437 and 449 cm^{-1}, the v_3 (tetrahedral antisymmetric stretch) mode with three components at 1051, 1140 and 1157 cm^{-1}, and the v_4 (tetrahedral antisymmetric bend) mode with two components at 617 and 640 cm^{-1}. We also observe an additional v_4-associated band at 606 cm^{-1}, in accord with the previous results of Lee et al. (2013). Additionally, six ambient pressure lattice modes are tracked under pressure in the barite- structured phase.

The frequencies of all observed Raman modes increase with pressure (Figures 2.6, 2.7, 2.8, 2.9, 2.10). Some peak broadening is observed in both media: this is more pronounced for the low frequency modes in a M:E medium. This broadening may be due to the initial distortion of the SO$_4$ tetrahedron becoming more pronounced with increasing pressure, a loss of accidental degeneracy of modes as pressure is increased, or non-hydrostatic effects. Many bands show non-linear shifts: we fit the pressure shifts quadratically, and present results on modes shifts from the experiments in neon media in table 2.2. Our absolute mode positions are in good agreement with those of Lee et al. (2013), although our quadratic fits shift the low-pressure slopes relative to their linear fits. Mode Grüneisen parameters are also presented in table 2.2, and are calculated using a bulk modulus of 59 GPa (Li et al. 2018): these show the typical decrease in mode Grüneisen parameter with increasing mode frequency. As described below, the pressure shifts in neon likely reflect those solely of the barite-structured phase. As with the infrared spectral results, the peak positions and splittings are reversible on decompression, although the changes at 23 GPa show substantial hysteresis, with some new bands associated with the high-pressure spectra persisting down to as low as ~ 10 GPa, such as a new v_2 mode (Figure 2.7a). The shapes of bands may differ on decompression: whether samples remain single crystals and preserve their orientation is unknown, and such shifts could alter band shapes on decompression.

Low frequency Raman modes associated with Pb-SO$_4$ translations and SO$_4$ rotational vibrations are shown in figure 2.6a, c within both M:E and neon media, and their Raman shifts are plotted as a function of pressure in figure 2.6b, d. Within the M:E medium, a shift in the intensity pattern occurs, near 13 GPa (Figure 2.6a), with a previously unresolved peak appearing at ~ 125 cm^{-1}; this peak clearly splits into two components at 26 GPa, although the initiation of the splitting is likely associated with a transition near 23 GPa. Within the neon pressure medium, all bands shift monotonically, and lower frequency modes are observed below 70 cm^{-1}. The most straightforward explanation of these data is that a transition likely occurs near 23 GPa in the M:E medium, but is suppressed in more hydrostatic environment of the neon medium: this is consistent with the behavior of the sulfate vibrations described below. Additionally, the pressure shift of the mode near 160 cm^{-1} in the M:E medium dramatically changes near 33 GPa, suggesting the presence of a possible change in compression mechanism near this pressure (Figure 2.6b).

Two sulfate symmetric bending vibrations, v_2, are observed at room pressure and temperature in both media (Figure 2.7a, b). The relative intensities of the two v_2 peaks vary between the two media, and under pressure: this is likely a consequence of differences in sample orientation. For the results in a M:E medium, we observe a small discontinuity in frequency and change in pressure shift of both bands near 13 GPa (Figure 2.7c), in accord with the prior results of Lee et al. (2013). Within M:E, at ~ 25 GPa a new, lower frequency peak appears near 465 cm^{-1}, and progressively grows in intensity while the highest frequency peak weakens until it disappears at 42 GPa (Figure 2.7a). The new peak that is first resolved at 25 GPa becomes the dominant peak in M:E above ~ 34 GPa; it is accompanied by a peak whose location corresponds to that of the original lower frequency peak. For comparison, a weak peak with the same

frequency as the strongest peak in M:E becomes resolvable in the spectra taken in a neon medium near 39 GPa (Figure 2.7c): this peak clearly grows between 39 and 42 GPa, but remains a small feature within the spectrum. There is also the onset of a lower frequency shoulder on the second highest frequency peak in the neon spectra above ~ 26 GPa: this is not resolved in the M:E spectra, probably because of the marked weakening of this peak at these pressures. The existence of the three primary peaks between 23 and 42 GPa in M:E and between 39 and 42 GPa in neon and their progressive relative intensity changes indicate that there is a coexistence of phases within the sample, and a slow, kinetically impeded phase transition. The transition initiates near 23 GPa in M:E, and is first observed for the v_2 vibrations at 38 GPa in neon. Such a sluggish transition implies: (1) that there is a significant volume change (and hence that the transition is first-order); (2) there is very likely a change in symmetry; and (3) that the transition is activated by non-hydrostatic stress.

The v_4 region of the spectrum is substantially lower in intensity (Figure 2.2a), and three peaks are observed at room pressure and temperature. Within M:E, the high-pressure evolution of the v_4–associated peaks is the most complex of any of the vibrations of the sulfate group (Figure 2.8a, b). Within both neon and M:E, multiple new weak modes becomes resolvable between the two lower frequency modes at pressures between 5 and 18 GPa. The lower frequency of these new features is likely generated by different pressure shifts of two initially accidentally degenerate modes. In M:E, a new mode is also resolved at ~ 635 cm^{-1} and 19 GPa that is clearly present until ~ 34 GPa (Figure 2.8a, c). Within M:E, two new broad modes become resolvable near 616 cm^{-1} and 681 cm^{-1} between 34 and 36 GPa, and progressively intensify under compression. Moreover, in accord with Lee et al. (2013), the band at 606 cm^{-1} undergoes a marked increase in its pressure shift in M:E near 13 GPa (Figure 2.8c), and minor

24

discontinuities in mode frequency are observed near this pressure. The spectra in neon, in contrast, appear to shift monotonically, with the primary changes in the spectra being the appearance of modes near 5 and 18 GPa that are likely generated by differing pressure shifts of degenerate v_4 components. Unlike the v_2 modes, we do not see a definitive appearance of new modes in the spectra in neon at the highest pressure conditions, as we do in the M:E medium. However, the new v_4 peaks are weak and broad (and the peak intensities in this region of the spectrum are low), so the difficulty in resolving them is not surprising. The wide variation in frequency of the new peaks in M:E above 33 GPa suggests that the $(SO_4)^{-2}$ tetrahedra may become more distorted at these pressures.

For comparison, the sulfate symmetric stretching v_1 mode initially appears as one intense peak and a new peak clearly appears at lower frequency in M:E above 23 GPa (Figure 2.9a). This is in accord with the observations of Lee et al. (2013), who observe the onset of splitting of this peak at 21 GPa. The new peak gradually increases in intensity as the higher frequency peak decreases in amplitude until it becomes unresolvable at 42 GPa. A decrease in pressure shift is also seen above 13 GPa in M:E (Fig. 9), and there may be a small (~ 3 cm^{-1}) shift to lower frequency of the main band at this pressure, as noted by Lee et al. (2013). Within the neon medium, the new peak that occurs in the M:E medium is observed and progressively grows in amplitude, but its intensity is far smaller at comparable pressures than in M:E. Again, as with the v_4 vibrations, the v_1 modes provide strong evidence that a coexistence of phases occurs above $\sim$ 23 GPa and a kinetically impeded transition proceeds over a broad pressure range, with the transition being enhanced by shear stress within the sample.

The tetrahedral antisymmetric stretching (v_3) mode is weak within the Raman spectrum: initially, 2–3 peaks are resolved, with the highest frequency peak being the most intense. Near 23

GPa, a new lower frequency peak that is resolved near 6 GPa in neon and 13 GPa in M:E merges

with the peak observed initially at 1062 cm^{-1} at ambient pressure (Figure 2.10a–c): it is likely

that these two peaks cross-over with one another, with the initially lower frequency band

reappearing in the neon spectra near 40 GPa at ~ 1200 cm^{-1} (Figure 2.10c). In M:E, a new peak

is resolved at ~ 28 GPa and 1130 cm^{-1}: this band becomes the most intense feature in the M:E

spectrum at the highest pressure conditions. In tandem with this increased intensity, the two high

frequency peaks initially seen at 1158 cm^{-1} and 1143 cm^{-1} become unresolvable by 36 GPa.

Thus, as with the other sulfate vibrations, it appears that a new phase grows in progressively

starting near 23 GPa in the spectra taken in M:E, while the spectra taken in a neon medium

predominantly reflect the metastable barite structure to the highest pressures of these

measurements.

The two discrete v_3 vibrations that remain in the M:E spectra at the highest pressures of

these measurements lie at markedly lower frequencies than the extrapolated positions of the

initially strongest v_3 vibrations within the barite structure (Figure 2.10). As with the symmetric

stretching and bending bands, the net decrease in frequency for these bands relative to the initial

barite-structured material indicates that the force constants of the S–O bond are likely lower

within the high-pressure phase. However, the corresponding tetrahedral antisymmetric stretching

bands in the infrared spectra do evolve higher frequency components under compression (Figure

2.5), and hence the Davydov splitting (the vibrational splitting induced by placing, for example,

multiple tetrahedra into a unit cell, with splitting between in-phase and out-of-phase vibrations)

of $PbSO_4$ may markedly decrease under compression. However, Davydov splittings in sulfates in

particular (Dawson et al. 1977) and low-symmetry molecular crystals in general (Krasnyanskii

and Tsyashchenko 1980) are difficult to interpret, and likely do not straightforwardly depend on the separation/dipole–dipole interactions of the molecular groups within the crystal.

2.4 Discussion

2.4.1 Spectral Changes at 13 GPa

The spectral changes observed at 13 GPa, which had previously been interpreted to be a shift in deformational mechanism based on similar changes in Raman mode shifts and positions at 14 GPa (Lee et al. 2013), are clearly reproducible between different studies, and have subtle, but distinct, spectroscopic signatures for spectra in a M:E medium: there is an appearance of new peaks associated with the v_4 and v_3 antisymmetric bending and stretching Raman modes, the development of a new infrared v_3-associated peak, and changes in the pressure shifts of the infrared v_4 modes.

Given these vibrational spectral changes at 13–14 GPa in M:E in both our study and that of Lee et al. (2013), a key question emerges: why is no transition (or even change in compressibility) observed near this pressure in the polycrystalline X-ray diffraction measurements of Li et al. (2018) in neon, or in our Raman results in neon? The obvious answer is that this subtle set of spectral shifts, which might reflect a change in local symmetry or a high order, stress-induced transition, is activated by shear stress. The salient question then becomes whether or not this is an equilibrium phase transition that is kinetically unable to occur at 300 K in a relatively hydrostatic environment, or whether it is a non- equilibrium transition that is only activated by shear stress.

We do not have a simple answer to this question, but a shift in local symmetry in $PbSO_4$ within a stress field is compatible with the observation that the multiplicity of vibrational bands

(and their amplitudes) in sulfates (including anglesite) is consistent with a spectroscopic *Imma* symmetry (Jayasooriya et al. 1991). The vibrational spectra would then reflect a simpler, spectroscopic primitive unit cell with half the size of the *Pnma* crystallographic unit cell. In this scenario, the spectroscopic shift at 13 GPa could (speculatively) be generated by internal shifts in the local bonding configuration (such as enhanced tetrahedral distortion and/or increased coupling of sulfate tetrahedra) that cause the *Imma* character of the spectra to be lost. Assessment of the possibility of the stress-induced loss of a "latent space group" (Jayasooriya et al. 1991), as well as the prospect that an undetected transition might be present in anglesite, would require high-pressure single-crystal X-ray diffraction measurements, possibly coupled with heating to ensure that equilibrium has been reached.

2.4.2 Spectral Changes at 23 GPa

The transition at 23 GPa is substantial and is seen across all sulfate modes and in the lattice mode region within a M:E medium, and is clearly resolved as well (albeit at substantially higher pressures) in the v_1 and v_2 sulfate vibrations. New Raman-active sulfate modes (v_1, v_2, v_3) and lattice vibrations appear at this pressure. Additionally, new infrared-active sulfate modes (v_1, v_3 and v_4) appear at this pressure. Most of the new peaks appear at lower frequency than the original peaks (the new v_3 and v_4 peaks observed in the infrared spectra are exceptions to this trend), and within a M:E medium, the Raman peaks increase in intensity relative to the original peaks to become the dominant or sole features in their respective spectral regions near 40 GPa. Within a neon medium, new peaks are clearly observed and are progressively growing in at the highest pressures of these measurements, although the peaks of the barite-structured phase remain the dominant features of the spectra. Thus, the progressive in-growth of new peaks and

decline in intensity of pre-existing peaks suggests a coexistence of phases between 23 and 40 GPa in M:E; the less hydrostatic CsI medium appears to be associated with a more rapid onset of new peaks. Because the transition is slow and strongly kinetically impeded at 300 K, the driving force for the transition is likely small. Moreover, it is likely that the S–O bonds in the high-pressure phase, as manifested by the generally lower frequencies of the SO_4 vibrations, become weaker: such weakening is plausibly generated by pressure-induced stronger bonding with the lead cation. Based on the structural systematics of ABX_4 phases (Fukunaga and Yamaoka 1979; Bastide 1987; Errandonea and Manjon 2008; Clavier et al. 2011), it is possible that above 23 GPa anglesite might convert to either the scheelite or monazite structures (Figure 2.2).

2.4.3 Spectral Changes at 33 GPa

Near 33 GPa, new antisymmetric bending modes are resolved in the infrared and Raman spectra within a M:E medium. As these new peaks lie at both low and high frequencies relative to other antisymmetric bends, this wider range suggests that the sulfate groups become more distorted near this pressure. Changes in the pressure-dependence of the Pb environment also likely occur above ~ 33 GPa in a M:E medium, as manifested by the shifts in low-frequency modes. However, these changes are subtle and almost certainly do not involve changes in coordination. It is difficult to disentangle these observations from the progressive shifts in intensities that occur associated with the transition that initiates at 23 GPa; nevertheless, it appears that a subsidiary change in one of the phases may take place near 33 GPa.

2.4.4 Factor Group Analysis

Factor group analysis can yield some insight into the possible high-pressure polymorphism of anglesite. However, there are limitations: many ABX_4 compounds do not show the expected number of optically-active modes, even when high-quality single crystal measurements have been con- ducted (e.g., Porto and Scott 1967; Dawson et al. 1977; Silva et al. 2006). And, for many such materials, the magnitude of Davydov splitting is small, producing accidental degeneracies between modes: this effect is particularly acute in barite-structured sulfates (Dawson et al. 1977). Indeed, the symmetries and unit cell sizes of many ABX_4 compounds produce an expectation of large number of modes of a given type (e.g., the v_1, v_2, v_3 and v_4 vibrations of the SO_4 tetrahedra), and substantially fewer are typically observed in non-oriented, non-polarized results. These caveats aside, the number of modes of a given type observed should provide a lower limit on the number of actual modes of that type that exist within a phase, and thus preclude structures with lower numbers of modes than are observed. Table 3 compares the number of expected peaks for different possible phases with the number of observed peaks attributable to the highest pressure phase of anglesite that we characterize.

Factor group analysis of the barite/anglesite structure yields:

$$\Gamma_{opt} = 11A_g(R) + 7B_{1g}(R) + 11B_{2g}(R)$$

$$+ 7B_{3g}(R) + 7A_u(\text{inactive})$$

$$+ 10B_{1u}(IR) + 6B_{2u}(IR) + 10\ B_{3u}(IR),$$

where R, IR and inactive denote Raman-active, infrared- active, and optically-inactive vibrations, respectively (Dawson et al. 1977). However, how many tetrahedral vibrations of each type are expected for this structure is of more importance here than the 36 Raman-active vibrations and 26 infrared-active vibrations. For v_1, 2 Raman and 2 infrared vibrations are

30

predicted; for v_2, 4 Raman and 3 infrared vibrations are expected; for v_3, 6 Raman and 5 infrared modes should be ideally present; and for v_4, 6 Raman and 5 infrared bands should occur. Clearly, for the anglesite phase, substantially fewer than these are observed for each type of vibration at ambient pressure, and still fewer are able to be tracked under pressure: at pressures below 10 GPa, we are able to track 1 Raman and 1 infrared v_1 band, 2 v_2 Raman modes, 1 infrared and 4 Raman v_3 bands, and 3 infrared and 4 Raman v_4 vibrations. The limited number of bands observed is in accord with the small amount of Davydov splitting (and perhaps a latent space group, as discussed above), and hence close-to-ideal tetrahedral geometry of the SO_4 group in anglesite.

For the monazite structure, which crystallizes in the monoclinic space group P21/n with Z = 4 (e.g., Silva et al. 2006; Errandonea et al. 2015):

$$\Gamma_{opt} = 18A_g(R) + 18B_g(R) + 17A_u(IR) + 16B_u(IR).$$

Here, v_1 has 2 infrared and 2 Raman-associated expected vibrations, v_2 has 4 infrared and 4 Raman modes, and v_3 and v_4 have 6 infrared and 6 Raman-associated vibrations. For comparison, the factor group of the tetragonal I41/a scheelite structure (with Z = 2) is:

$$\Gamma_{opt} = 3A_g(R) + 5B_g(R) + 5E_g(R) + 4A_u(IR) + 3B_u(inactive) + 4E_u(IR),$$

(e.g., Vandenborre et al. 1989; Knittle and Williams 1993). Here, v_1 is associated with one Raman vibration and no infrared bands; v_2 involves 2 Raman and one infrared band; and v_3 and v_4 have 2 components in the Raman, and 2 in the infrared. For comparison, the factor group analysis of the $P2_12_12_1$ symmetry phase of $BaSO_4$, with the structure proposed by Santamaria-Perez et al. (2011) with Z = 4, is:

$$\Gamma_{opt} = 18A \ (R) + 17B_1(R, IR) + 17B_2(R, IR) + 17B_3(R, IR).$$

31

Of these, v_1 generates 4 Raman vibrations and 3 infrared bands; v_2 produces 8 vibrations: 2 that are Raman active and 6 that are Raman and infrared active; and v_3 and v_4 have 12 components in the Raman, and 8 in the infrared. Although this irreducible representation generates a large number of bands, those associated with A symmetry are anticipated to be the most intense in the Raman spectrum.

Among the vibrations in our high-pressure spectra, v_4 has five resolved Raman components in our highest pressure spectra in M:E (which likely most closely reflects the spectrum of the high-pressure phase), and six in the interval between 13 and 23 GPa; three are present in each pressure interval in the infrared spectra. Correspondingly, between 13 and 23 GPa, two components of v_1 are present in the Raman spectrum, and above 40 GPa, one appears to be present with possibly a weak mode in the infrared. For v_2, two Raman components are resolved between 13 and 23 GPa, and two different components at the highest pressures of our measurements. Finally, v_3 has two components in the infrared between 13 and 23 GPa, and four in the Raman; at our highest pressure conditions (again, in M:E), this vibration likely has two resolved Raman components and three associated infrared bands. Thus, if the 13 GPa spectral change does represent a phase transition, then it is to a phase that is closely related to the barite structure and is certainly not to either the monazite- or scheelite-structures (either of which would have been readily detected by Li et al. 2018). In terms of the 23 GPa transition, the most plausible suggestion is that this is probably a transition to the orthorhombic $P2_12_12_1$ structure previously observed in barite under pressure (Santamaria-Perez et al. 2011). This symmetry is not common among ABX_4 compounds, having only been observed to date in high-pressure $BaSO_4$, although it has also been observed in the mixed cation sulfate $K_2Mn(SO_4)_3$ (Igartua et al. 1996). This transition has been observed to have very substantial kinetic hindrance, with it

proceeding to completion between 29.5 and > 40 GPa in a He medium, and initiating at 19 GPa in silicone oil, and not being completed by 49 GPa (Santamaria-Perez et al. 2011). Thus, the kinetic hindrance of this transition is certainly of similar magnitude to that which we observe in $PbSO_4$. Moreover, since the divalent cation in this structure is 12-fold coordinate, no anomalous decrease in coordination number would occur associated with this transition. The possible transition that may initiate at 33 GPa could, based on the number of bands present, be to a lower symmetry phase, likely with a greater degree of distortion of the sulfate tetrahedra, but probably maintaining 12-fold coordination of Pb. Based on band multiplicities, this highest pressure transition is probably not to the scheelite structure, but could be a distortion/closely related phase to the *$P2_12_12_1$* structure.

2.5 Conclusions

The vibrational spectrum of anglesite undergoes a complex evolution under pressure: a major spectral shift initiates near 23 GPa. This transition is strongly kinetically impeded and shear activated, as it approaches completion in a M:E medium near 40 GPa, and has barely initiated in a neon medium at 38 GPa. This transition is observed via the appearance of new peaks associated with the tetrahedral vibrations, and splitting of a lattice mode within M:E media; it is also observed within a subset of the tetrahedral modes in the spectra taken in a neon media. Indeed, the spectra in neon largely record monotonic shifts in the vibrations of the low-pressure phase to the highest pressures of these measurements (42 GPa). More subtle spectral changes occur in the less hydrostatic media near 13 GPa and 33 GPa: the nature of these possible shifts is unclear, but may be associated with either shear stress-induced internal distortions, or equilibrium transitions that are kinetically impeded and only activated by shear stress.

These observations imply that a sluggish nucleation and growth type of transition and associated coexistence of phases occurs between 23 GPa to above 40 GPa in $PbSO_4$, and the progress of the transition is markedly enhanced by shear stress. Based on the frequencies of its Raman bands, the high-pressure phase likely has weaker S–O bonds than the barite-structured phase. While the structure of the high-pressure phase(s) is not constrained, an analogy with $BaSO_4$, which has a similarly kinetically impeded transition under compression, indicates that the $P2_12_12_1$ symmetry structure represents a likely candidate for the stable phase of $PbSO_4$ above 23 GPa.

Tables

v_0 (cm^{-1})	Infrared assignment	dv/dp (cm^{-1} GPa^{-1}) < 13 GPa	dv/dp (cm^{-1} GPa^{-1}) 13–23 GPa	dv/dp (cm^{-1} GPa^{-1}) 23–33 GPa	dv/dp (cm^{-1} GPa^{-1}) > 33 GPa
598	v_4	0.16[a]	0.41[a]	–	–
617	v_4	0.41[a]	0.19[a]	0.82±0.04	0.93±0.03
626	v_4	1.10[a]	0.86[a]	0.64±0.01	0.75±0.9
–	v_4	–	–	–	1.50±0.16
975	v_1	2.95[a]	2.25[a]	2.60±0.37	3.13±0.53
–	v_1	–	–	2.20±0.53	1.40[a]
1110	v_3	1.72[a]	2.59[a]	1.64±0.09	1.65±0.01
1121[b]	v_3	–	1.56[a]	3.17±0.17	2.54±0.01
1106[b]	v_3	–	–	4.54±0.48	3.89±0.14

[a]Two points fits
[b]Extrapolated to zero pressure from pressures above 23 GPa

Table 2.1 Pressure dependence of the infrared-active vibrations

v_0 (cm^{-1})	Raman assignment	dv/dp (cm^{-1} GPa^{-1}) linear term	(cm^{-1} GPa^{-2}) Quadratic Term	Mode γ_i
55	Pb-SO$_4$	0.58 ($\pm$0.01)	Not significant	0.62 ($\pm$0.02)
66	Pb-SO$_4$	0.60 ($\pm$0.06)	0.003 ($\pm$0.001)	0.54 ($\pm$0.06)
102	Pb-SO$_4$	2.33 ($\pm$0.04)	$-$0.012 ($\pm$0.001)	1.35 ($\pm$0.04)
111	Pb-SO$_4$	4.63 ($\pm$0.14)	$-$0.039 ($\pm$0.003)	2.46 ($\pm$0.11)
146	Pb-SO$_4$	3.65 ($\pm$0.21)	$-$0.020 ($\pm$0.005)	1.48 ($\pm$0.11)
158	Pb-SO$_4$	4.24 ($\pm$0.16)	$-$0.028 ($\pm$0.003)	1.58 ($\pm$0.08)
188	Pb-SO$_4$	5.19 ($\pm$0.13)	$-$0.040 ($\pm$0.004)	1.63 ($\pm$0.07)
439	v_2	2.33 ($\pm$0.05)	$-$0.017 ($\pm$0.001)	0.31 ($\pm$0.01)
452	v_2	2.52 ($\pm$0.05)	$-$0.011 ($\pm$0.001)	0.33 ($\pm$0.01)
606	v_4	1.02 ($\pm$0.02)	Not significant	0.099 ($\pm$0.004)
620	v_4	1.30 ($\pm$0.03)	$-$0.008 ($\pm$0.001)	0.124 ($\pm$0.005)
644	v_4	1.56 ($\pm$0.08)	1.56$\pm$0.08	0.14 ($\pm$0.01)
978	v_1	4.24 ($\pm$0.07)	$-$0.029 ($\pm$0.002)	0.26 ($\pm$0.01)
1062	v_3	3.72 ($\pm$0.11)	$-$0.018 ($\pm$0.002)	0.21 ($\pm$0.01)
1160	v_3	3.36 ($\pm$0.09)	2.48$\pm$0.11	0.17 ($\pm$0.01)

Table 2.2 Pressure dependence of the Raman-active vibrations and mode Grüneisen parameters

Factor group analysis	Barite/anglesite	Scheelite	Monazite	$P2_12_12_1$	Observed at high pressure[a]
Raman					
v_1	2	1	2	4	1
v_2	4	2	4	8	2
v_3	6	2	6	12	2
v_4	6	2	6	12	5
Infrared					
v_1	2	0	2	3	1
v_2	3	1	4	6	0
v_3	5	2	6	9	3
v_4	5	2	6	9	3

[a]Number reflects those observed peaks that are inferred to be generated by the highest pressure phase (those peaks present or increasing in amplitude at the highest pressures of these experiments)

Table 2.3 Predicted number of Raman and Infrared peaks compared to observations

Figures
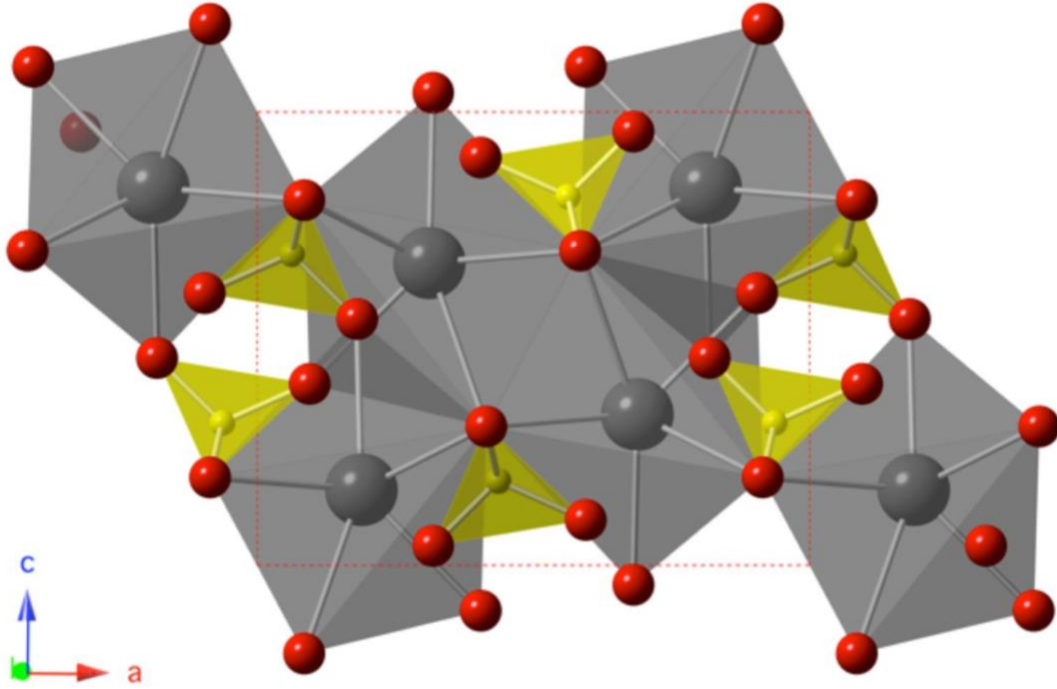
Figure 2.1 Crystal structure of anglesite down the b-axis, unit cell is the dashed outline (Miyake et al. 1978). Lead atoms/polyhedra are gray, oxygen atoms are red, and sulfur atoms/polyhedral are yellow. Crystal structure diagram generated using CrystalMaker® 8.7.6
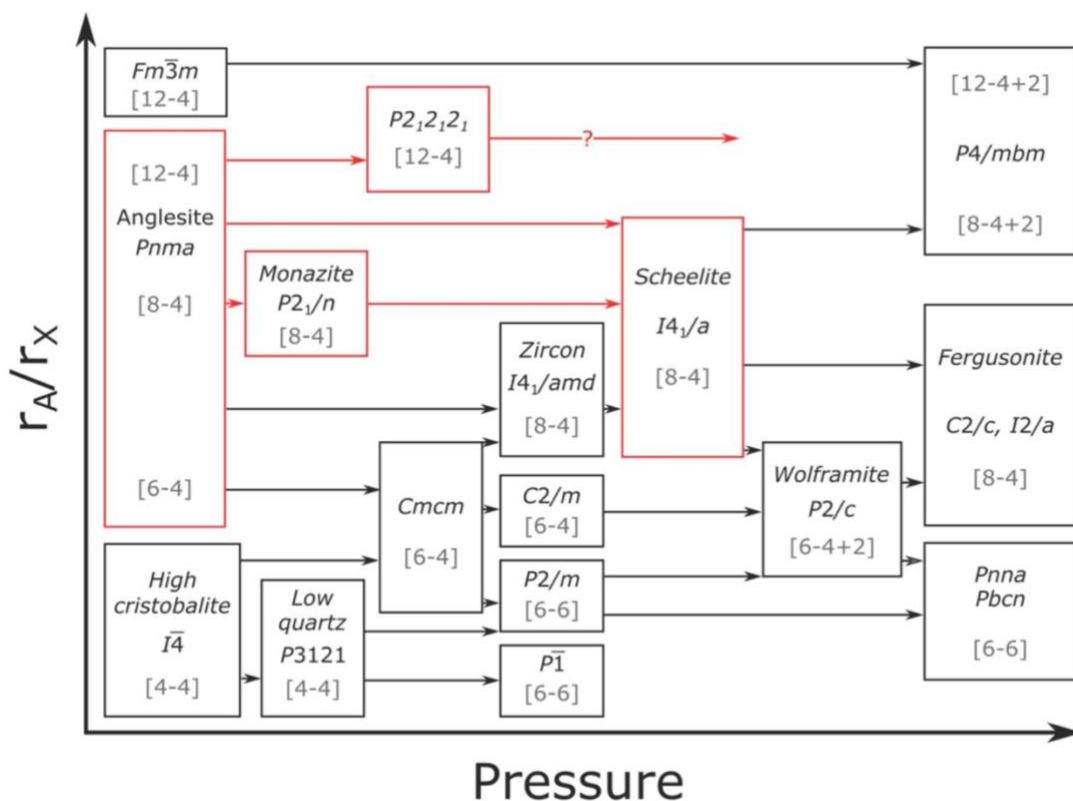
Figure 2.2 Schematic evolution of structures with increasing pressure for ABX$_4$ compounds depending on their rA/rX ratios. Red boxes and arrows indicate possible phase transition paths for anglesite under compression at room temperature. Numbers in brackets indicate coordination numbers of the A and B ions, respectively, in the structure. Modified from Errandonea and Manjon (2008), including additions from Santamaria-Perez et al. (2011)

(a)
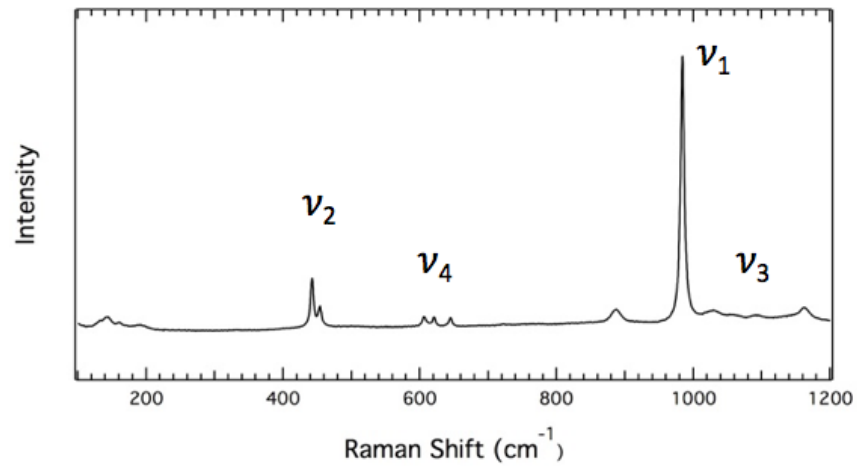
(b)
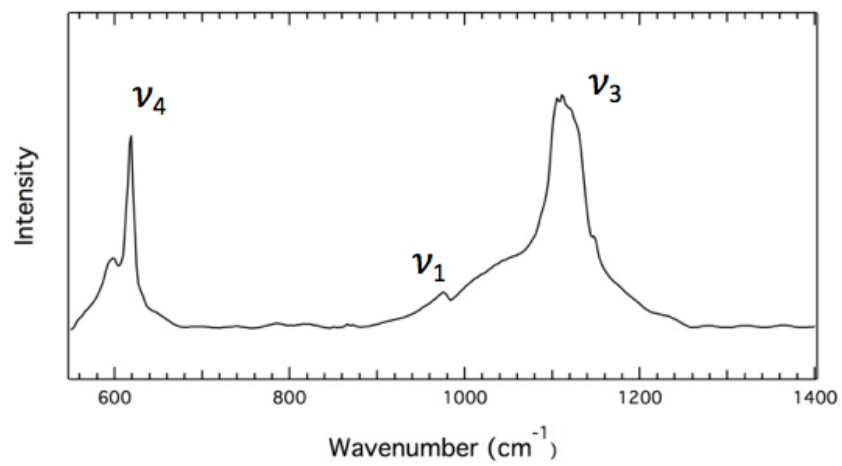
Figure 2.3 Representative ambient temperature and pressure **a** Raman and **b** infrared spectra of anglesite
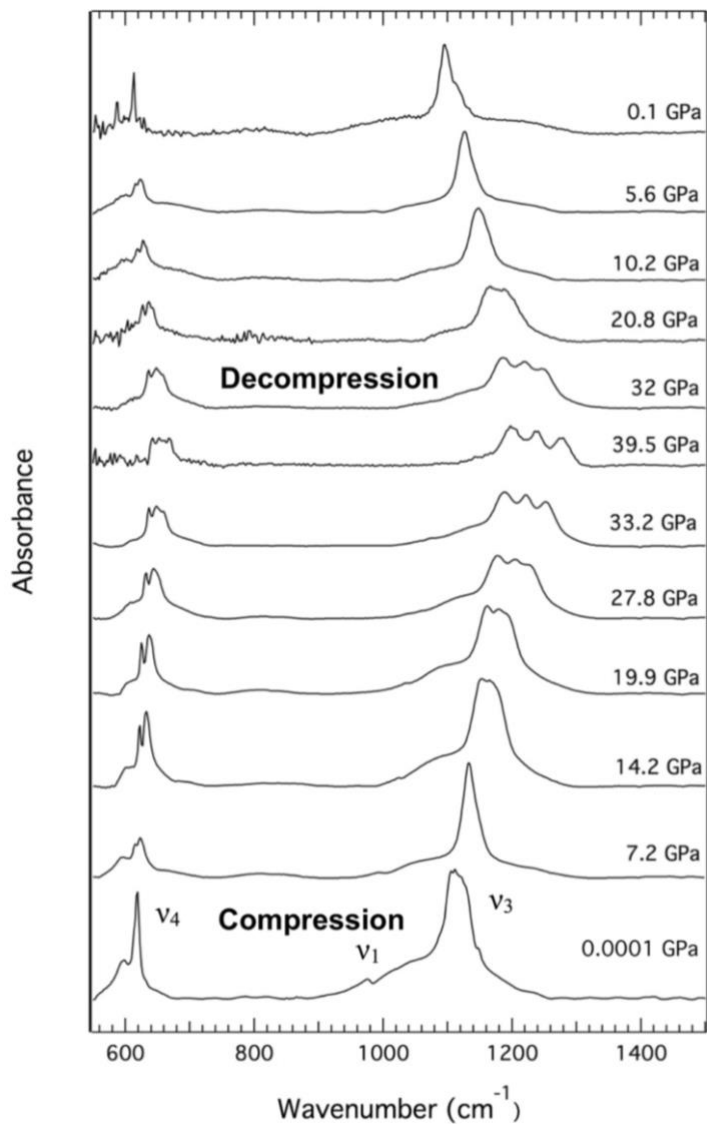
Figure 2.4 Representative mid-infrared spectra of anglesite on compression to ~ 40 GPa and decompression (top 5 spectra) at 300 K
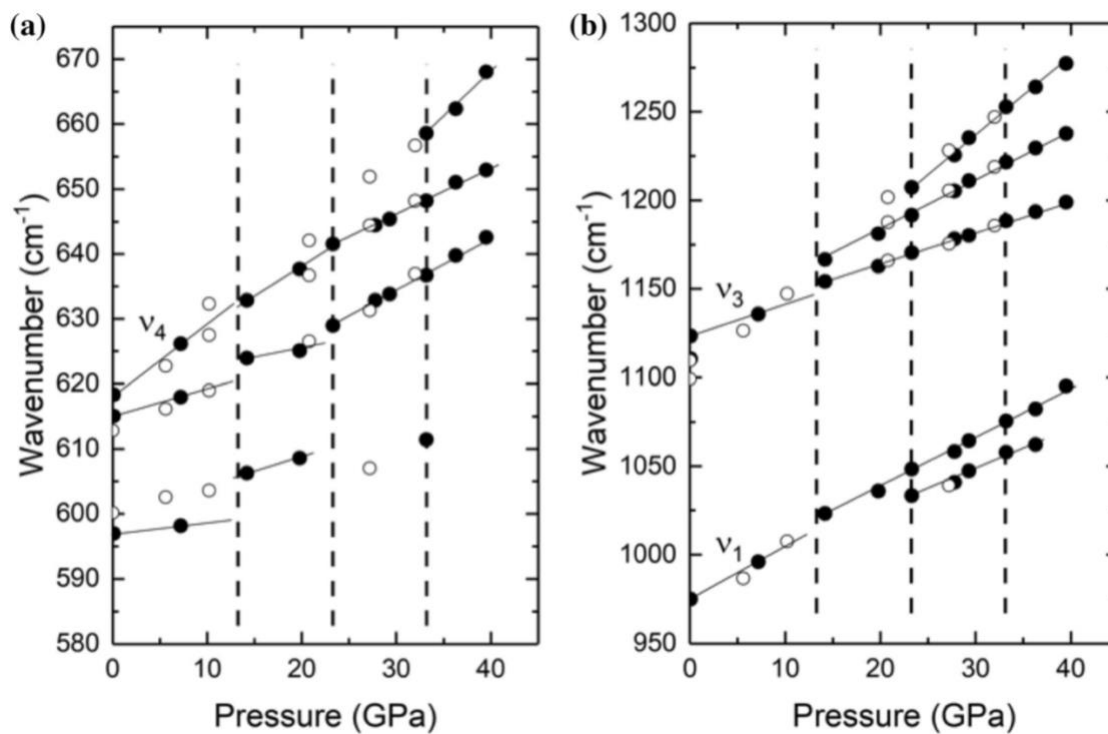
Figure 2.5 a Peak positions of the infrared-active tetrahedral antisymmetric bend, v_4, as a function of pressure. **b** Peak positions of the infrared-active tetrahedral symmetric and antisymmetric stretching modes, v_1 and v_3, as a function of pressure. Closed symbols represent compression while open symbols represent decompression. Dashed lines indicate spectral shifts/transitions and the error bars are smaller than the symbols
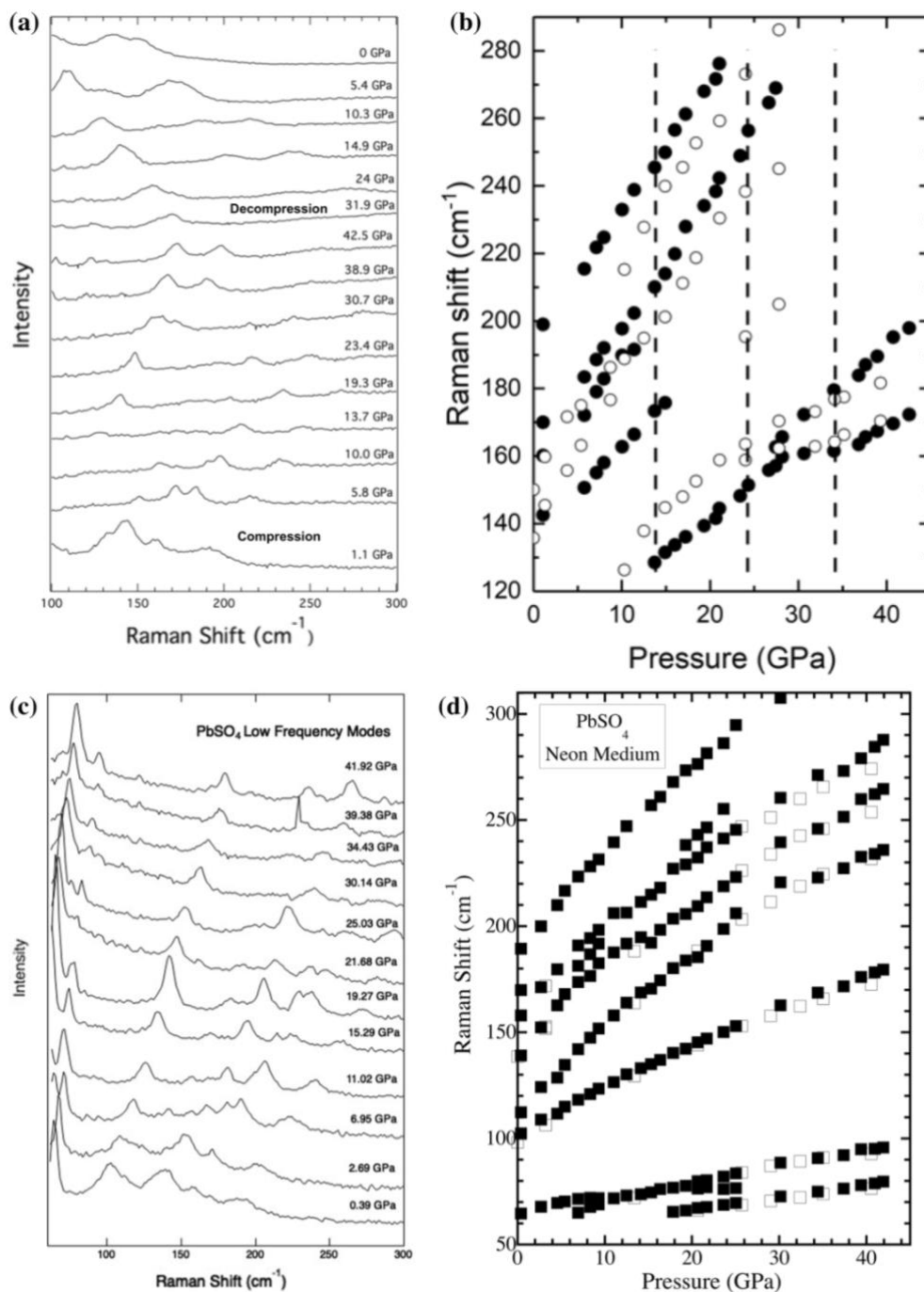
Figure 2.6 a Raman spectra of the low frequency Raman-active modes on compression and decompression (top) in methanol:ethanol. **b** Peak positions of the observed low-frequency Raman-active lattice modes as a function of pressure in M:E. Closed circles are on compression, open circles on decompression. **c** Raman spectra within neon. The spike near 260 cm^{-1} at 39.4 GPa is an artifact. **d** Mode shifts of low frequency modes in a neon medium. Closed squares are on compression, open squares on decompression. Note that the x-axis scales of **a** and **c** and y-axis scales of **b** and **d** differ
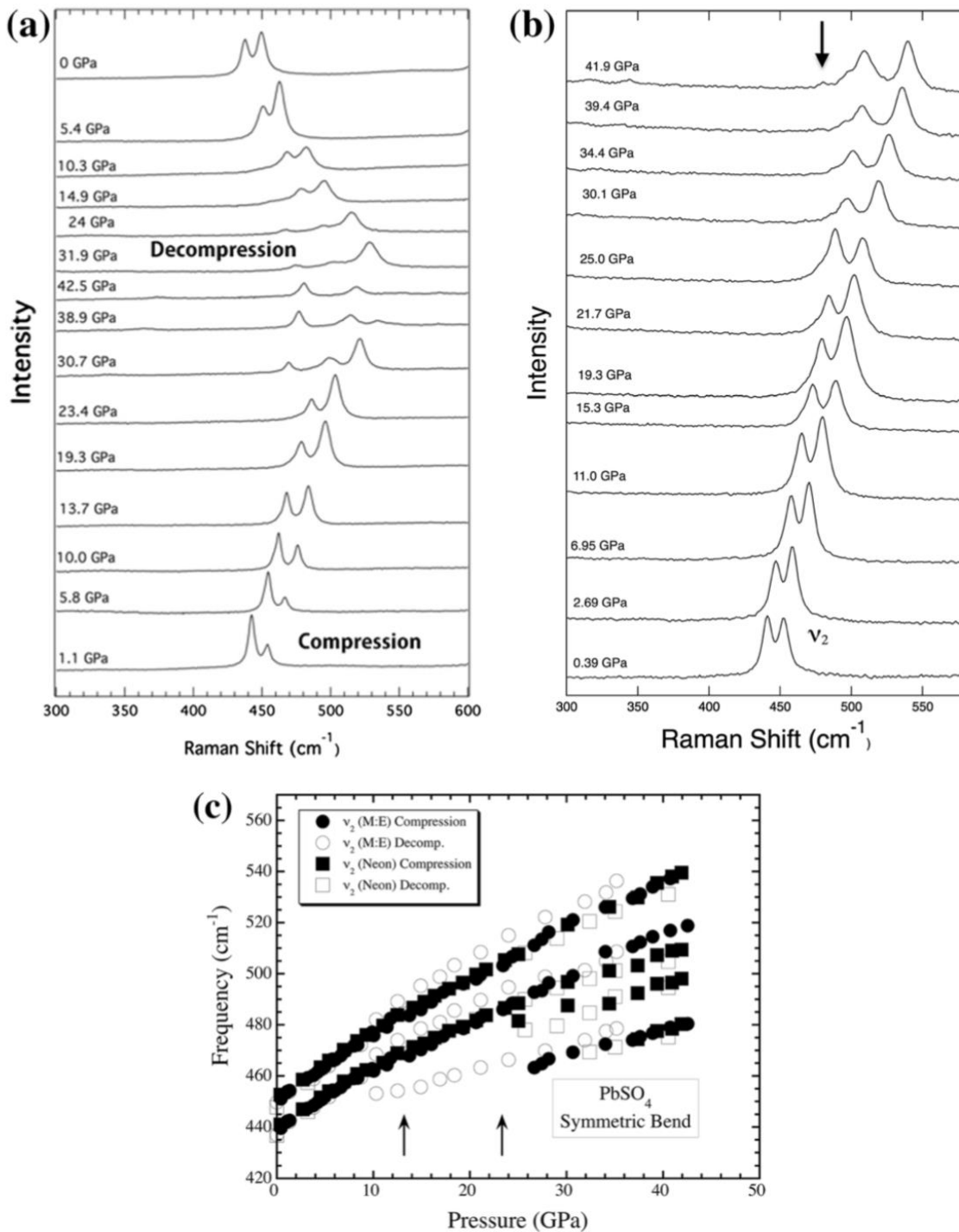
Figure 2.7 a Raman spectra of the sulfate symmetric bend, v_2, on com- pression and decompression in a M:E medium. **b** Spectra in a neon medium (arrow shows position of a new peak at the higher pressures). **c** Peak positions of the sulfate symmetric bend, v_2, as a function of pressure (arrows show positions of spectral shifts observed for these modes). Because multiple runs were conducted with the sample oriented in different directions, peak intensities vary both between runs and between compression and decompression. Closed symbols represent compression while open symbols represent decompression
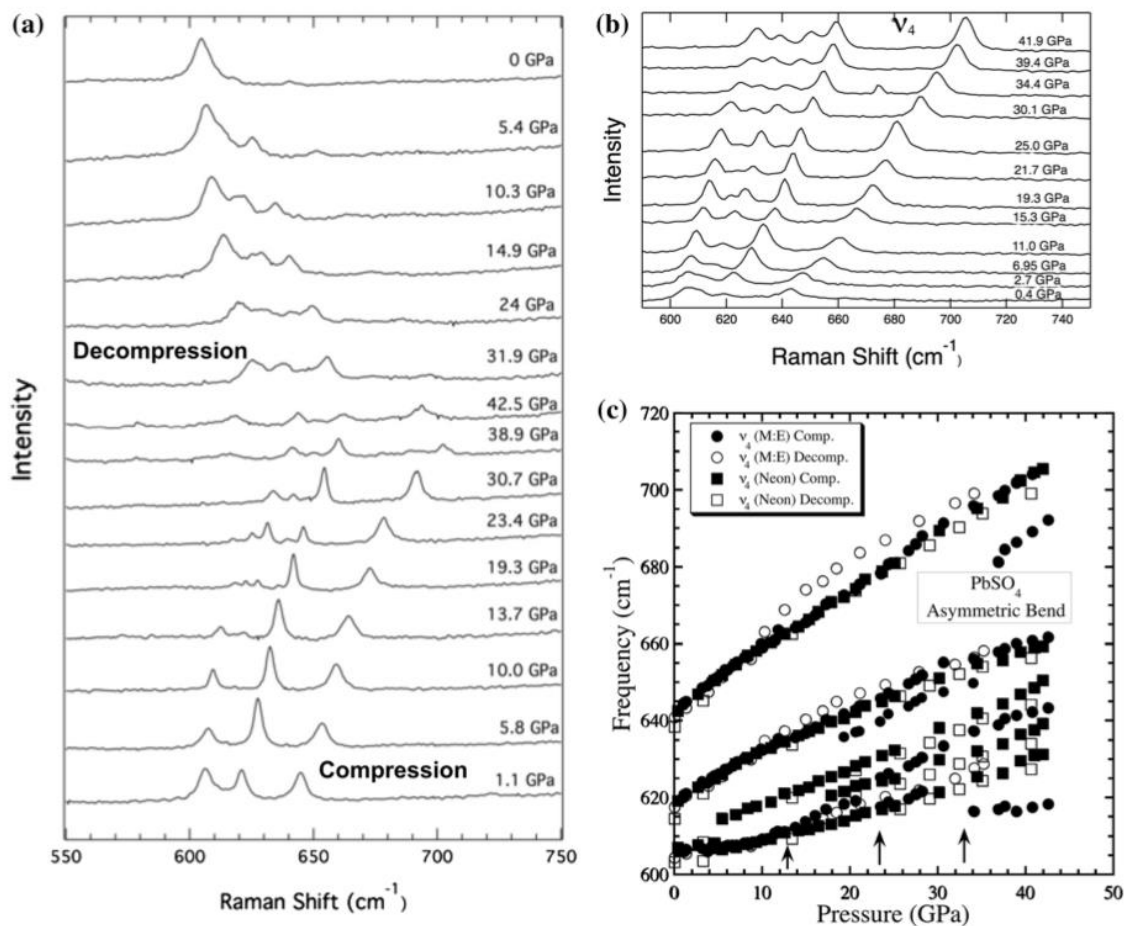
Figure 2.8 a Raman spectra of the sulfate antisymmetric bend, v_4, on compression and decompression in a M:E medium. **b** Spectra in a neon medium. **c** Peak positions of the sulfate antisymmetric bend, v_4, as a function of pressure. Arrows indicate discontinuous spectral shifts observed in this set of vibrations
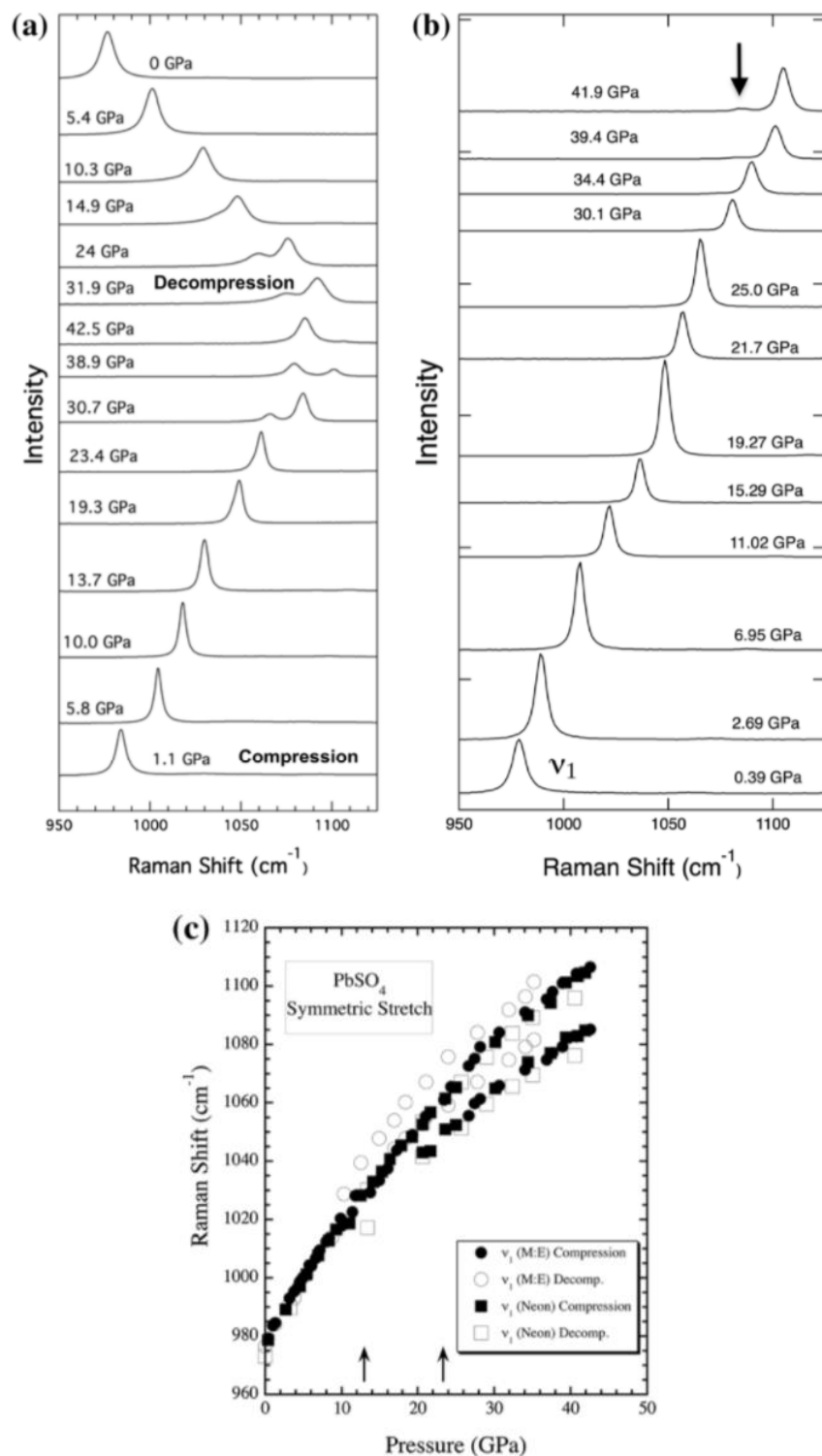
Figure 2.9 a Raman spectra of the sulfate symmetric stretch, v_1, on compression and decompression (top) in a M:E medium. **b** Sulfate symmetric stretch within a neon medium. **c** Peak positions of the sulfate symmetric stretch, v_1, as a function of pressure. Closed symbols represent compression while open symbols represent decompression
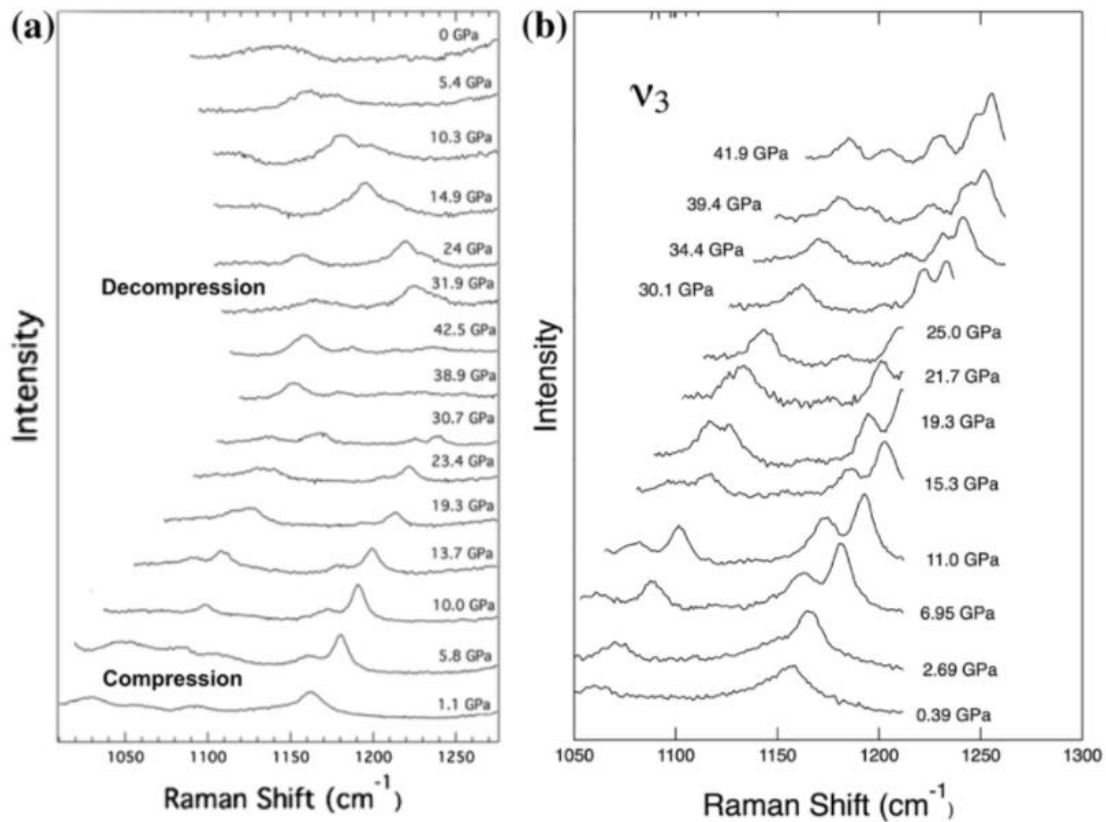
Figure 2.10 a Raman spectra of the sulfate antisymmetric stretch, v_3, on compression and decompression in a M:E medium. **b** The sulfate antisymmetric stretch in a neon medium. The spectra have been truncated to remove the high-intensity v_1 mode at lower frequencies. **c** Peak positions of the sulfate antisymmetric stretch, v_3, as a function of pressure. Closed symbols represent compression while open symbols represent decompression. Arrows indicate transitions/spectral changes

2.6 References

Alia JM, Edwards HGM, Lopez-Andres S, Gonzalez-Martin FJ, Garcia-Navarro, Mansour HR (2000) Ft-Raman study of three synthetic solid solutions formed by orthorhombic sulfates: celestite-barytes, barytes-anglesite and celestite-anglesite. *Spectroscopy Letters* 33: 323-336

Antao, SM (2012). Structural trends for celestite ($SrSO_4$), anglesite ($PbSO_4$), and barite ($BaSO_4$): Confirmation of expected variations within the SO_4 groups. *American Mineralogist* 97: 661-665

Bastide JP (1987) Simplified systematics of the compounds ABX_4 ($X = O^{2-}$, F^-) and possible evolution of their crystal structures under pressure. *Journal of Solid State Chemistry* 71:115-120

Bradbury SE and Williams Q (2009) X-ray diffraction and infrared spectroscopy of monazite-structured $CaSO_4$ at high pressures: implications for shocked anhydrite. *Journal of Physics and Chemistry of Solids* 70: 134-141

Buzgar N, Buzatu A, Sanislav IV (2009) The Raman study on certain sulfates. *Geologie* 55: 5-23

Clavier N, Podor R, Dacheux N (2011) Crystal chemistry of the monazite structure. *Journal of the European Ceramic Society* 31: 941-976.

Crichton WA, Merlini M, Hanfland M, Muller H (2011) The crystal structure of barite, $BaSO_4$, at high pressure. *American Mineralogist* 96: 364-367

Dawson P, Hargreave MM, Wilkinson GR (1977) Polarized i.r. reflection, absorption and laser Raman studies on a single crystal of $BaSO_4$. *Spectrochimica Acta* 33A: 83-93

Errandonea D and Majon FJ (2008) Pressure effects on the structural and electronic properties of ABX_4 scintillating crystals. *Progress in Materials Science* 53: 711-773

Errandonea D, Munoz A, Rodriguez-Hernandez P, Proctor JE, Sapina F, Bettinelli M (2015) Theoretical and experimental study of the crystal structures, lattice vibrations, and band structures of monazite-type $PbCrO_4$, $PbSeO_4$, $SrCrO_4$, $SrSeO_4$. *Inorganic Chemistry* 54: 7524-7535

Evans KA (2012) The redox budget of subduction zones. *Earth-Science Reviews* 113: 11-32.

Evans KA, Tomkins AG, Cliff J, Fiorentini ML (2014) Insights into subduction zone sulfur recycling from isotopic analysis of eclogite-hosted sulfides. *Chemical Geology* 365: 1-19.

Fujii T, Ohfuji H, Inoue T (2016) Phase relation of $CaSO_4$ at high pressure and temperature up to 90 GPa and 2300 K. *Physics and Chemistry of Minerals* 43: 353-361

Fukunaga O and Yamaoka S (1979) Phase transformations in ABO_4 type compounds under high pressue. *Physics and Chemistry of Minerals* 5: 167-177

Gracia L, Beltran A, Errandonea D, Andres J (2012) $CaSO_4$ and its pressure-induced phase transitions. A density function theory study. *Inorganic Chemistry* 51: 1751-1759

Griffith WP (1970) Raman studies on rock-forming minerals. Part II. Minerals containing MO_3, MO_4 and MO_6 groups. *Journal of the Chemical Society A*: 286-291

Hazen RM, Finger LW, Mariathasan JWE (1985) High-pressure crystal chemistry of scheelite-type tungstates and molybdates. *Journal of Physics and Chemistry of Solids* 46:253-263

Igartua JM, Aroyo MI, Perez-Mato, JM (1996) Systematic search of materials with high-temperature structural phase transitions: Application to space group $P2_12_12_1$. *Physical Review B* 54: 12744-12752

Jayasooriya UA, Kettle SFA, Mahasuverachai S, and White RP (1996) Lattice vibrations in compounds crystallizing with baryte structure. *Journal of the Chemical Society, Faraday Transactions* 92: 3625-3628

Jayasooriya UA, Kettle SFA, Mahasuverachai S, Al-Jowder O (1991) Manifestation of latent

    space group symmetry in the vibrational spectra of MSO_4; where M=Ba, Sr, and Pb.

    Journal of Chemical Physics 94: 5946-5948

Kaminskii AA, Bohaty L, Becker P, Rhee H, Eichler HJ, Lux O, Koltashev VV (2011)

    Stimulated Raman scattering in natural crystals on $SrSO_4$, $BaSO_4$ and $PbSO_4$: High-order

    Stokes and anti-stokes generation with single-crystal wavelength UV, visible, and near-

    IR excitation, as well as cascaded up-conversion nonlinear $x^{(3)} – x^{(3)}$ lasing effects under

    dual-wavelength picosecond collinear coherent pumping. *Applied Physics* 105: 363-378

Klotz S, Chervin JC, Munsch P, Le Marchand G (2009) Hydrostatic limits of 11 pressure

    transmitting media. *Journal of Physics D: Applied Physics* 42: 075413

Knittle E, Williams Q (1993) High pressure Raman spectroscopy of $ZrSiO_4$: Observation of the

    zircon to scheelite transition at 300 K. *American Mineralogist* 78: 245-252

Krasnyanskii GE and Tsyashchenko YP (1980) Contribution of different intermolecular

    potentials to the Davydov splitting of vibrational levels in crystals and site symmetry.

    Physica Status Solidi b 101: K151-K153

Lane MD (2007) Mid-infrared emission spectroscopy of sulfate and sulfate bearing minerals.

    American Mineralogist 92: 1-18

Lee P-L, Huang E, Yu S-C (2003) High pressure Raman and x-ray studies of barite $BaSO_4$. *High*

    Pressure Research 23: 439-450

Lee P-L, Huang E, Yu S-C, Chen Y-H (2012) High-pressure Raman study on anglesite. *World*

    Journal on Condensed Matter Physics 3: 28-32

Li B, Xu J, Chen W, Ye Z, Huang S, Fan D, Zhou W, Xie H (2018) Compressibility and

    expansivity of anglesite ($PbSO_4$) using in situ synchrotron X-ray diffraction at high-

pressure and high-temperature conditions. *Physics and Chemistry of Minerals*: doi.org/10.1007/s00269-018-0970-1

Lopez-Solano J, Rodriguez-Hernandez P, Munoz A, Gomis O, Santamaria-Perez D, Errandonea D, Manjon FJ, Kumar RS, Stavrou E, Raptis C (2010) Theoretical and experimental study of the structural stability of $TbPO_4$ at high pressures. *Physical Review B* 81: 144126

Mao HK, Xu J, Bell PM (1986) Calibration of the ruby pressure gauge to 800 kbar under quasi-hydrostatic conditions. *Journal of Geophysical Research* 91: 4673-4676

Miyake M, Minato I, Morikawa H, Iwai S-I (1978) Crystal structures and sulphate force constants of barite, celestite, and anglesite. *American Mineralogist* 63: 506-510

Ni Y, Hughes JM, Mariano AN (1995) Crystal chemistry of the monazite and xenotime structures. *American Mineralogist* 80:21-26

Porto SPS and Scott JF (1967) Raman spectra of $CaWO_4$, $SrWO_4$, and $SrMoO_4$. *Physical Review* 157: 716-718

Santamaria-Perez D, Gracia L, Garbarino G, Beltran A, Chulia-Jordan R, Gomis O, Errandonea D, Ferrer-Roca C, Martinez-Garcia D, Segura A (2011) High-pressure study of the behavior of mineral barite by x-ray diffraction. *Physical Review* (B) 84: 054102

Silva EN, Ayala AP, Guedes I, Paschoal CWA, Moreira RL, Loong C-K, Boatner LA (2006) Vibrational spectra of monazite-type rare earth orthophosphates. *Optical Materials* 29: 224-230

Vandenborre MT, Michel D, Ennaciri A (1989) Vibrational spectra and force fields of scheelite-type germanates. *Spectrochimica Acta Part A: Molecular Spectroscopy* 45: 721-727

Chapter 3 - An X-Ray Diffraction Study of the High-Pressure Structural Changes of Anglesite (PbSO$_4$)

3.1 Introduction

The deep Earth plays a critical role in the global sulfur cycle. It is likely that more sulfur is subducted into the mantle than is released by volcanic activity, creating a deep Earth sulfur reservoir (Evans, 2012; Evans, et al. (2014). Therefore, high-pressure experiments are needed to identify stable sulfur-bearing mineral phases and their thermodynamic parameters. Of particular interest to the deep Earth sulfur cycle are the sulfates which are commonly found in subducting slabs. Some of the most common sulfates include gypsum and baryte. While both minerals have been studied extensively under high pressures and temperatures, studies on baryte group minerals have had conflicting results. Santamaria-Perez et al. (2011) studied baryte and saw a sluggish transition between 13 and 27 GPa (depending on pressure medium) to a distorted orthorhombic barite structure with space group $P2_12_12_1$. Lee et al. (2003) observed changes in Raman spectra and X-Ray diffraction patterns of baryte around 10 GPa which were interpreted to be a phase transition to a new structure. Crichton et al. (2011) studied baryte to 21.5 GPa using Raman spectroscopy and saw no phase transition. Meanwhile, Chen et al. (2010) studied isostructural celestite (SrSO$_4$) to 26 GPa and saw a transition at 11 GPa which they concluded to be a distortion of the Sr-O polyhedra. However, experiments by Girard et al., (2018) saw no phase transitions to 62 GPa. Clearly further study of the baryte-group minerals is needed to determine their high-pressure behavior and the isostructural lead sulfate, anglesite (PbSO$_4$), is a good candidate.

Anglesite (PbSO$_4$) is a member of the baryte group. It has an orthorhombic *Pnma* crystal structure comprised of SO$_4$ tetrahedra with Pb^{2+} in pseudo-eight to twelve-fold coordination with

the oxygen ions (Figure 3.1). The coordination of lead in anglesite is highly irregular, with Pb-O distances varying from 2.61(2) Å to 3.73(1) Å (Miyake et al. 1978; Antao 2012). Anglesite has been a known member of the baryte group since its discovery in 1832 at the Parys Mountain Mine in Wales. It forms as a secondary weathering product in acidic lead-bearing ore oxidation zones (Keim and Markl, 2015).

Previously, Lee et al. (2013) studied anglesite using Raman spectroscopy to 35 GPa, observing two structural changes at 14 and 21 GPa. Li et al. (2018) studied anglesite to 21.6 GPa with X-ray diffraction and found no changes. They report a bulk modulus, $K_0 = 59$ GPa and its pressure derivative, $K' = 5.3$. Santamaria-Perez et al. (2019) studied anglesite using X-Ray diffraction to 67 GPa and found Anglesite converts to the $P2_12_12_1$ structure above 27 GPa. Equation of state measurements by Santamaria-Perez et al. of the high-pressure phase resulted in a $K_0 = 68$ GPa and $K' = 5.03$. However, due to a lack of data at lower pressures, the ambient pressure phase was estimated to be $K_0 = 63.8$ GPa. A previous study by Sawchuk et al. (2019) investigated anglesite using infrared and Raman spectroscopy and found two structural changes at 20 GPa and 40 GPa. These were interpreted to be the initiation and completion of a sluggish transition to the $P2_12_12_1$ structure. In our X-ray diffraction experiments, we access higher pressures than previously studied, assemble a more complete data set, and compare results with previous diffraction and spectroscopy work.

3.2 Experimental Methods

3.2.1 Sample

Natural crystals of anglesite from Sardinia, Italy were used in these experiments (UCLA Collection #MS1603). Samples were white, translucent, formed crystals up to 1cm, and

coexisted with galena. All samples were from a 4 mm^3 crystal which was ground into a powder. Sample identity was confirmed by Raman spectroscopy and X-ray diffraction. X-ray diffraction also determined the lattice parameters a= 8.449(2) Å, b= 5.397(1) Å, c= 6.963(1) Å, and V$_0$= 319.23(7) Å^3 at room pressure and temperature which are in good agreement with previous measurements (Antao, 2012).

3.2.2 Synchrotron X-Ray Diffraction

Symmetric type diamond anvil cells (DACs) were used to generate high pressures in these experiments. This apparatus uses two brilliant-cut diamonds with 250 µm culets mounted to metal backing plates that are screwed together in axial compression to generate pressures of up to 75 gigapascals (GPa). Between the two diamonds is a spring-steel gasket which was pre-indented to ~ 25µm thickness and had a 90 µm diameter hole drilled and centered on the face of the diamonds. This hole creates the sample chamber. Inside the sample chamber is the sample, which is comprised of a small pellet of anglesite powder ~ 30 µm across by ~10 µm thick, a few small grains of ruby which are used as a pressure gauge using fluorescence spectroscopy (Mao et al. 1986), and gas loaded neon which serves as a hydrostatic pressure transmitting medium (Klotz et al., 2009). Gas loading was done using the COMPRES gas loading apparatus.

Two high-pressure X-ray diffraction experiments for anglesite were performed at beamline 12.2.2 at the Advanced Light Source in Berkeley, CA. Beamline 12.2.2 is a specialized high-pressure hard X-ray (15-25 KeV) light source operating under monochromatic conditions; ($\lambda = 0.4973$ Å) with a focused X-ray spot size of 10 µm x 10 µm to provide multigrain X-ray diffraction from powder samples loaded in a pressurized diamond anvil cell. Patterns were collected for 1-2 minutes on a two-dimensional MAR 345 imaging plate calibrated

with CeO2 standard powder. The patterns collected contain information from the sample, with ring positions corresponding to lattice spacings using Bragg's law. Calibration of the beam center, detector tilt, and distance from the sample to the detector was completed using the program DIOPTAS (Prescher and Prakapenka, 2015). DIOPTAS also integrates the ellipses and creates a one-dimensional pattern of intensity as a function of two-theta. Each peak along the one-dimensional profile corresponds to the d-spacing for a set of lattice planes.

Run 1 reached a pressure of 46.4 GPa in 2-5 GPa pressure steps before it was decompressed to ambient pressure in 5-10 GPa pressure steps. Run 2 reached 30 GPa in 2-5 GPa pressure steps, data was not collected on decompression. X-ray diffraction patterns were taken at each pressure step. Pressures were determined at each pressure step using ruby fluorescence and the offline Raman spectrometer at the ALS.

Two-dimensional angle dispersive diffraction patterns were collected and integrated using the program DIOPTAS (Prescher and Prakapenka, 2015) to yield intensity versus two-theta diffraction patterns (Figure 3.2). Peak positions were determined in 2 theta space from the full width, half max. Corresponding d-spacings were calculated using Bragg's Law. For each run and at each pressure step the first 7 diffraction peaks were used to calculate the lattice parameters.

3.3 Results

3.3.1 X-Ray Diffraction

At ambient conditions the lattice parameters for our sample of anglesite are a= 8.449(2) Å, b= 5.397(1) Å, c= 6.963(1) Å, and V=319.23(7) Å^3. These values are in excellent agreement with previous measurements (Miyake et al., 1978). The indexed ambient X-ray diffraction

patterns of anglesite ($PbSO_4$) is shown in figure 3.2. Figure 3.3 shows a series of diffraction patterns taken from run 1 during compression and decompression. The peak shifts as a function of pressure are shown in figure 3.4. Both X-ray diffraction experiments agree well with each other. We observe two-theta peak positions increase as a function of pressure corresponding to compression of the lattice structure, and are reversible on decompression with some hysteresis. We observe two structural changes at 21 and 40 GPa. At 21 GPa two new diffraction peaks appear; however, at this pressure we observe no discontinuity in the slope of the lattice parameters as a function of pressure. At 40 GPa the trend of the [200] lattice plane appears to change, indicating a structural change (Figure 3.4).

The centroid position for the peaks were determined from the full width, half max and corresponding d-spacings were calculated using Bragg's law. At each pressure step the first seven diffraction peaks were used to calculate the best-fit orthorhombic lattice parameters. These seven peaks are associated with the following lattice planes: (101), (111), (120), (200), (021), (210), and (121). Lattice parameters were calculated using the program Unit Cell (Holland and Redfern, 1997), yielding values for the lattice parameters a, b, c, and volume (table 3.1). All lattice parameters decrease with pressure. However, above 40 GPa, we see changes to the slope in both the a and b lattice parameters. This can be seen more clearly in figure 3.5, which shows the lattice parameter a, b, and c as a function of pressure. Figure 3.6 shows the change in lattice parameter ratios with pressure.

Around 21 GPa we observe two new peaks emerging. The first of these peaks is located 6.53 2θ and appears between the 19.6 and 21.6 GPa pressure steps. The second peak is located at 9.77 2θ and appears between the 22.7 and 25.7 GPa pressure steps. Both begin as weak peaks, gradually grow in intensity with increasing pressure, and disappear on decompression with some

56

hysteresis.

Around 40 GPa we observe a downturn of the slope of the (200) lattice plane. We also observe a discontinuity in slope of the *a* lattice parameter resulting in a decrease of that lattice parameter. Additionally, the *b* lattice parameter undergoes the opposite change, an increase of that lattice parameter. The slope of the *c* lattice parameter appears to be unchanged. All changes are reversible on decompression with some hysteresis.

3.3.2 *P2$_1$2$_1$2$_1$* Structural Changes

We attribute the changes we observe at both 21 and 40 GPa to a phase transition to the *P2$_1$2$_1$2$_1$* structure. Santamaria-Perez et al. (2011) observed the transformation of baryte to the *P2$_1$2$_1$2$_1$* structure and describes it in detail. The *P2$_1$2$_1$2$_1$* structure is a subgroup of the *Pnma* structure and a distortion of the ambient-pressure baryte structure. It is caused by displacement and tilting of the SO_4^{2-} tetrahedra. In experiments done by Santamaria-Perez et al. on barite, they observe two new peaks which appear at 27 GPa. Additionally, the *P2$_1$2$_1$2$_1$* transition they observe was accompanied by a contraction the *a* lattice parameter by 18%, and an expansion of the *b* lattice parameter by 20%. This transition in has been observed to be kinetically impeded with a large pressure range of the ambient and high-pressure phases coexisting (Santamaria-Perez et al., 2011; Santamaria-Perez et al., 2019; Sawchuk et al., 2019).

In our study, we observe two new peaks that appear at 21 GPa followed by a contraction of the *a* lattice parameter and an expansion of the *b* lattice parameter across the transition observed at 40 GPa. Given the similarities of this transition with the transitions observed by Santamaria-Perez et al. (2011) in baryte and Santamaria-Perez et al. (2019) in anglesite, we believe it very likely the new phase we observe in our anglesite experiments is the *P2$_1$2$_1$2$_1$*

structure. In agreement with previous studies, we observe a kinetically impeded phase transition which results in the ambient pressure phase and the high-pressure phase coexisting between 21 GPa and 40 GPa.

3.3.3 Equation of State of Anglesite

Figure 3.7 shows a plot of the unit cell volume as a function of pressure for all runs along with experimental data from Li et al. (2018) and Santamaria-Perez et al. (2019). As is also observed by Santamaria-Perez et al., lattice parameters reported by Li et al. are slightly smaller than those measured in our data. We do not have an explanation for this discrepancy. Lattice parameters reported by Santamaria-Perez et al. agree very well with our data. We determined the best fit values for K_{0T} and K' of both the low-pressure and high-pressure phases using our pressure-volume experimental data and the Birch-Murnaghan equation of state (Birch, 1947). For the low pressure phase, this yields an isothermal bulk modulus of K_{0T}=63.2(2.7) GPa and K'= 5.9(4)., the line for this fit is plotted in figure 3.7. For the high-pressure phase, this yields values of V_0 =315.2(8) Å^3, K_{0T}=72.9(3.8) GPa, and K'= 4.7(4), this is plotted as a dotted line in figure 3.7. The values for the low pressure phase are in good agreement with values reported by both Li et al. 2018 who reports a K_0 = 59 GPa and K' = 5.3 and Santamaria-Perez et al. (2019) who reports a K_0 = 63 GPa. The values for the high-pressure phase are also in good agreement with those reported by Santamaria-Perez et al. (2019) who reports a V_0 = 314.7(4) Å^3, K_{0T} = 68(1) GPa, and K' = 5.03(6).

3.4 Conclusions

In summary, we have studied the high-pressure behavior of the lead sulfate, anglesite ($PbSO_4$), up to 46 GPa using x-ray diffraction. In our experiments, we observe changes to the initial structure that we interpret to be a phase transition that initiates at 21 GPa and is not complete until 40 GPa. These changes include the appearance of new peaks at 21GPa, a contraction of the *a* lattice parameter, and an expansion of the *b* lattice parameter. Our observations are consistent with a phase transition, observed by other high-pressure studies on anglesite and baryte, to a distorted baryte structure, *$P2_12_12_1$*. This transition is kinetically impeded which results in a coexistence of phases from 21 to 40 GPa. Future work should focus on the effects high temperatures may have on this transition. It is likely the introduction of high temperatures would help drive this phase transition forward. From our experimental data we also calculate anglesite's isothermal bulk modulus yielding K_{0T}=63(2) GPa and K'= 5.9(4) for the low pressure phase and K_{0T}=67(4) GPa and K'= 4.9(4). While anglesite is likely not a common mineral in the deep Earth, its study at high pressures may give insight into phase stability among sulfates in the mantle and thus provide information about the deep Earth sulfur cycle.

Tables

	Pressure	a	b	c	V_0
Run 1 - Compression	4.6	8.318(1)	5.270(1)	6.8081(9)	298.50(6)
	8.8	8.210(1)	5.193(1)	6.7048(8)	285.89(6)
	12.3	8.146(1)	5.147(1)	6.6423(8)	278.56(6)
	15	8.102(1)	5.120(1)	6.6004(8)	273.88(6)
	18.3	8.035(1)	5.084(1)	6.5438(8)	267.36(5)
	22.7	7.990(1)	5.039(1)	6.4866(8)	261.21(5)
	25.7	7.948(1)	5.014(1)	6.4332(8)	256.41(5)
	29.1	7.899(1)	4.971(1)	6.3814(8)	250.60(5)
	33.7	7.871(1)	4.955(1)	6.3289(7)	246.85(5)
	37.7	7.845(1)	4.911(1)	6.2836(7)	242.14(5)
	40.1	7.798(1)	4.936(1)	6.2110(7)	239.13(5)
	42.6	7.794(1)	4.889(1)	6.2129(7)	236.77(4)
	46.4	7.794(1)	4.836(1)	6.1608(7)	232.26(4)
Run 1 – Decompression	39.2	7.786(1)	4.850(1)	6.2111(7)	234.59(4)
	35	7.811(1)	4.879(1)	6.2512(7)	238.25(5)
	31.1	7.831(1)	4.927(1)	6.3169(7)	243.75(5)
	22.8	7.919(1)	5.007(1)	6.4277(8)	254.92(5)
	14.6	8.104(1)	5.142(1)	6.6056(8)	275.29(6)
	3.8	8.358(1)	5.301(1)	6.8386(9)	303.00(6)
	0	8.493(1)	5.397(1)	6.9632(9)	319.23(7)
Run 2 – Compression	0.6	8.467(1)	5.359(1)	6.9362(9)	314.76(7)
	5.2	8.310(1)	5.238(1)	6.7956(9)	295.87(6)
	9.8	8.177(1)	5.157(1)	6.6846(8)	281.90(6)
	15.7	8.065(1)	5.090(1)	6.5807(8)	270.20(5)
	19.6	7.993(1)	5.058(1)	6.5099(8)	263.23(5)
	21.6	7.982(1)	5.034(1)	6.4932(8)	260.93(5)
	26.1	7.926(1)	4.980(1)	6.4307(8)	253.89(5)
	30.3	7.875(1)	4.948(1)	6.3774(8)	248.57(5)

Table 3.1 Experimental values for the a, b, and c lattice parameters and volumes across all runs for compression and decompression.

Figures
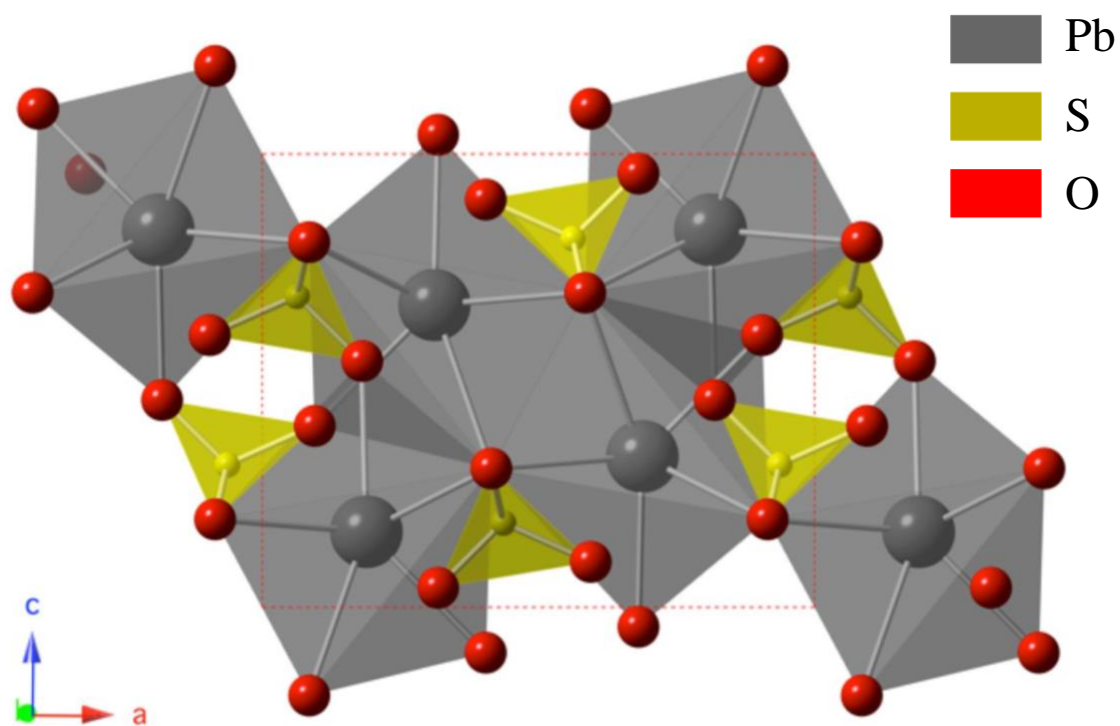
Figure 3.1 Crystal structure of anglesite down the b-axis. Dashed outline shows the unit in the a and c direction. Crystal structure diagram generated with CrystalMaker® 8.7.6. using the atomic positions of Miyake et al. (1978)
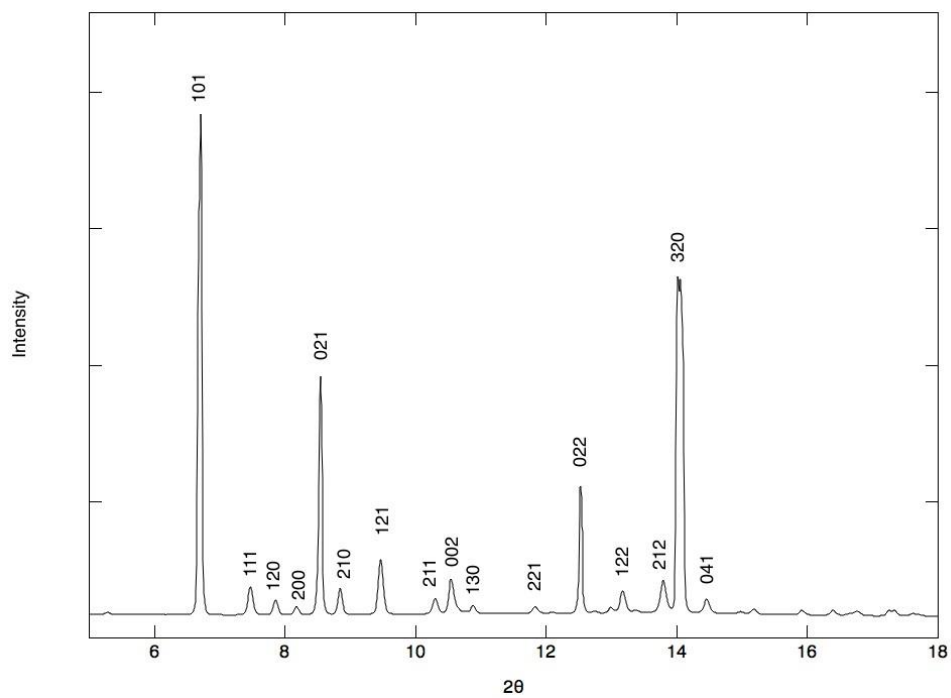
Figure 3.2 Indexed X-ray diffraction pattern of anglesite at 0.5 GPa and ambient temperature. λ= 0.495Å
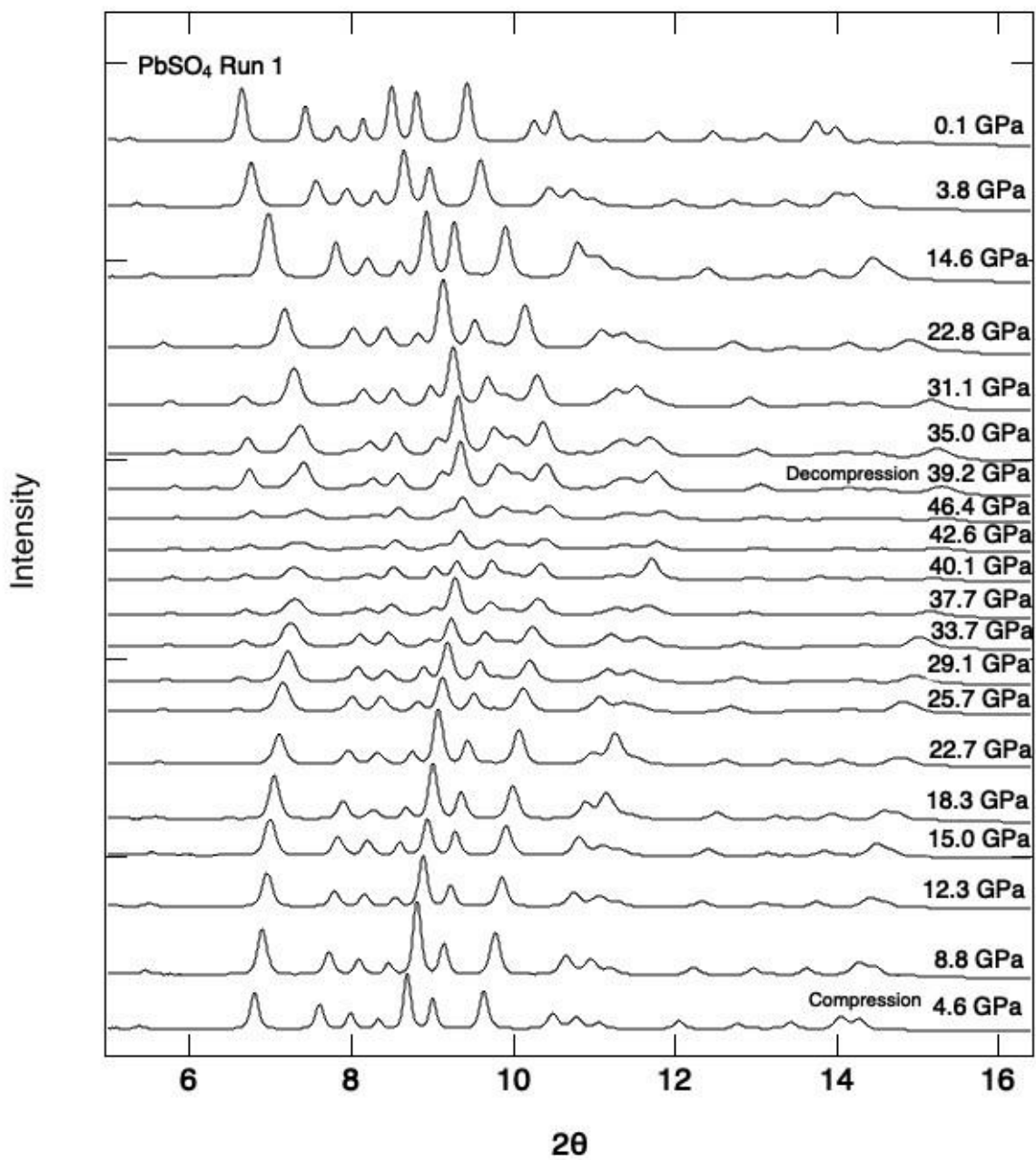
Figure 3.3 X-ray diffraction patterns of anglesite under compression to 46 GPa and decompression (Run 1). $\lambda = 0.495$Å
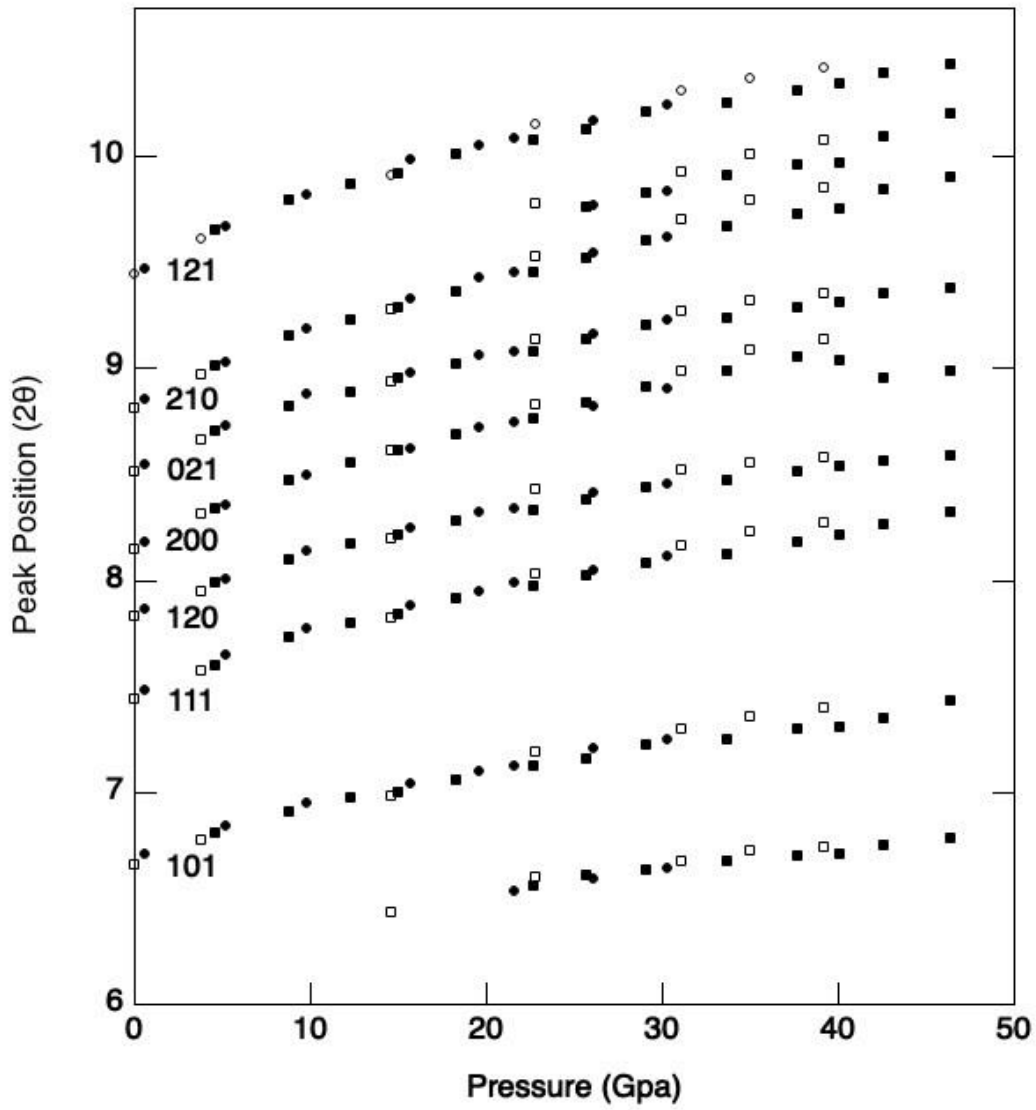
Figure 3.4 Peak position of anglesite as a function of pressure on compression (closed symbol) and decompression (open symbol) for Run 1 (squares) and Run 2 (circles)
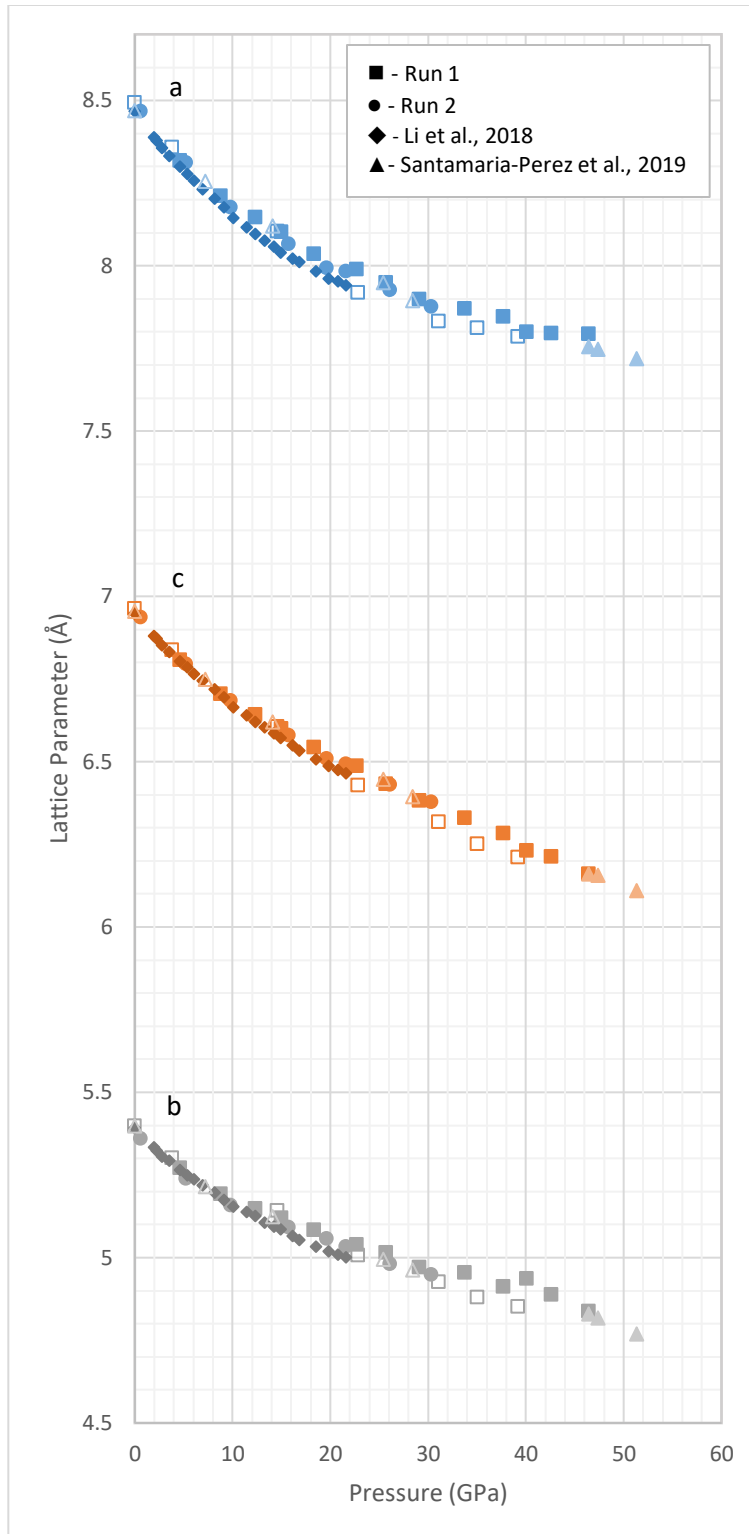
Figure 3.5 Lattice parameters: a (blue), b (gray), and c (orange) of anglesite as a function of pressure. Our data shown as filled squares (Run 1, compression) filled circles (Run 2, compression), and open squares (Run 1, decompression). Data from Li et al. 2018 (diamonds) and Santamaria-Perez et al. 2019 (triangles) also shown
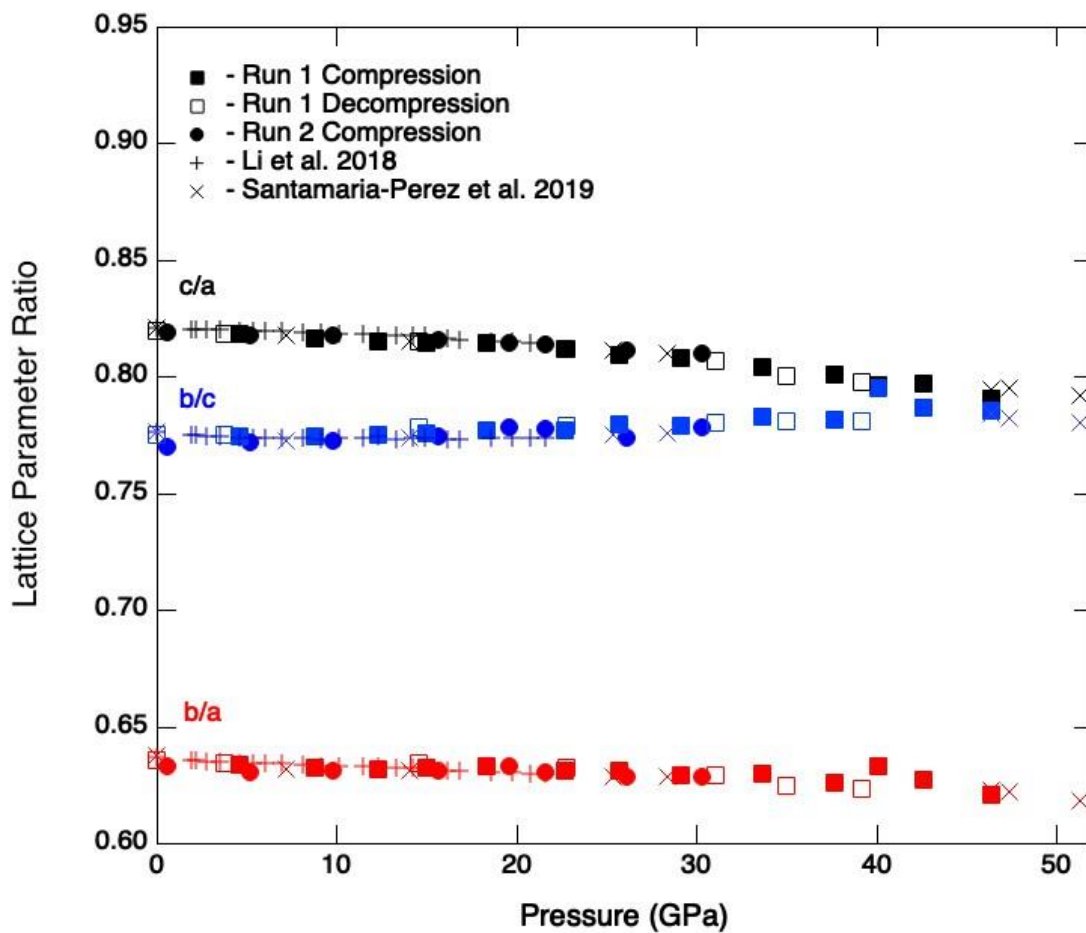
Figure 3.6 Lattice parameter ratios for c/a (black), b/c (blue), and b/a (red). Our data shown as filled squares (Run 1, compression) filled circles (Run 2, compression), and open squares (Run 1, decompression). Data from Li et al. 2018 (+ symbol) and Santamaria-Perez et al. 2019 (× symbol) also shown.
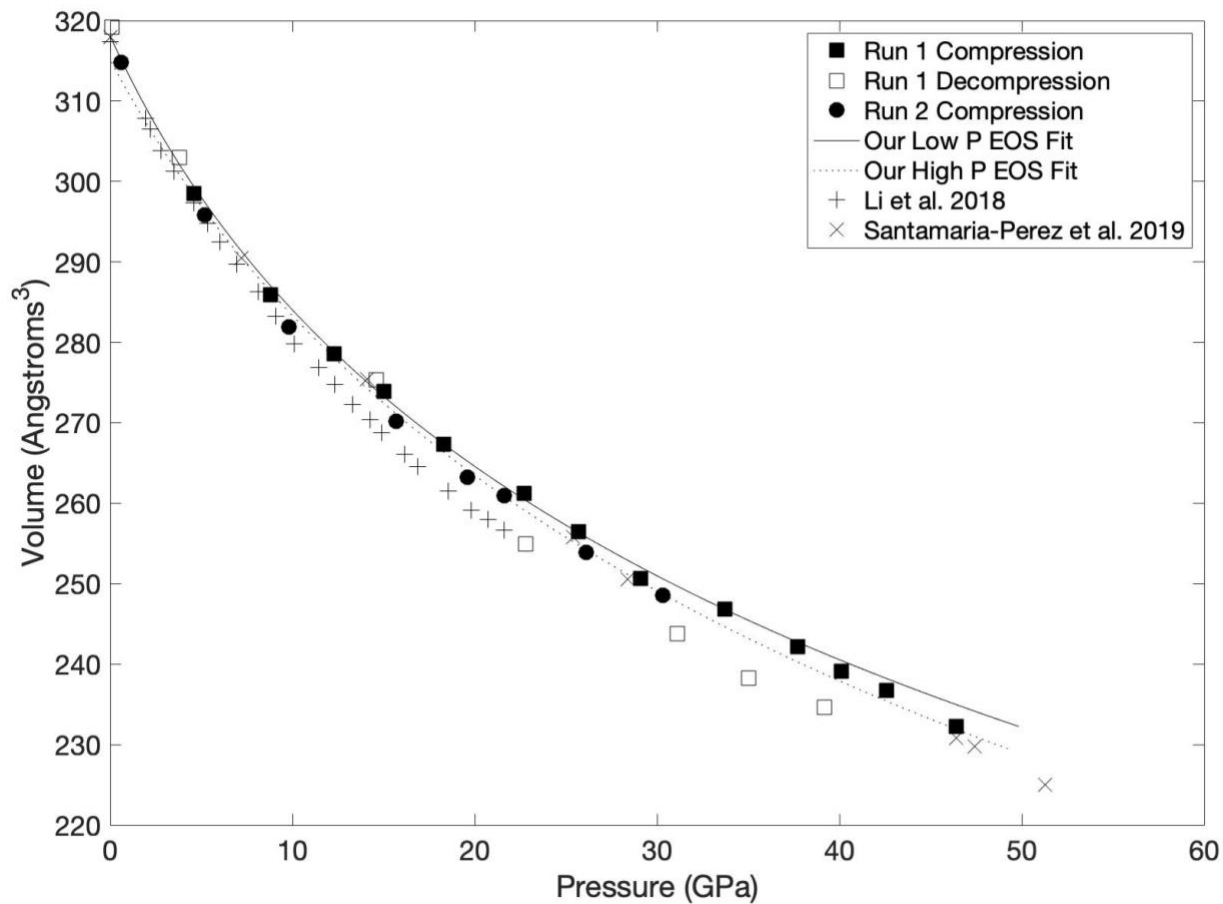
Figure 3.7 Volume of anglesite as a function of pressure with equation of state curves for the high pressure phases fit to the data. Our data shown as filled squares (Run 1, compression) filled circles (Run 2, compression), and open squares (Run 1, decompression). Data from Li et al. 2018 (+ symbol) and Santamaria-Perez et al. 2019 (× symbol) also shown

3.5 References

Antao SM (2012) Structural trends for celestite (SrSO$_4$), anglesite (PbSO$_4$), and barite (BaSO$_4$): confirmation of expected variations within the SO$_4$ groups. *American Mineralogist* 97:661–665

Birch F (1947) Finite elastic strain of cubic crystals. *Phys Rev* 71:809

Chen Y-H, Yu S-C, Huang E, Lee P-L (2010) Raman Spectroscopy and X-ray diffraction studies on celestite. *Physica B: Condensed Matter*, Volume 405, Issue 20, pages 4386-4388

Crichton WA, Merlini M, Hanfland M, Muller H (2011) The crystal structure of barite, BaSO$_4$, at high pressure. *American Mineralogist*, Volume 96, pages 364-367

Evans KA (2012) The redox budget of subduction zones. *Earth-Science Reviews* 113: 11-32.

Evans KA, Tomkins AG, Cliff J, Fiorentini ML (2014) Insights into subduction zone sulfur recycling from isotopic analysis of eclogite-hosted sulfides. *Chemical Geology* 365: 1-19.

Girard A, Stekiel M, Spahr D, Morgenroth W, Wehinger B, Milman V, Nguyen-Thanh T, Mirone A, Minelli A, Paolasini L, Bosak A, Winkler B (2018) Structural, elastic and vibrational properties of celestite, SrSO$_4$, from synchrotron x-ray diffraction, thermal diffuse scattering, and Raman scattering. *Journal of Physics: Condensed Matter*, vol. 31, 055703

Holland TJB and Redfern SAT (1997) Unit cell refinement from powder diffraction data: the use of regression diagnostics. *Mineralogical Magazine* 61: 65-77.

Keim M and Markl G (2015) Weathering of galena: Mineralogical processes, hydrogeochemical fluid path modeling, and estimation of the growth rate of pyromorphite. *American Mineralogist,* Volume 100, pages 1584-1594

Klotz S, Chervin JC, Munsch P, Marchand GL (2009) Hydrostatic limits of 11 pressure transmitting media. J. *Phys. D: Appl. Phys*. 42 075413 DOI:10.1088/0022-3727/42/7/075413

Lee P-L, Huang E, Yu S-C (2003) High Pressure Raman and X-ray studies of barite, $BaSO_4$. *High Pressure Research*, 23:4, 439-450, DOI: 10.1080/0895795031000115439.

Lee P-L, Huang E, Yu S-C, Chen Y-H (2013) High-pressure Raman study on anglesite. *World J Condens Matter Phys* 3:28–32

Li B, Xu J, Chen W, Ye Z, Huang S, Fan D, Zhou W, Xie H (2018) Compressibility and expansivity of anglesite ($PbSO_4$) using in situ synchrotron X-ray diffraction at high-pressure and high-temperature conditions. *Phys Chem Miner*. https://doi.org/10.1007/s0026 9-018-0970-1

Mao HK, Xu J, Bell PM (1986) Calibration of the ruby pressure gauge to 800 kbar under quasi-hydrostatic conditions. *J Geophys Res* 91: 4673-4676

Miyake M, Minato I, Morikawa H, Iwai S-I (1978) Crystal structures and sulphate force constants of barite, celestite, and anglesite. *Am Miner* 63:506–510

Prescher C, Prakapenka VB (2015) DIOPTAS: a program for reduction of two-dimensional X-ray diffraction data and data exploration. *High Press. Res*. 35:3, 223–230

Santamaria-Perez D, Chulia-Jordan R, Daisenberger D, Rodriquez-Hernandez P, Munoz A (2019) Dense Post-Barite-type Polymorph of $PbSO_4$ Anglesite at High Pressures. *Inorg. Chem*. 2019, 58, 2708-2716

Santamaria-Perez D, Gracia L, Garbarino G, Beltran A, Chulia-Jordan R, Gomis O, Errandonea D, Ferrer-Roca C, Martinez-Garcia D, Segura A (2011) High-pressure study of the

behavior of mineral barite by x-ray diffraction. *Physical Review B,* 054102, DOI: 10.1103/PhysRevB.84.054102

Sawchuk K, O'Bannon EF, Vennari C, Kavner A, Knittle E, Williams Q (2019) An infrared and Raman spectroscopic study of $PbSO_4$-anglesite at high pressures. *Physics and Chemistry of Minerals,* 46, 623-637. https://doi.org/10.1007/s00269-019-01027-z

Chapter 4 - An X-Ray Diffraction and Raman Spectroscopic Study of the High-Pressure Behavior of Gaspéite ($Ni_{0.73}Mg_{0.27}CO_3$)

4.1 Introduction

Carbonates are the main carriers of carbon into the deep Earth (Alt and Teagle, 1999; Dasgupta and Hirschmann, 2010). Studying the high-pressure behavior of carbonates is important for our understanding and modeling of the deep Earth carbon cycle. Many carbonates adopt a calcite structure, including first-row transition metal carbonates such as siderite ($FeCO_3$), rhodochrosite ($MnCO_3$), spherocobaltite ($CoCO_3$), and gaspéite ($NiCO_3$). First-row transition metals are important because they determine the thermodynamic properties of the minerals that contain them. Systematics amongst the properties of these divalent transition metal cations in a variety of mineral species at high pressures and temperatures provides information to contribute to models of the thermodynamic properties of their mixtures. Furthermore, experimental data on the phase stability and elastic properties of the transition metal carbonates are needed to compare with computational investigations of mineral species bearing divalent transitional metals.

Gaspéite ($NiCO_3$) is the nickel end-member of the calcite group. It has a hexagonal $R\bar{3}c$ unit cell comprised of six CO_3 trigonal ions and Ni^{2+} in 6-fold coordination with oxygen (Figure 4.1). Gaspéite, named after its place of discovery on the Gaspé Peninsula, has been a known member of the calcite group since its discovery in 1966 (Kohls and Rodda, 1966). Natural samples are uncommon and usually contain Mg substituting for the Ni, up to 43%. It forms from the weathering of nickel sulfides in supergene deposits with the most notable deposit of gaspéite located in the Western Australia nickel deposits (Thornber and Nickel, 1975). Previously, Zhang and Reeder (1999) studied gaspéite under pressures up to 8 GPa, saw no phase transformations,

and measured K_{0T} =131(1) GPa with K' fixed at 4. More recently, Chulia-Jordan et al. (2020) studied gaspéite with a composition of $Ni_{0.75}Mg_{0.25}CO_3$ to 20 GPa and experimentally determined K_{0T} =105(2) GPa, K'=7.4(3), and V_0=273.79(15) $Å^3$. Ab initio simulations also done in the same study on gaspéite with a composition of $Ni_{0.75}Mg_{0.25}CO_3$ calculated K_{0T} = 123.6 GPa and K'=4.6 given V_0=276.81 $Å^3$. Additionally, their ab initio simulations on pure $NiCO_3$ yielded K_{0T} = 129 GPa and K'=4.6 given V_0=273.95 $Å^3$.

Other carbonates with the $R\overline{3}c$ structure such as calcite, siderite, magnesite, rhodochrosite, and spherocobaltite have been studied extensively, but behave quite differently under high pressures. While work has been done on carbonates at both high pressure, ambient temperature and at high pressure, high temperature we will focus on studies at high pressure and room temperature for consistency with our high pressure, ambient temperature study. Calcite ($CaCO_3$) undergoes a series of phase transitions to CaCO3-II (1.5-2.5 GPa) CaCO3-III (2.5-15 GPa) and CaCO3-VI (15 GPa and above) (Merlini et al., 2012). Siderite ($FeCO_3$) has been shown to undergo a structural and electronic phase transition associated with its spin transition around 50 GPa (Fafan et al., 2012). We do not expect a spin transition to occur in the nickel carbonate as it contains 8 electrons in its d-orbital. Magnesite ($MgCO_3$) remains stable to 53 GPa (Fiquet, 1994), although changes at higher pressures and temperatures are known to occur (Gillet 1993, Isshiki et al., 2004). Spherocobaltite ($CoCO_3$) undergoes no transitions up to 56 GPa at ambient temperatures (Chariton et al., 2017). Rhodochrosite ($MnCO_3$) exhibits two phase transitions: one that initiates at 15 GPa and is not complete until 30 GPa, and another at 50 GPa (Farfan et al., 2013). The goal of our experimental work is to extend the study of gaspéite to higher pressures, determine its phase stability and elastic properties, and to investigate unifying trends amongst the calcite-structured transition metal carbonates.

4.2 Experimental Methods

4.2.1 Sample

The natural crystals of gaspéite used in these experiments are from the 132 North Ni Mine in Widgiemooltha, Australia (Nickel et al., 1994). These samples were obtained from the Sawchuk Mineral Collection (Specimen 5AB.008). Samples were bright green, translucent, and formed microcrystalline aggregates. All aliquots were obtained from a $3mm^3$ section of the sample.

The sample composition and structure was confirmed by examining separate aliquots of our starting sample at ambient pressure using Raman spectroscopy, scanning electron microscopy (SEM), and an X-ray diffraction measurement in a glass capillary tube. The Raman spectroscopy shows characteristic carbonate peaks. Analysis with a Tescan Vega-3 SEM with an energy dispersive analysis X-ray (EDAX) detector, an accelerating voltage of 20 kV, and calibrated with aluminum and copper, indicated a composition of $(Ni_{0.73}Mg_{0.27})CO_3$. X-ray diffraction determined a = 4.6111(4) Å, c = 14.805(4) Å, and V = 272.61(6) $Å^3$ at room pressure and temperature.

4.2.2 Synchrotron X-Ray Diffraction

Three high-pressure X-ray diffraction experiments were performed, each using a different aliquot of gaspéite from the same starting material. Runs 1 and 2 were performed at beamline 13-ID-D at GSECARS at the Advanced Photon Source (APS) in Chicago, IL and run 3 was performed at beamline 12.2.2 at the Advanced Light Source (ALS) in Berkeley, CA. In each experiment, symmetric type diamond anvil cells (DACs) with brilliant-cut diamonds with 250 μm culets were used to generate high pressures. A spring-steel gasket was pre-indented to a ~25

μm thickness and a 90 μm diameter hole was drilled through the gasket centered on the face of the diamonds to create a sample chamber. A small pellet of powdered gaspéite, approximately ~ 30 μm across and ~10 μm thick was placed inside this sample chamber. Additionally, a few small grains of ruby were placed in the sample chamber to be used as a pressure gauge (Mao et al., 1986). Finally, to maintain hydrostaticity during the experiment, a pressure-transmitting medium, gas-loaded Ne, was loaded into the sample chamber and the cell pressurized to ~1 GPa (Klotz et al., 2009).

Runs 1 and 2 were performed at beamline 13-IDD at GSECARS at the APS using a 37 KeV (0.3344 Å) light source with a beam size of approximately 3 μm x 3 μm at full width, half max. Diffraction patterns were collected for about 10 seconds on a Pilatus 3X CdTe 1M pixel array detector. Run 3 was performed at the ALS Beamline 12.2.2 using an incident X-ray wavelength of 0.4973 Å and a beam size of approximately 10 μm x10 μm. Patterns were collected for ~1-2 minutes on a two-dimensional MAR 345 imaging plate. Both detectors were calibrated using a CeO_2 standard powder. Calibration of the beam center, detector tilt, and distance from the sample to the detector was completed using the program DIOPTAS (Prescher and Prakapenka, 2015).

For each set of experiments, pressure was increased in ~2-5 GPa increments and diffraction patterns were obtained at every step up to 40 GPa at room temperature. In runs 1 and 2, data was only obtained on compression; in run 3 data was also obtained during decompression. During decompression, pressure was released in steps of ~5-10 GPa. Pressures were determined at each pressure step using ruby fluorescence. The Ne pressure medium provided an additional pressure calibration and was in good agreement with the pressure found using ruby fluorescence. Two-dimensional angle dispersive diffraction patterns were collected

and integrated using the DIOPTAS program to yield intensity versus two-theta diffraction patterns (Figure 4.2).

4.2.3 Raman Spectroscopy

The high-pressure Raman measurements were collected using a symmetric type DAC with brilliant-cut diamonds with 250-µm-diameter culets. Single crystals of gaspéite were loaded into a spring steel gasket pre-indented to ~25 μm thickness with a 90-µm hole that served as the sample chamber. A pressure media of either KCl (runs 1-3) or Ne gas (run 4) was used. Two to five small grains of ruby were included in the sample chamber to determine pressures using the standard ruby fluorescence technique (Mao et al., 1986). Raman spectra were collected at room pressure to 50.9 GPa using a Horiba LabRam HR Evolution Raman spectrometer. An excitation wavelength of 633 nm was used to collect spectra from 100-1250 cm^{-1} for durations of 30 seconds averaged over 30 collections. Peaks above 1250 cm^{-1} were not observed due to the strong Raman signal given by the diamonds. Pressure was increased in 1-2 GPa steps and in steps of ~5 GPa on decompression. The resolution of the Raman spectra was ~1 cm^{-1}. An Olympus BXFM-ILHS microscope equipped with a 50x long working distance objective was used to focus the laser onto the sample to a spot size of ~2 µm.

4.3 Results and Discussion

4.3.1 X-Ray Diffraction Results

At ambient conditions the lattice parameters of our sample of gaspéite are a = 4.6111(4) Å, c = 14.805(4) Å, and V = 272.61(6) $Å^3$. These values are in good agreement with previous measurements by Kohls and Rodda (1966). All three X-ray diffraction experiments

agree very well with each other, which confirms reproducibility between experiments. The positions and intensities of the observed diffraction peaks are consistent with the calcite structure, with no evidence of peak splitting or new peaks appearing up to the highest pressure reached in these experiments, 39.5 GPa (Figure 4.2). One new peak does appear around 14 GPa but this is associated with the Ne pressure medium becoming crystalline and nonhydrostatic (Klotz et al., 2009). This Ne peak disappears at approximately the same pressure upon decompression. Therefore, the diffraction patterns were indexed based on the $R\bar{3}c$ calcite structure and the center position of each peak was determined using a Gaussian fit. Corresponding *d*-spacings were calculated using Bragg's law. For each run, and at each pressure step, the first six diffraction peaks were used to calculate the best-fit calcite structure, $R\bar{3}c$, lattice parameters. These six peaks are associated with the following lattice planes: (012), (104), (110), (113), (202), and (024). We have chosen to exclude the (018) and (116) planes in our analysis: the peaks associated with these planes are both weak and very close to each other in two theta; resolving them as individual peaks was not possible. Assuming the combined peak to be the peak position of either the (018) or the (116) peaks leads to significant error in the volume determination. At higher pressures it may be possible to distinguish these peaks, but we are unable to due to the limited optical aperture of the DAC. Lattice parameters were calculated using the program Unit Cell (Holland and Redfern, 1997), yielding values for the lattice parameters *a*, *c*, and volume (table 4.1). On compression to our highest pressures of 39.5 GPa, gaspéite's a-axis decreases by 4%, c-axis by 7.4%, and it's c/a ratio by 3.5% (Figure 4.3). The decrease in c/a ratio with pressure follows a linear trend with an equation of: $y = -0.0057x + 3.202$. The c-axis is almost twice as compressible as the a-axis.

4.3.2 Equation of State of Gaspéite

Figure 4.4 shows a plot of unit cell volume as a function of pressure for all three experimental runs along with experimental data from Zhang and Reeder (1999) of end member $NiCO_3$, Chulia-Jordan et al. (2020) of $Ni_{0.75}Mg_{0.25}CO_3$, and Fiquet et al. (1994) of end member $MgCO_3$. We determined pressure-volume equations of state for each run separately. This approach has the benefit of providing an additional test of internal consistency amongst our three runs. To find the best-fit elastic parameters for each of our high-pressure runs, we use the Birch-Murnaghan equation of state to determine best fit values for V_0, K_{0T}, and K' (Birch, 1947). These values are shown in Table 4.2 and the fits are plotted as lines in figure 4.4. The values are consistent with each other and are well within mutual error bars. Combining all the three runs results in $K_{0T} = 136(4)$ GPa, $K'=4.6(3)$, and $V_0=271.8(3)$ $Å^3$. Our value for bulk modulus agree well with the value previously reported by Zhang and Reeder of $K_{0T} =131(1)$ GPa with an assumed K'=4. Additionally, our results agree well with ab initio simulations of gaspéite of a similar composition done by Chulia-Jordan et al. (2020) which report $K_{0T} = 123$ GPa and $K'= 4.6$ given $V_0= 276.81$ $Å^3$. We speculate that the high value of K'= 7.4(3) reported from the experimental data of Chulia-Jordan et al. (2020) may be due to difficulties resolving the (018) and (116) peaks which would create bias in the pressure dependence. Note that when we include the positions of the (018) and (116) peaks in our analysis we obtain a similarly high K' value to the one reported by Chulia-Jordan et al. (2020).

Within the first-row transition metal carbonates, Gaspéite is the least compressible; rhodochrosite ($MnCO_3$) has a $K_{0T} =107(11)$ GPa (Merlini et al., 2015), siderite ($FeCO_3$) has a $K_{0T} =110(2)$ GPa (Lavina et al., 2010), and spherocobaltite ($CoCO_3$) has a $K_{0T} =128(2)$ GPa (Chariton et al., 2017). This may be due to nickel's smaller cation radius which appears to lead

to an increase in bulk modulus (Figure 4.5). This has been suggested by previous studies as well (Zhang and Reeder, 1999 and Chariton et al., 2017).

4.3.3 Raman Results

A sample of the Raman spectra results obtained during this high-pressure study are shown in figure 4.6. Gaspéite exhibits four Raman active modes between 200-1250 cm^{-1} at ambient conditions. The first two modes are at low wavenumber and are associated with the translational ($E_g(T)$) and librational ($E_g(L)$) lattice vibration modes which are found, under ambient conditions, at 255.1 cm^{-1} and 362.9 cm^{-1}, respectively. The other two modes are associated with internal vibrations in the $(CO_3)^{2-}$. These are the CO_3 in-plane bending mode (v_4) which is found at 763.1 cm^{-1} under ambient conditions and the CO_3 symmetric stretching mode (v_1) which is at 1112.1 cm^{-1} under ambient conditions. Four experimental runs were carried out, three using KCl and one using a Ne pressure media. There appears to be very little difference between runs which confirms the reproducibility of the data and shows no variation between the KCl and Ne pressure media used. Pressures of up to 50 GPa were achieved, and no peak splitting, new peaks, or changes in slope with pressure were observed, suggesting no phase transitions occurred (Figure 4.7). All modes increase in wavenumber and become broader with increasing pressure, however, we have no trouble resolving them even up to the highest pressures achieved in the experiments. The intensity of both the $E_g(T)$ and $E_g(L)$ modes decrease visibly with pressure, this is especially true of the $E_g(T)$ mode. Peak broadening is also observed with increasing pressure for both the v_4 and v_1 modes. Wavenumbers corresponding to each vibrational mode (peak positions) were plotted as a function of pressure and increase smoothly with increasing pressure (Figure 4.7). The runs agree very well with each other, showing only a

1-2% offset between them. Additionally, within the runs the compression and decompression data agrees very well, indicating almost no hysteresis.

4.3.4 Isothermal Grüneisen Parameters

The mode Grüneisen parameter, γ_i, relates the isothermal change in frequency of mode i, v_i, to the change in volume, V, using the formula from Born and Huang, 1954:

$$\gamma_i = -\frac{V dv_i}{v_i dV}$$

The frequency was measured in our Raman experiments and the volume was calculated at each experimental Raman pressure step using our calculated equation of state. Our measured isothermal mode Grüneisen parameters are 1.69(4) for the E_g(T) mode, 1.68(3) for the E_g(L) mode, 0.42(1) for the v_4 mode, and 0.4(1) for the v_1 mode (Table 4.3). These values are in good agreement with other previously studied calcite-structured carbonates (Farsang et al., 2018). Figure 4.8 summarizes trends in zero-pressure frequency, unit cell volume, and mode Grüneisen parameter for lattice-mode vibrational trends amongst the transition metal calcite-structured carbonates. The ambient-pressure Raman mode frequencies decrease with increasing unit cell volume while the mode Grüneisen parameter tends to increase with increasing unit cell volume.

4.4 Implications and Concluding Remarks

In summary, our X-ray diffraction and Raman spectroscopy results indicate that gaspéite undergoes no phase transitions to 50 GPa and ambient temperatures. This is unlike the behavior of some calcite-structed carbonates such as calcite, siderite, and rhodochrosite; but is similar to the behavior of magnesite and spherocobaltite. The calcite-structured carbonate phase might be

stabilized at high pressure by the substitution of smaller cations such as Ni. This assertion is supported by the behavior of magnesite which is stable up to 110 GPa and 2200 K (Gillet 1993, Isshiki et al., 2004) and spherocobaltite, which is stable to 56 GPa and 1200 K (Chariton et al., 2017). The cation radii of Magnesium (0.72 Å) and cobalt (0.745 Å) are similar to that of nickel (0.69 Å). Nickel has the smallest cation of all the first-row transition metals forming calcite-structured carbonates, which suggests that the $R\bar{3}c$ nickel carbonate could be stable in the lower mantle. Extending the pressure and temperature range in future experiments on $NiCO_3$ may find that it is stable in the calcite-structure to the highest pressures of all the carbonates.

While $NiCO_3$ does not play an important role in the Earth, the behavior of Ni as a trace element in metal, silicate, oxide, and carbonate phases is important as a tracer for core/mantle formation and evolution processes. The phase stability, density, partitioning coefficient, and structure for the transition metal end-members provides important bounds on thermodynamic modeling of multicomponent systems. Therefore, information on the thermodynamic properties of $NiCO_3$ and other carbonates need to be available for predictions of high-pressure behaviors of carbonates at mantle and core conditions, which will aid in understanding the deep Earth carbon cycle.

Tables

	Pressure (GPa)	a (Å)	c (Å)	V (Å^3)
Run 1 (APS)	0.8	4.6048 (4)	14.733 (4)	270.55 (6)
	3	4.5912 (3)	14.592 (4)	266.37 (5)
	4.75	4.5740 (3)	14.496 (4)	262.65 (5)
	12.5	4.5385 (3)	14.1605 (4)	252.60 (5)
	18.3	4.4969 (3)	13.996 (4)	245.11 (5)
	30.5	4.4565 (3)	13.487 (3)	231.97 (4)
	37.7	4.4423 (3)	13.280 (3)	226.96 (4)
Run 2 (APS)	0.75	4.6028 (3)	14.746 (4)	270.55 (6)
	1.11	4.5992 (3)	14.723 (4)	269.71 (6)
	1.3	4.5982 (3)	14.699 (4)	269.15 (6)
	1.86	4.5951 (3)	14.669 (4)	268.23 (5)
	2.77	4.5874 (3)	14.606 (4)	266.18 (5)
	3.6	4.5808 (3)	14.581 (4)	264.97 (5)
	4.8	4.5727 (3)	14.513 (4)	262.80 (5)
	6.6	4.5596 (4)	14.4681 (4)	260.50 (6)
	10.5	4.5375 (4)	14.303 (4)	255.02 (6)
	13.2	4.5206 (3)	14.154 (4)	250.49 (6)
	15.1	4.5132 (3)	14.058 (4)	247.98 (6)
	18.1	4.4982 (3)	13.968 (4)	244.76 (5)
	23	4.4784 (3)	13.813 (4)	239.92 (5)
Run 3 (ALS)	0.5	4.6119 (4)	14.752 (4)	271.74 (6)
	5.6	4.5669 (3)	14.442 (4)	260.85 (5)
	14.1	4.5255 (3)	14.111 (4)	250.28 (5)
	16.1	4.5178 (3)	13.999 (4)	247.44 (5)
	19	4.5117 (3)	13.879 (3)	244.66 (5)
	23.3	4.4844 (3)	13.723 (3)	239.00 (5)
	26.3	4.4739 (3)	13.654 (3)	236.67 (5)
	30.1	4.4612 (3)	13.526 (3)	233.14 (5)
	33.2	4.4525 (3)	13.413 (3)	230.28 (5)
	36.8	4.4422 (3)	13.309 (3)	227.45 (5)

Table 4.1 Values for a, c, and volume of gaspéite under pressure across all experiments.

Experiment	K (GPa)	K'	Vo (Å^3)
Run 1	140 (12) GPa	4.27 (8)	271.87 (8)
Run 2	136.9 (8.6) GPa	4.49 (5)	272.09 (7)
Run 3	136.4 (4.2) GPa	4.39 (5)	271.7 (2)

Table 4.2 Bulk modulus (K), its pressure derivative (K'), and initial volume of gaspéite (NiCO$_3$) for different experiments

Observed Mode	γ	v_i (cm^{-1})
Eg(T)	1.69 (4)	257 (1)
Eg(L)	1.68 (3)	365 (1)
v_4	0.42 (1)	762 (1)
v_1	0.40 (1)	1107 (1)

Table 4.3 Isothermal Gruneisen parameters for the observed NiCO$_3$ Raman modes and the initial frequency.

Figures
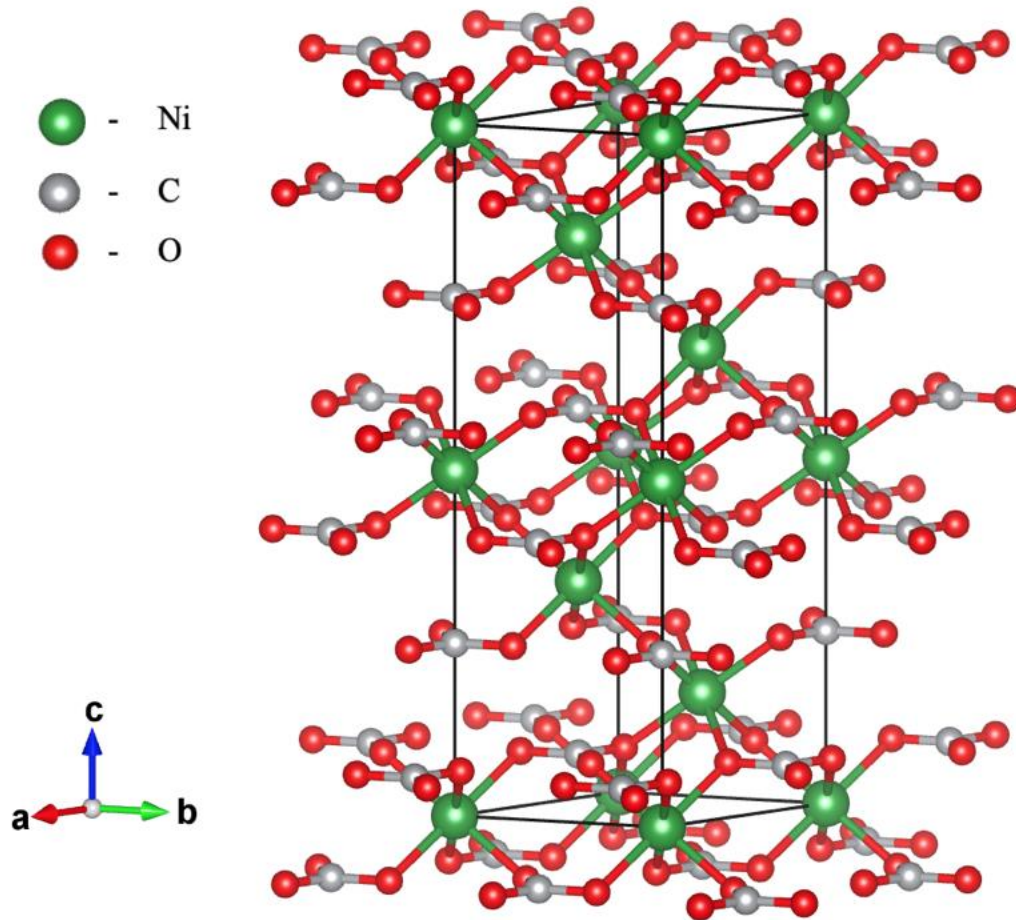
Figure 4.1 Crystal structure of gaspéite NiCO₃, unit cell outlined in black. Crystal structure diagram generated using VESTA (Momma and Izumi, 2011 and Graf, 1961)
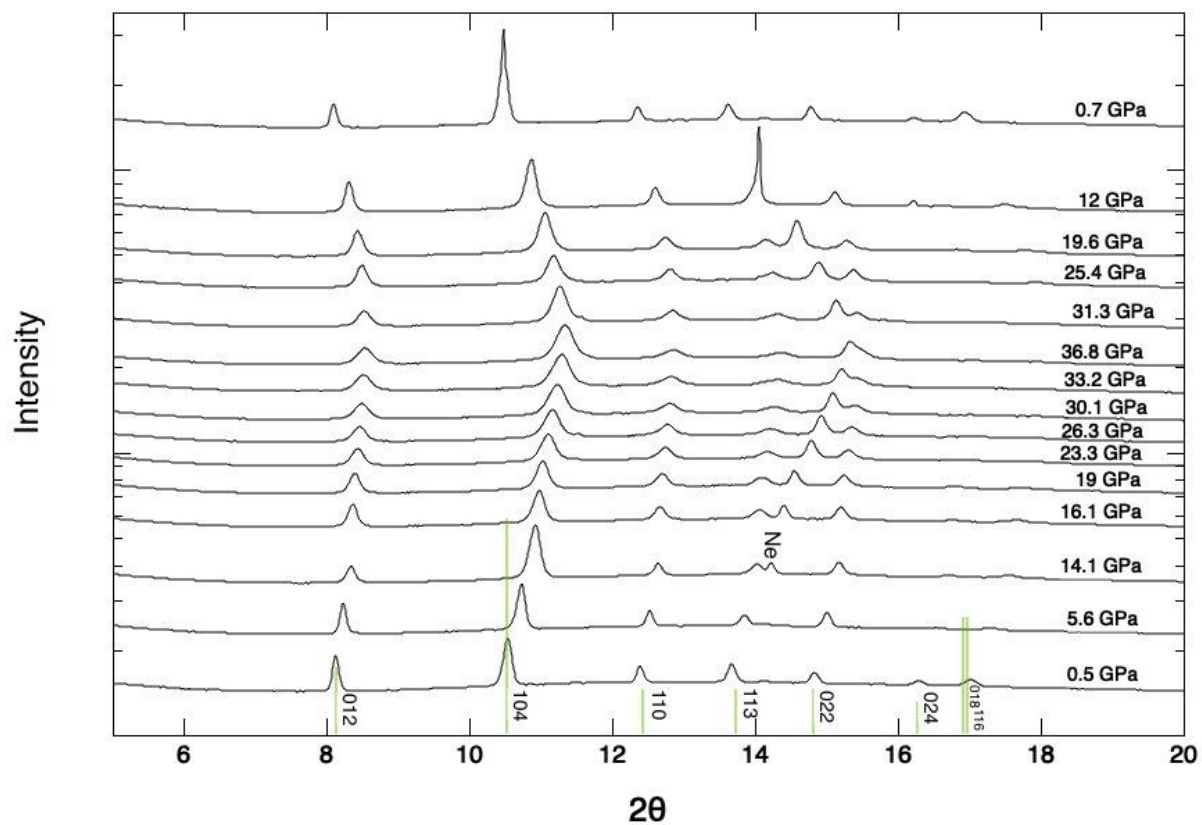
Figure 4.2 X-ray diffraction pattern of gaspéite (NiCO$_3$) under compression to 35 GPa and decompression. Run 3, ALS. Lines indicate indexed peak positions of gaspéite. $\lambda = 0.4977$Å
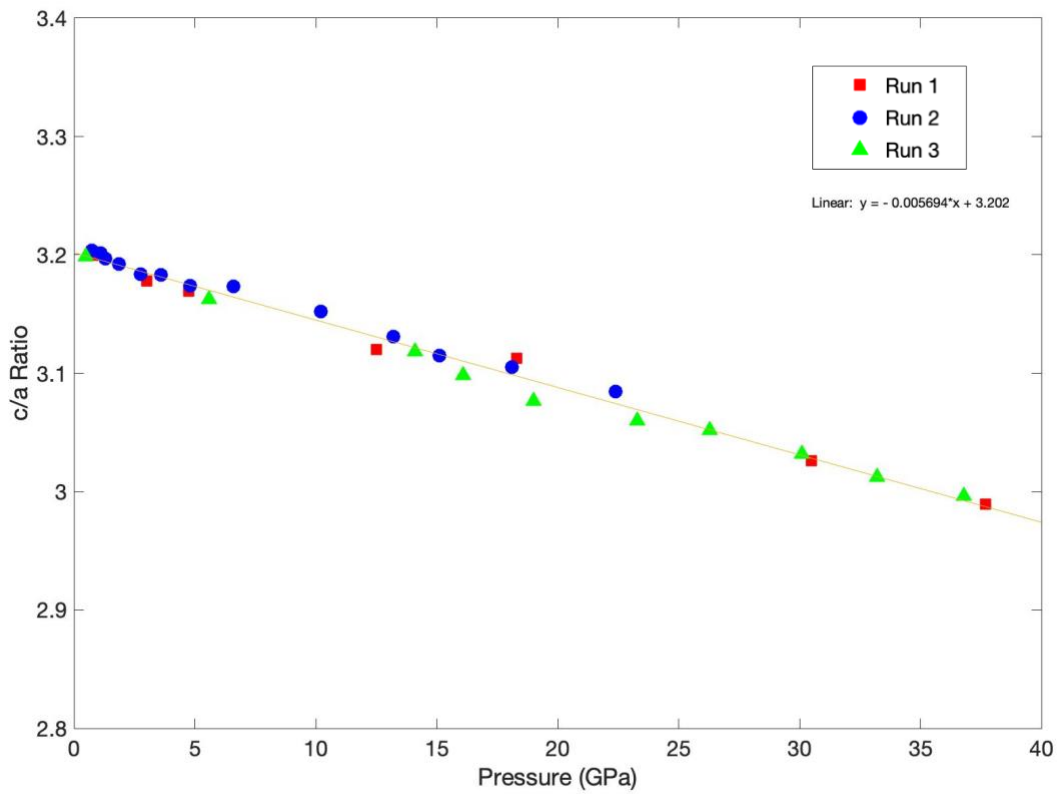
Figure 4.3 C/A ratio of gaspéite (NiCO$_3$) under compression and decompression for all experiments. Squares are run 1 on compression, circles are run 2 on compression, triangles are run 3 on compression
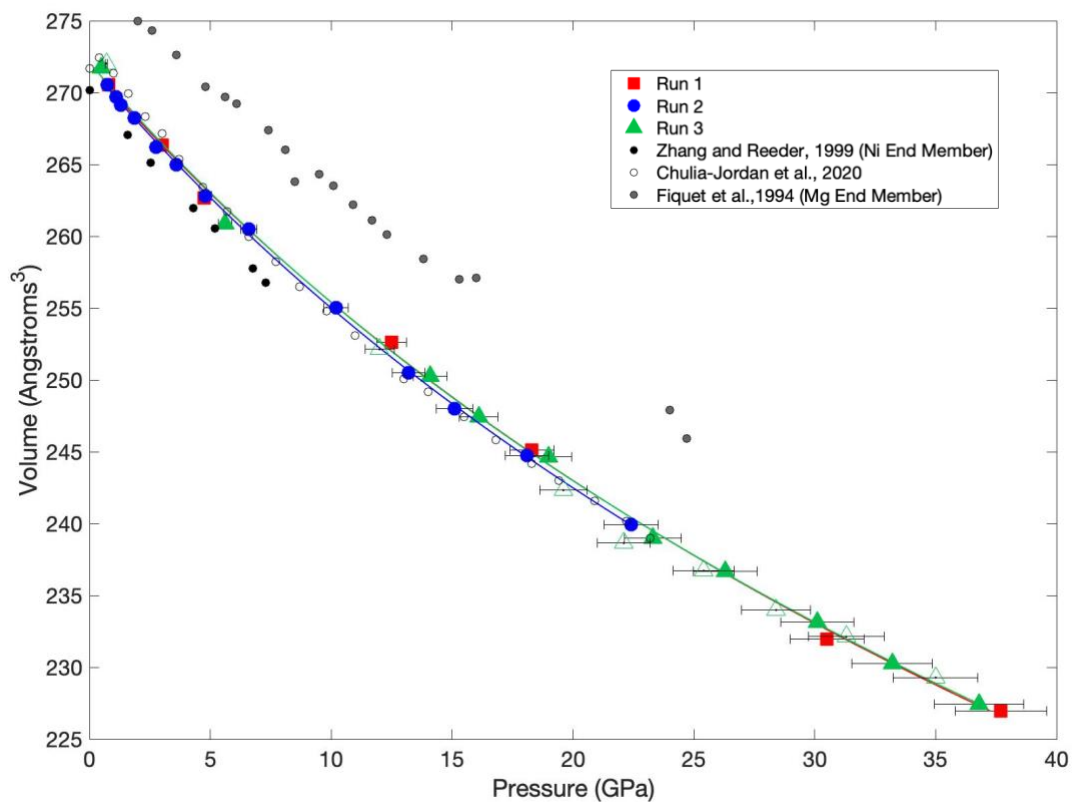
Figure 4.4 Volume changes of gaspéite (NiCO₃) under compression and decompression for our experiments. Squares are run 1 on compression, circles are run 2 on compression, triangles are run 3 on compression, open triangles are run 3 on decompression. Error bars for pressure shown, error bars for volume are smaller than markers. Smaller black circles are nickel end member data from Zhang and Reeder, 1999. Smaller white circles are Ni$_{0.75}$Mg$_{0.25}$CO₃ data from Chulia-Jordan et al. (2020). Smaller gray circles are magnesium end member data from Fiquet et al., 1994
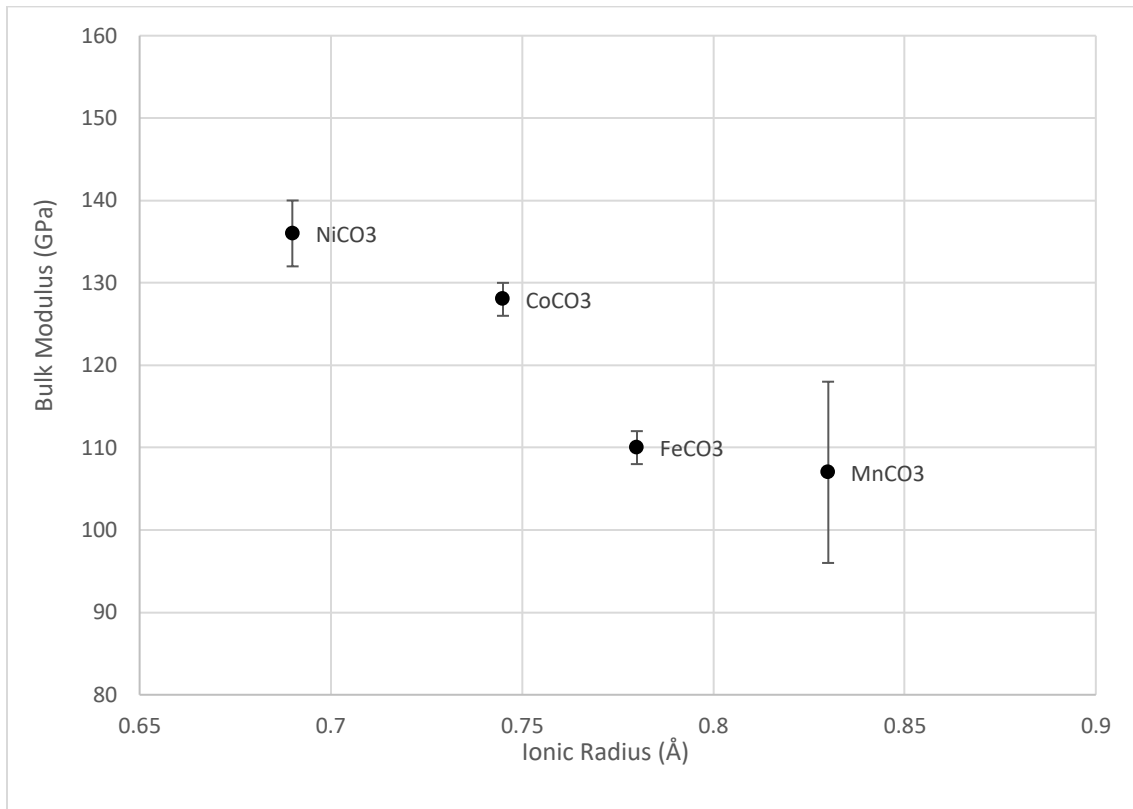
Figure 4.5 Bulk modulus as a function of cation radius for the calcite-structured transition metal carbonates: Gaspéite (NiCO$_3$, This study), Spherocobaltite (CoCO$_3$, Chariton et al., 2017), Siderite (FeCO$_3$, Lavina et al., 2010), and Rhodochrosite (MnCO$_3$, Merlini et al., 2015). Radii from Shannon, R.D., 1976
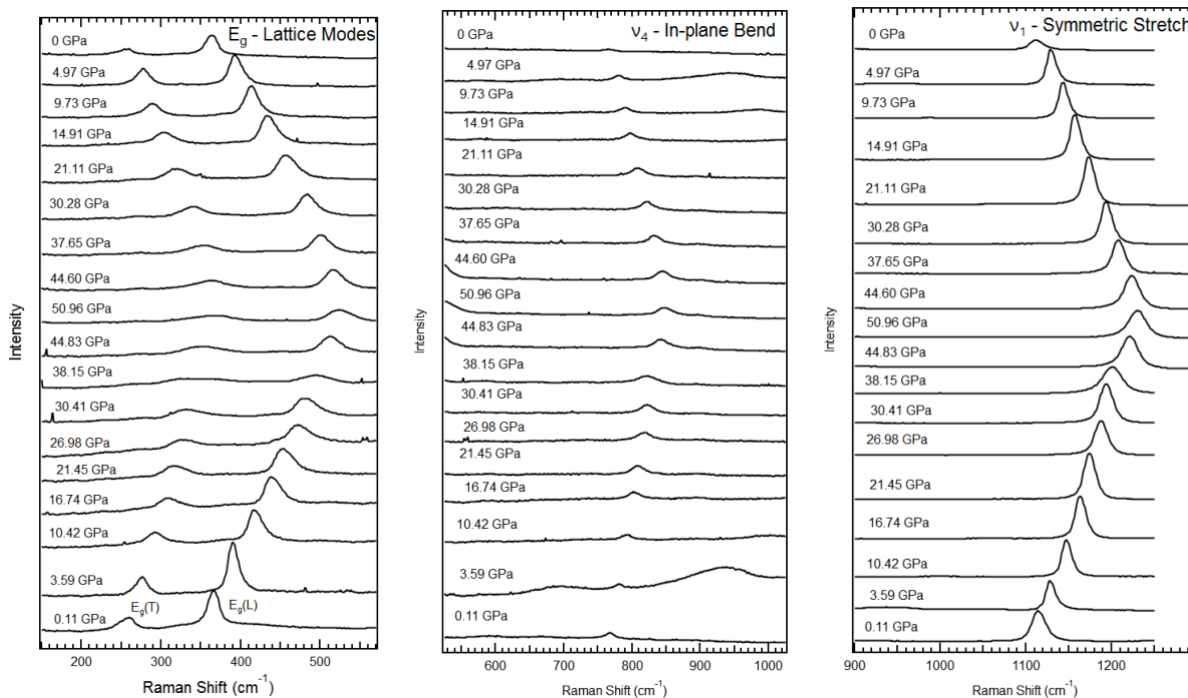
Figure 4.6 Raman Spectra of gaspéite (NiCO₃) for all 4 observed modes under compression to 50.9 GPa and decompression
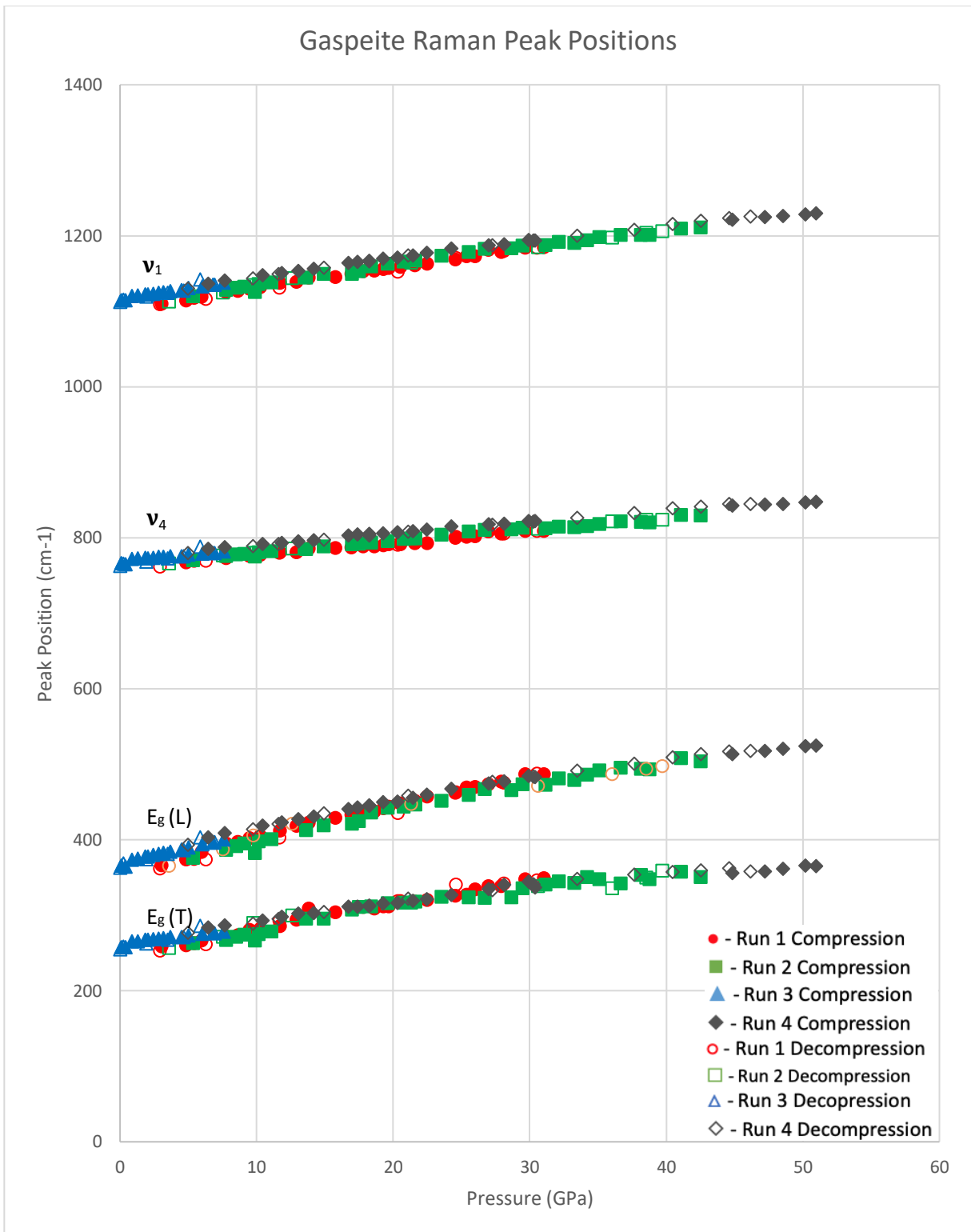
Figure 4.7 Peak position with pressure for the observed Raman peaks on compression and decompression. Closed symbols represent compression while open symbols represent decompression. Error bars are smaller than symbols
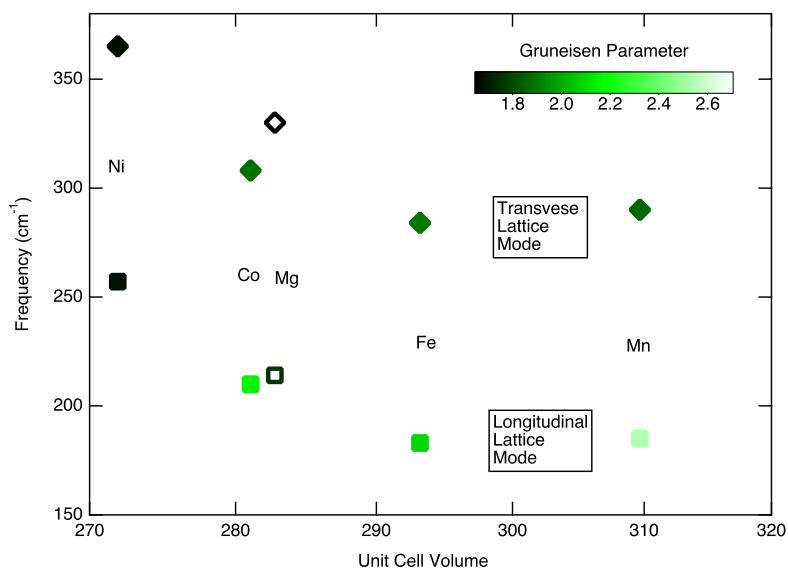
Figure 4.8 Raman frequencies plotted as a function of unit cell volume for lattice modes for calcite-structured carbonates. Data for $MgCO_3$, $MnCO_3$, and $FeCO_3$ from Farfan et al. 2013. Data for $CoCO_3$ from Chariton et al. 2017. $NiCO_3$ data from this study. Shading shows the Grüneisen parameter corresponding to each mode

4.5 References

Alt JC, Teagle DAH (1999) The uptake of carbon during alteration of the oceanic crust. *Geochemica et Cosmochimica Acta*, 63, 1527-1535.

Born M and Huang K (1954) Dynamical theory of crystal lattices. Clarendon Press.

Birch F (1947) Finite elastic strain of cubic crystals. *Phys Rev* 71:809

Chariton S, Cerantola V, Ismailova L, Bykova E, Bykov M, Kupenko I, McCammon C, Dubrovinsky L (2017) The high-pressure behavior of spherocobaltite ($CoCO_3$): a single crystal Raman spectroscopy and XRD study. *Physics and Chemistry of Minerals* DOI: 10.1007/s00269-017-0902-5

Chulia-Jordan R, Santamaria-Perez D, Ortero-de-la-Roza A, Ruiz-Fuertes J, Marqueno T, Gomis O, MacLeod S, Popescu C (2020) Phase Stability of Natural $Ni_{0.75}Mg_{0.22}Ca_{0.03}CO_3$ Gaspeite Mineral at High Pressure and Temperature. *The Journal of Physical Chemistry C* 2020 124 (36), 19781-19792.

Dasgupta R, Hirschmann MM (2010) The deep carbon cycle and melting in Earth's interior. *Earth and Planetary Science Letters* 298: 1-13

Farfan G, Wang S, Ma H, Caracas R, Mao W (2012). Bonding and structural changes in siderite at high pressure. *American Mineralogist.* Volume 97, Issue 8-9, pp. 1421-1426.

Farfan GA, Boulard E, Wang S, Mao WL (2013). Bonding and electronic changes in rhodochrosite at high pressure. *American Mineralogist.* Volume 98, pp. 1817-1823.

Farsang S, Facq S, Redfern SAT (2018). Raman modes of carbonate minerals as pressure and temperature gauges up to 6 GPa and 500 C. *American Mineralogist.* Volume 103, pp.1988-1998.

Fiquet G, Guyot F, Itie JP (1994). High Pressure X-ray Diffraction Study of Carbonates: $MgCO_3$,

CaMg(CO$_3$)$_2$, and CaCO$_3$. *American Mineralogist*, Volume 79, pp.15-23

Gillet P (1993). Stability of magnesite (MgCO$_3$) at mantle pressure and temperatures conditions:
A Raman spectroscopic study. *American Mineralogist*. Volume 78, Issue 11-12, pp.
1328-1331.

Graf (1961) Crystallographic tables for the rhombohedral carbonates. *American Mineralogist*.
Volume 46, Issue 11-12, pp. 1283-1316.

Holland TJB and Redfern SAT (1997) Unit cell refinement from powder diffraction data: the use
of regression diagnostics. *Mineralogical Magazine* 61: 65-77.

Isshiki M, Irifune T, Hirose K, Ono S, Ohishi Y, Watanuki T, Nishibori E, Takata M, Sakata M
(2004) Stability of magnesite and its high-pressure form in the lowermost mantle. *Nature*
Vol. 427 pp. 60-63

Klotz S, Chervin JC, Munsch P, Marchand GL (2009) Hydrostatic limits of 11 pressure
transmitting media. *J. Phys. D: Appl. Phys*. 42 075413 DOI:10.1088/0022-
3727/42/7/075413

Kohls DW and Rodda JL (1966) Gaspéite (Ni, Mg, Fe) (CO$_3$), A new carbonate from the Gaspé
peninsula, Quebec. *American Mineralogist* 51: May-June pp. 677-684

Lavina B, Dera P, Down RT, Yang W, Sinogeikin S, Meng Y, Shen G, Schiferl D (2010)
Structure of Siderite FeCO$_3$ to 56 GPa and hysteresis of its spin-pairing transition.
Physical Review B 82, 0641110.

Mao HK, Xu J, Bell PM (1986) Calibration of the ruby pressure gauge to 800 kbar under quasi-
hydrostatic conditions. *J Geophys Res* 91: 4673-4676

Merlini M, Hanfland M, and Crichton WA (2012). $CaCO_3$-III and $CaCO_3$-VI, high-pressure
    polymorphs of calcite: Possible host structures for carbon in the Earth's mantle. *Earth*
    and Planetary Science Letters. Volume 333-334, pp. 265-271.

Merlini M, Hanfland M, Gemmi M (2015) The $MnCO_3$-II high-pressure polymorph of
    rhodochrosite. *American Mineralogist* Volume 100, pages 2625-2629.

Momma K and Izumi F (2011) VESTA 3 for three-dimensional visualization of crystal,
    volumetric and morphology data. *J. Appl. Crystallogr* 44: 1272-1276

Nickel EH, Clout JFM, Gartrell BJ (1994) Secondary nickel minerals from Widgiemooltha.
    Mineralogical Record; Bowie Vol. 25, Iss. 4, (July, 1994): 283

Prescher C, Prakapenka VB (2015) DIOPTAS: a program for reduction of two-dimensional X-
    ray diffraction data and data exploration. *High Press. Res*. 35:3, 223–230.

Shannon RD (1976) Revised Effective Ionic Radii and Systematic Studies of Interatomic
    Distances in Halides and Chalcogenides. *Acta Cryst*. A32, 751, pp. 751-767.

Thornber MR and Nickel EH (1976) Supergene Alteration of Sulphides. III. The Composition of
    Associated Carbonates. *Chemical Geology*, 17(1976)45-72 pp. 45-72.

Zhang J and Reeder R (1999) Comparative compressibilities of calcite-structured carbonates:
    Deviations from empirical relations. *American Mineralogist*. Volume 84, Issue 5-6, pp.
    861-870.

Chapter 5 - Manganese Metal Reactions with CO_2 at High Pressures and Temperatures

5.1 Introduction

The study of carbon in the deep Earth is important in understanding the global carbon cycle. It is generally accepted that more carbon enters the deep Earth through subduction than is released back to the surface (Dasgupta and Hirschmann, 2010; Kelemen and Manning, 2015). Therefore, the study of mineral phases that could store carbon in the deep Earth are of particular interest. Depending on the local chemistry, carbon could be in an oxidized phase such as a carbonate or a reduced phase such as graphite or diamond (McCammon, 2005; Dasgupta and Hirschmann, 2006; Dasgupta, 2013). All of these phases have been observed in diamond inclusions, suggesting a very complicated redox environment in the mantle (Wirth et al., 2009; Kaminsky and Wirth, 2011; Logvinova et al., 2019). Determining carbon-bearing mineral phases in the deep Earth requires knowledge of the relative stability field of metals, oxides, and carbonate phases, along with the high-pressure thermoelastic properties of those phases. One way to accomplish this is to study reactions at mantle conditions between CO_2 and elements that are abundant in the mantle to determine their preference to form an oxide or a carbonate. The results of these reactions will give insight into stable carbon-bearing phases and may one day be used in constructing mantle phase stability diagrams. A long-term goal in the mineral physics community is to determine the phase stability and thermoelastic properties of all metals, oxides, and carbonates; these experiments will provide information to achieve this goal.

How transition metals (such as iron, nickel, and manganese) behave under deep Earth conditions are of particular interest. Transition metals will often determine the thermodynamic properties of the minerals that contain them. The study of transition metals at high-pressures and

temperatures are important because they may provide insight into trace element cycling in the deep Earth. Investigating transition metals will also provide information on transition metal mineral phase stability and thermoelastic properties which are needed for computational investigations. Additionally, knowledge of the high pressure and temperature behavior of a variety of transition metal-bearing minerals will provide information about systematic trends in thermodynamic properties with varying cation sizes. We chose to study the transition metal manganese because it is one of the most abundant transition metal geochemical tracers; it readily forms a carbonate at ambient pressure; and its high-pressure metal, carbonate, and oxide densities and equation of state parameters are relatively well known.

Manganese has been studied under high pressure by Fujihisa and Takemura (1995), under high temperature by Persson and Ohman (1929), and under high temperature and pressure by Rapoport and Kennedy (1966). Fujihisa and Takemura studied manganese metal at ambient temperature and high pressure up to 190 GPa. In their study, they calculated a $K_{0T} = 148$ GPa and a $K' = 4.6$ for the α-manganese phase and found a phase transition that occurs above 165 GPa. Persson and Ohman (1929) studied manganese metal at high temperatures and found a high temperature phase transition from α-manganese to β-manganese after heating around 1005 K. This transition reverts to the α-manganese structure on cooling. Additionally, manganese transform to γ-manganese after heating around 1470 K. This transition also reverts to α-manganese after cooling. Rapoport and Kennedy (1966) studied the high temperature structures of manganese under pressures of up to 4 GPa and temperatures up to 1300 K. In their study, they observed the transition temperatures for both β- and γ-manganese increase significantly at high pressure.

Previous studies on reactions between CO_2 and transition metals have suggested the formation of both oxides and carbonates. Theoretical calculations at ambient pressures have suggested CO_2 is absorbed readily by iron, cobalt, and nickel while copper only weakly interacts with CO_2 (Liu et al., 2012). In the case of nickel, it has been shown this absorption forms a carbonate (Solymosi, 1991). Santamaria-Perez et al. (2016) previously studied high-pressure and temperature reactions between transition metals and carbon dioxide in the diamond anvil cell. In their study, they explored carbon dioxide reactions with rhenium, gold, and platinum. Above 8 GPa and 1500 K rhenium reacted with the carbon dioxide to form an oxide. However, gold and platinum had no reactions with carbon dioxide up to the highest pressure and temperature studied: 48 GPa and 2400 K. In our studies, we expect reactions between CO_2 and manganese metal to form an oxide or a carbonate:

$$2Mn + CO_2 \rightarrow 2MnO + C$$

$$2Mn + 3CO_2 \rightarrow 2MnCO_3 + C$$
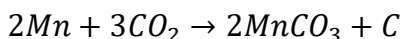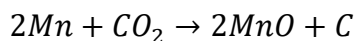
In both cases, we expect the formation of diamond, however detecting diamond as a reaction product is difficult as it will likely nucleate of the face of the diamond anvils.

5.2 Experimental Methods

The metallic manganese, iron, and nickel samples used in these experiments were obtained from Alfa Aesar and were of at least 99.9% purity. The sample of manganosite was a ~4mm^3 fragment obtained off of a natural sample in the UCLA mineral collection (specimen MS 576). The sample was from Franklin, New Jersey. Crystals were dark green and coexisted with zincite and magnetite. Sample identity was confirmed using Raman spectroscopy and X-ray diffraction. This sample of manganosite was then crushed into a powder.

To generate high pressures during the experiments, symmetric type diamond anvil cells (DACs) with brilliant-cut diamonds with 250 μm culets were used. A spring-steel gasket was pre-indented to a ~25 μm thickness and a 90-μm diameter hole was drilled through the gasket centered on the face of the diamonds to create a sample chamber. The powdered sample was then pressed into a pellet approximately 30 μm across and 10 μm thick. This pellet was placed into the sample chamber along with a few grains of ruby which were used as a pressure gauge (Mao et al., 1986). The rest of the sample chamber was gas-loaded with high-purity CO_2 using the COMPRES gas loading apparatus, this was done to maintain hydrostaticity during the experiment and also serve as a reactant during the experiment. Finally, the cell was pressurized to its target pressure.

All high pressure, high temperature experimental reaction runs were performed at beamline 12.2.2 at the Advanced Light Source (ALS) in Berkeley, CA. Beamline 12.2.2 has an incident X-ray wavelength of 0.4973 Å and a beam size of approximately 10 μm x10 μm. Patterns were collected before and after heating for ~1-2 minutes on a two-dimensional MAR 345 imaging plate. The detector was calibrated using a CeO_2 standard powder. Calibration of the beam center, detector tilt, and distance from the sample to the detector was completed using the program DIOPTAS (Prescher and Prakapenka, 2015).

In each experimental run the pressure was increased to its target pressure (6, 23, and 44 GPa for manganese metal, 14.5 and 30 GPa for manganese oxide) and a diffraction pattern was obtained. The sample was then brought to high temperatures to promote reactions between the sample and CO_2. This was achieved by double-sided laser heating using an infrared ($\lambda = 1.09$μm) continuous wave fiber laser operating in Gaussian mode. Temperatures were determined by spectroradiometry using a peak scaling method, this utilizes the average temperature over the

entire hotspot, the peak temperature, and the two dimensional intensity gradient. Further information about the laser heating system and temperature measurements can be found in Rainey and Kavner (2014) and in Kunz et al. (2018). Heating of the sample occurred for ~2-3 minutes during which, the sample was rastered by the laser to promote reactions in as much of the sample as possible. After heating, the sample was quenched and diffraction patterns were taken in multiple parts of the sample. The collected diffraction patterns were integrated using the DIOPTAS program to yield intensity versus two-theta diffraction patterns. These patterns were indexed using known patterns of metals, carbonates, and oxides in order to determine the reaction products during the experiments.

5.3 Results and Discussion

5.3.1 Manganese Metal Reactions

Reaction experiments between manganese metal and CO_2 were carried out at 6, 23, and 44 GPa. Figure 1 shows diffraction patterns taken at 6 GPa before and after heating to 2000 K. Figure 2 shows the 6 GPa diffraction pattern after heating with the caked diffraction image in the background. After heating, new peaks appear in the diffraction pattern that were identified as the manganese carbonate, rhodochrosite. Figure 3 shows diffraction patterns taken at 23.5 GPa before and after heating to 2000 K. Figure 4 shows the 23.5 GPa diffraction pattern after heating with the caked diffraction image in the background. At this pressure and temperature the formation of rhodochrosite is also observed. Differences in intensity between these two pressure steps is likely due to different orientations of manganese metal grains. In order to confirm the presence of rhodochrosite after heating at 6 and 23.5 GPa we compare our results to a previous study by Farfan et al. (2013). Figure 5 shows a figure by Farfan et al. (2013) of three diffraction

peaks of rhodochrosite at high pressure. We have overlain the new peaks we observed in our diffraction patterns, and identify as rhodochrosite, for comparison. The peaks we observe in our post-heating patterns match well with rhodochrosite's high-pressure behavior. Therefore, we are confident that reactions between manganese metal and CO_2 form rhodochrosite. We also compare the high-pressure behavior of manganese metal to a previous study by Fujihisa and Takemura (1995). Figure 6 shows a figure by Fujihisa and Takemura (1995) of their equation of state of manganese metal at high pressure. We have added our data points for comparison, which agree very well.

A reaction experiment was also performed at 44 GPa and 2500 K (Figure 7, 8). Unlike previous experiments, we were unable to determine the reaction products. The pre-heat pattern shows characteristic manganese metal peaks. However, many new peaks appear in the quenched pattern. Some of these peaks could be associated with rhodochrosite but many of the other peaks cannot be matched with manganese metal or rhodochrosite. Farfan et al. (2013) reports a phase transition in rhodochrosite above 50 GPa; while our experiment is below this pressure, the unknown hydrostaticity of CO_2 may cause nonhydrostatic stresses resulting in the phase transition initiating at lower pressures. Additionally, Boulard et al. (2016) observes drastic changes in rhodochrosite at 45 GPa and 1400 K. At this pressure and temperature they observe the high-pressure phase of rhodochrosite and a manganese oxide form after heating. However, in their study, they used NaCl and KCl pressure media which would change the redox environment of their experiment compared to our experiments which use a CO_2 pressure medium. We also speculate that manganese metal may have undergone structural changes at this pressure and temperature. While manganese metal has been studied extensively under high pressures (Fujihisa and Takemura, 1995), under high temperature (Persson and Ohman, 1929), and under

high temperature and low pressure (Rapoport and Kennedy, 1966), there have been no higher

pressure, high temperature studies. Without a high pressure, high temperature study of

manganese metal we cannot be sure of the reaction products at 44 GPa and 2500 K.

5.3.2 Manganese Oxide Reactions

Reaction experiments were also carried out between manganese oxide and CO_2 at 14.5

and 30 GPa and 2000 K (Figure 9). This was done as a secondary check on the results of the

manganese metal reaction experiments. Since manganese metal and CO_2 form a carbonate, it is

expected that a manganese oxide and CO_2 would form a carbonate as well. This experiment was

performed at 2000 K and two pressure steps: 14.5 and 30 GPa. At both pressure steps new peaks

appear in the post-heating diffraction pattern that can be indexed as rhodochrosite. The switch

from oxide to carbonate confirms that rhodochrosite is the more stable phase at these pressures

and temperatures. Additionally, this may represent a more realistic reaction that could happen in

the mantle.

5.3.3 Reactions with Other Transition Metals

We have carried out preliminary reaction experiments between CO_2 and other first-row

transition metals: iron at 42.5 GPa and nickel at 40 GPa. In both experiments, after heating to

2500 K, we observe the formation of their respective carbonates.

Diffraction patterns for iron and CO_2 at 42.5 GPa before and after heating are shown in

figure 10. Figure 11 shows the after heating pattern with the caked diffraction image in the

background. After heating, new peaks appear that are consistent with the iron carbonate,

siderite. At this pressure siderite is in its ambient-pressure $R\bar{3}c$ structure, previous studies do not

see any phase transitions until 46 GPa (Farfan, et al., 2012). Therefore, the diffraction positions for calcite-structured siderite are included in both figure 10 and 11, and are a good match for the new peaks that appear after heating.

Figure 12 shows diffraction patterns for nickel and CO_2 at 40 GPa before and after heating. Figure 13 shows the after-heating pattern with the caked diffraction image in the background. After heating at this pressure, new peaks appear that match well with the nickel carbonate, gaspéite, which remains in its ambient-pressure $R\overline{3}c$ structure at 40 GPa (Sawchuk, et al., 2021). Diffraction positions for the nickel carbonate are shown in both figure 12 and 13.

5.4 Implication and Concluding Remarks

In summary, we have carried out reaction experiments between CO_2 and first row transition metals that are abundant in the Earth: manganese, iron, and nickel. Using X-ray diffraction, we have identified carbonates as the products of reactions between CO_2 and the transition metals: manganese, iron, and nickel, at pressures and temperatures relating to the upper mantle. Additionally, reactions between CO_2 and the manganese oxide, manganosite, also produce a carbonate. Determining the reaction products in these experiments informs us of relative phase stability of oxide and carbonate phases. These results suggest that carbonates are a stable phase in the mantle and could therefore store carbon in the deep Earth. To better understand the stability of carbonates in the mantle, future studies should focus on conducting systematic reaction experiments across a wide range of pressures and temperatures. Ultimately, this information could be used to create mantle phase stability diagrams. While reactions between CO_2 and transition metals are likely a simplification of reactions that may be taking

101

place in the mantle, they can provide useful insights into the stability of end-member carbonates
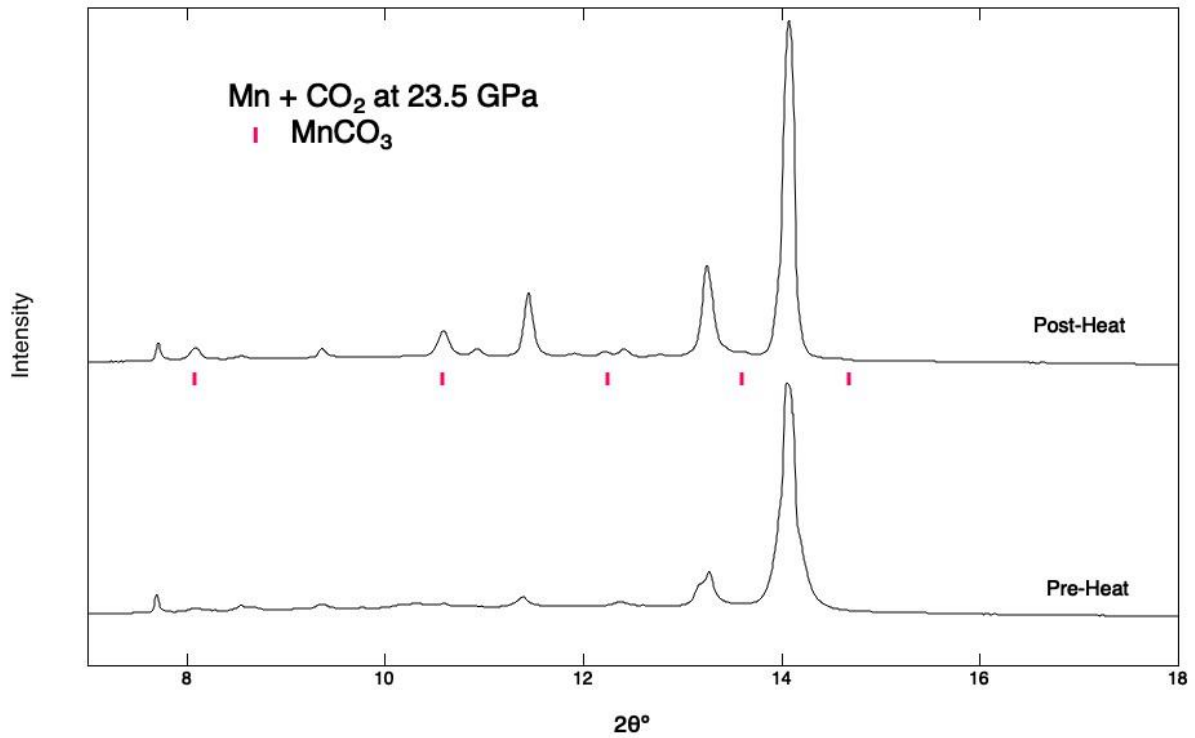
and oxides in the mantle.

Figures
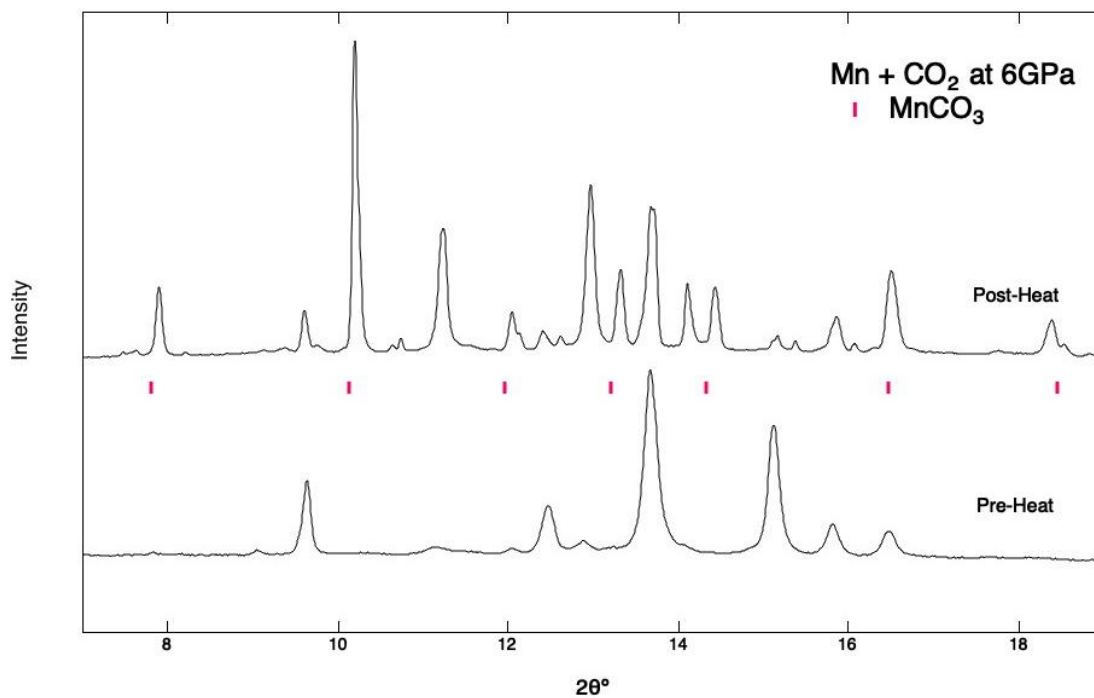
Figure 5.1 Manganese and CO_2 at 6 GPa before and after heating to 2000K. Rhodochrosite peaks marked in pink
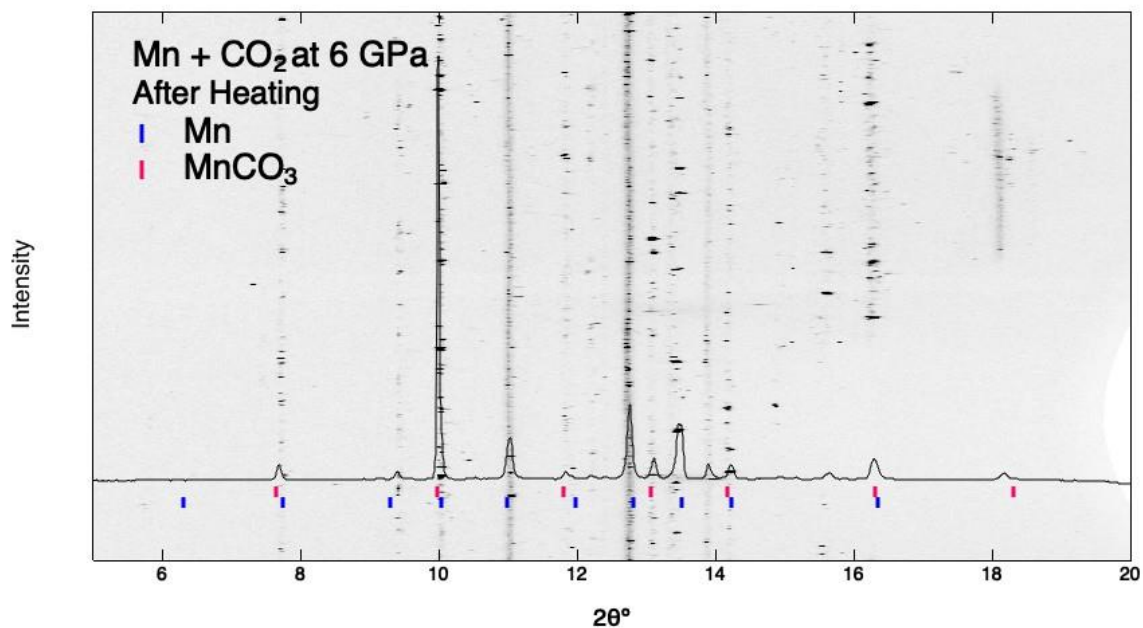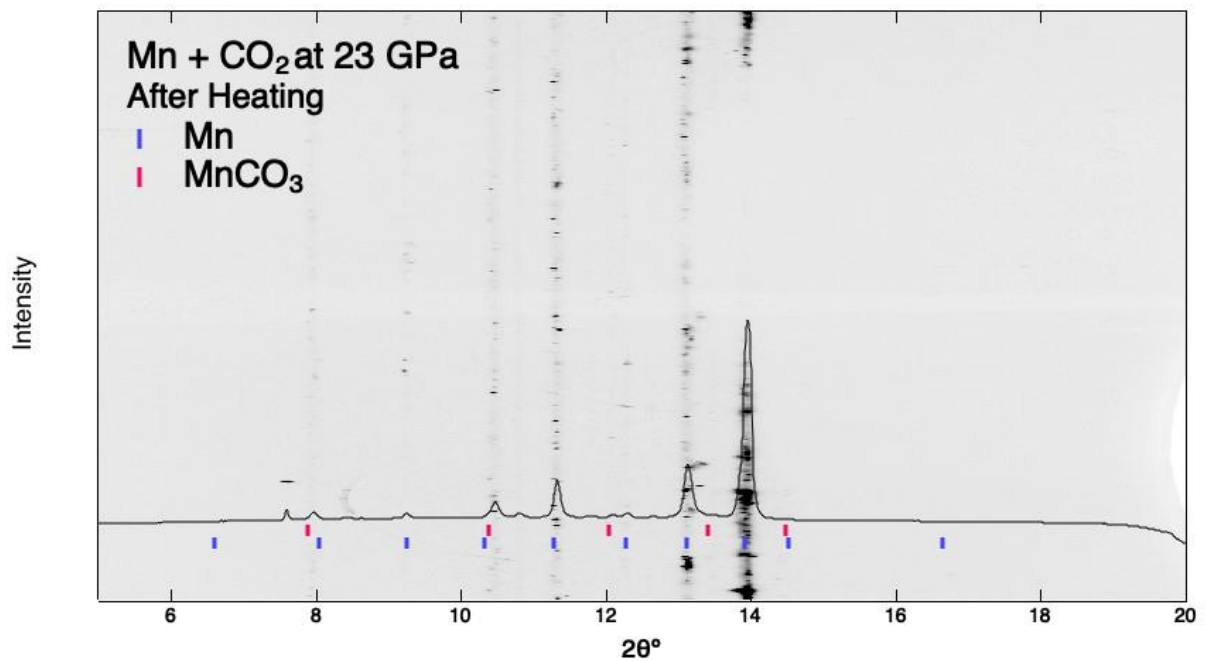

Figure 5.2 Diffraction pattern of manganese and CO_2 reactions after heating with caked diffraction image in background. Diffraction positions for manganese metal in blue and for rhodochrosite in pink.

Figure 5.3 Manganese and CO_2 at 23.5 GPa before and after heating to 2000K. Rhodochrosite peaks marked in pink

Figure 5.4 Diffraction pattern of manganese and CO_2 reactions after heating with caked diffraction image in background. Diffraction positions for manganese metal in blue and for rhodochrosite in pink.
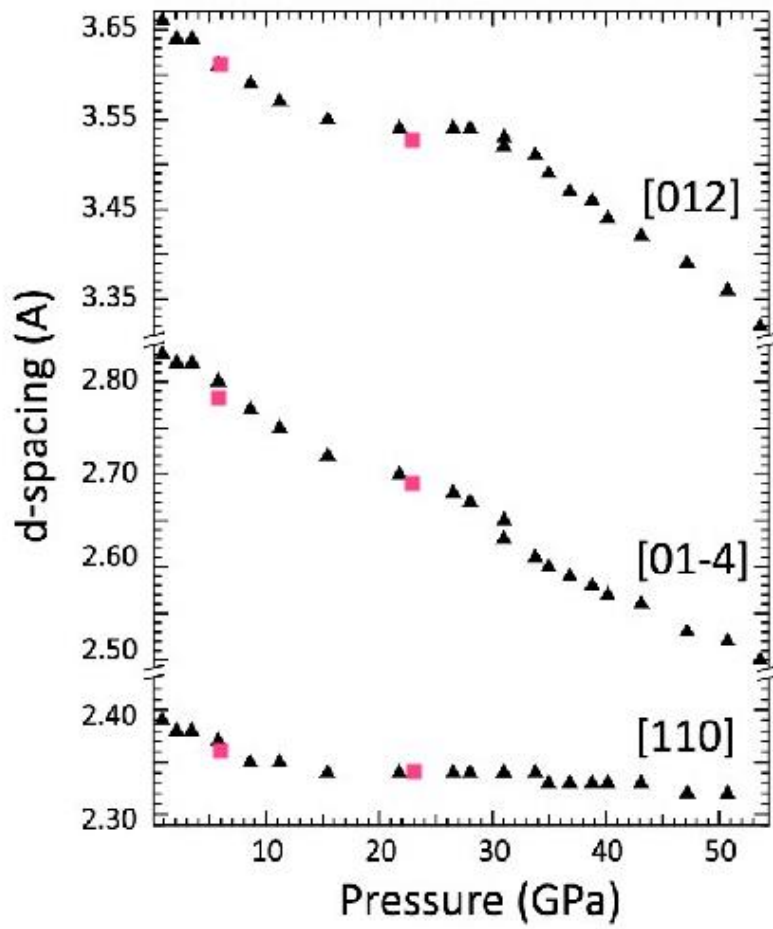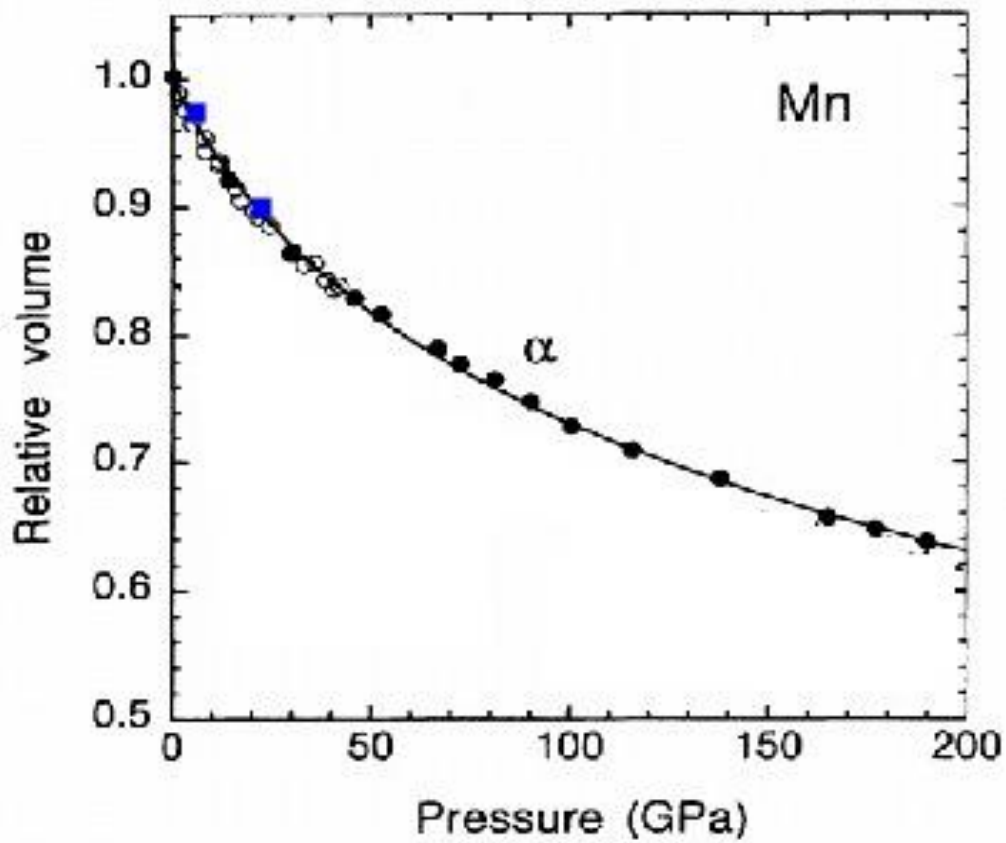
Figure 5.5 d-spacing as a function of pressure for three lattice planes of rhodochrosite. Modified from Farfan et al., (2013). Farfan's data in black, data from this study in pink

Figure 5.6 Relative volume as a function of pressure for manganese metal. Modified from Fujihisa and Takemura (1995). Fujihisa and Takemura data in black, data from this study in blue

Figure 5.7 Manganese and CO_2 at 44 GPa before and after heating to 2500K. Rhodochrosite peaks marked in pink

Figure 5.8 Manganese and CO_2 at 44 GPa after heating with caked diffraction image in the background. Manganese metal peak positions marked in blue and rhodochrosite peak positions marked in pink
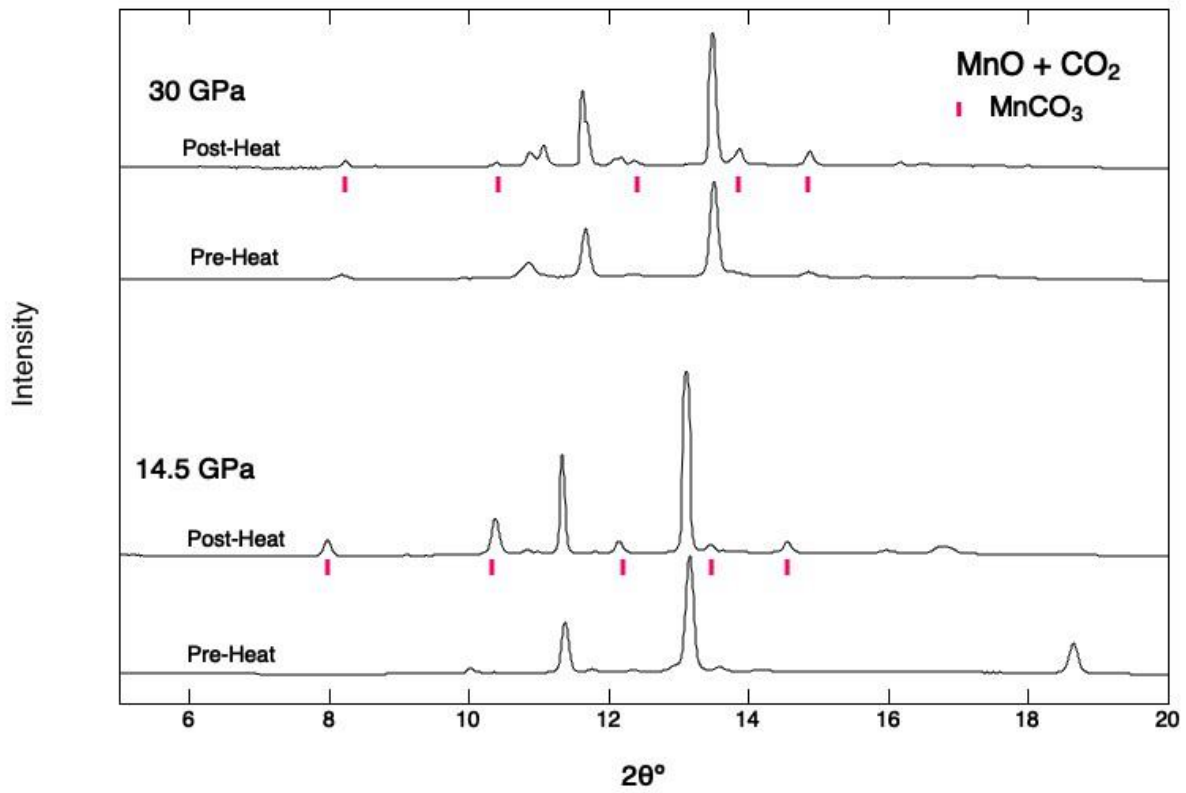
Figure 5.9 Manganese Oxide (manganosite) and CO_2 at 14.5 and 30 GPa before and after heating to 2500K. Reaction product, Rhodochrosite, peaks marked in pink
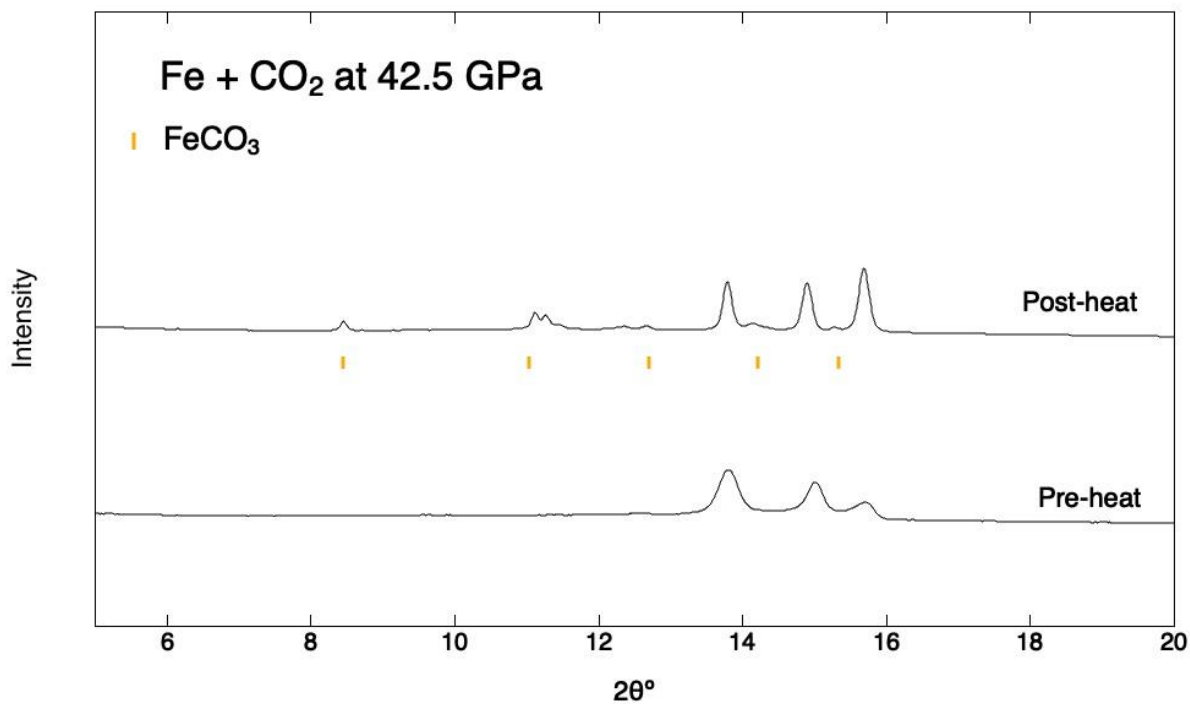
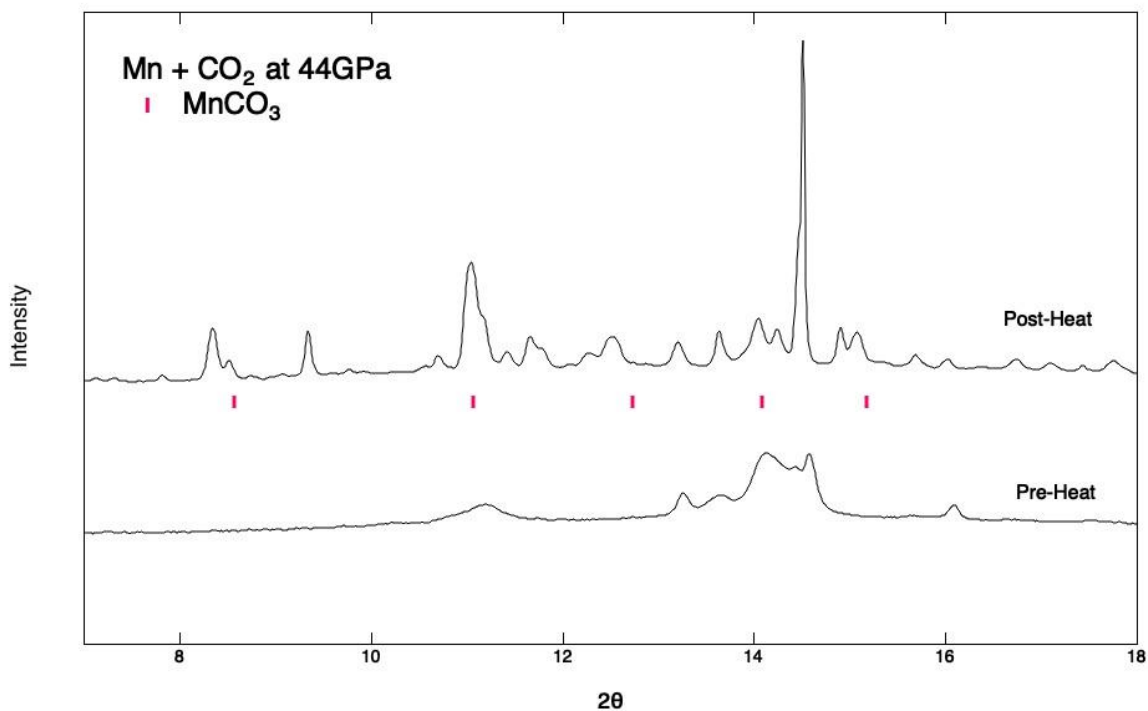**Figure 5.10** Iron and CO_2 at 42.5 GPa before and after heating to 2500K. Siderite peaks marked in yellow
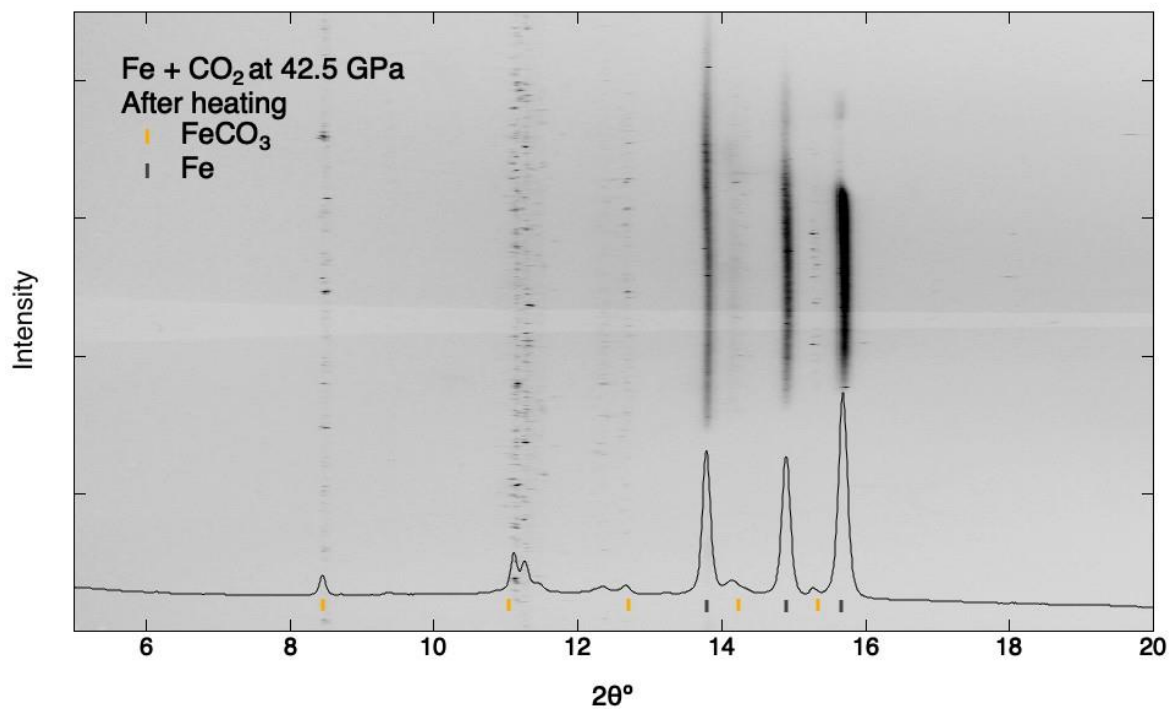
Figure 5.11 Diffraction pattern of iron and CO_2 reactions after heating with caked diffraction image in background. Diffraction positions for iron metal in gray and for siderite in yellow
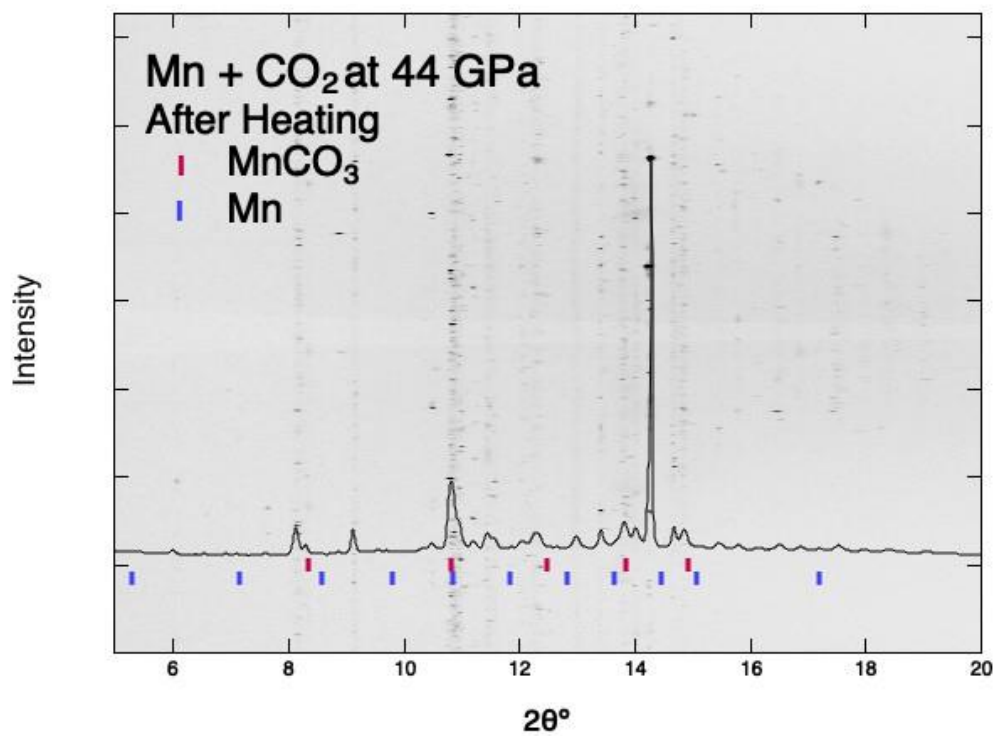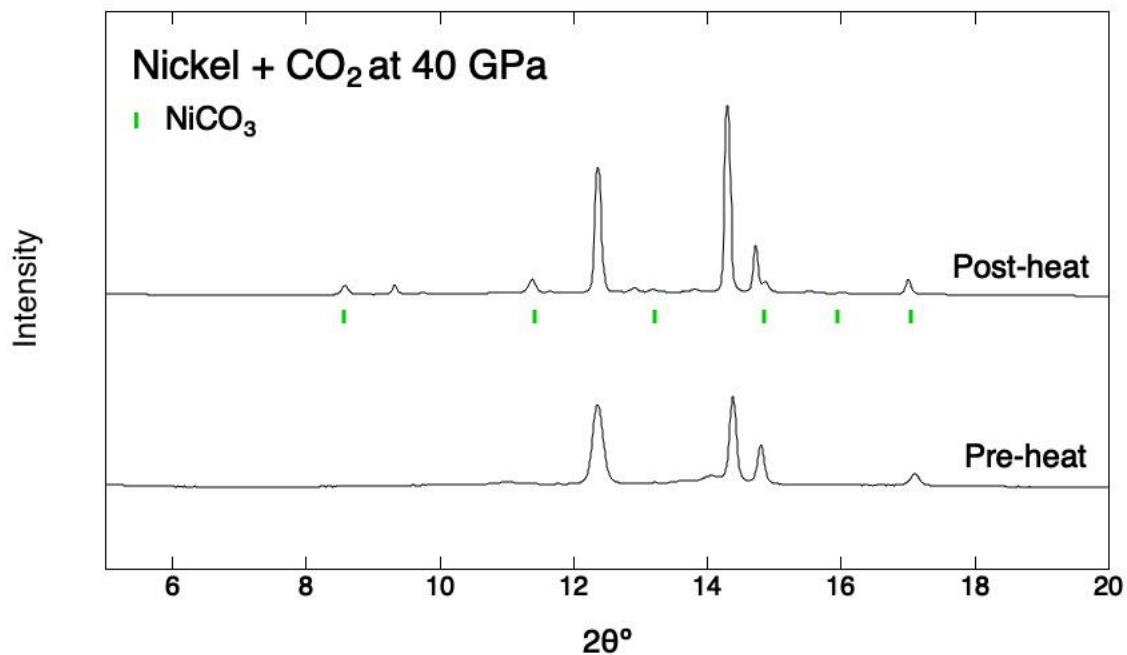
Figure 5.12 Nickel and CO_2 at 40 GPa before and after heating to 2500K. Gaspéite peaks marked in green
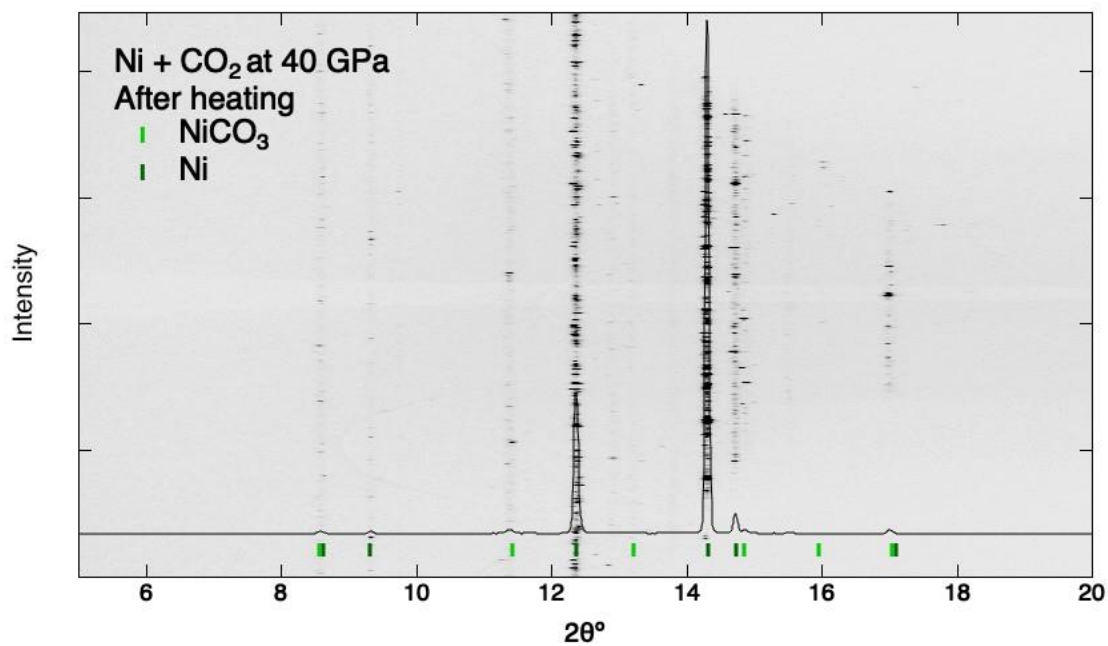
Figure 5.13 Diffraction pattern of nickel and CO_2 reactions after heating with caked diffraction image in background. Diffraction positions for nickel metal in dark green and for gaspéite in light green

5.5 References

Boulard E, Liu Y, Koh AL, Reagan M, Stodolna J, Morad G, Mezouar M, Mao WL (2016)

Transformations and Decomposition of $MnCO_3$ at Earth's Lower Mantle Conditions.

Frontiers in Earth Sciences 4:107, doi: 10.3389/feart.2016.00107

Dasgupta R, (2013) Ingassing, storage, and outgassing of terrestrial carbon through geologic

time. *Reviews in Mineralogy and Geochemistry*, vol. 77, pp. 183-229

Dasgupta R and Hirschmann M (2006) Melting in the Earth's deep upper mantle caused by

carbon dioxide. *Nature,* 440, 659-662

Dasgupta R, Hirschmann MM (2010) The deep carbon cycle and melting in Earth's interior.

Earth and Planetary Science Letters 298: 1-13

Farfan GA, Boulard E, Wang S, Mao WL (2013). Bonding and electronic changes in

rhodochrosite at high pressure. American Mineralogist. Volume 98, pp. 1817-1823.

Farfan G, Wang S, Ma H, Caracas R, Mao W (2012) Bonding and structural changes in siderite

at high pressure. *American Mineralogist*, vol. 97, pp. 1421-1426

Fujihisa H and Takemura K (1995). Stability and Equation of State of α-manganese Under

Ultrahigh Pressure. *Physical Review B*. Volume 52 issue 18, pp. 257-260.

Kaminsky FV, Wirth R (2011). Iron carbide inclusions in lower-mantle diamond from Juina,

Brazil. *The Canadian Mineralogist*, 49, 2, 555-572, DOI: 10.3749/canmin.49.2.555

Kelemen P and Manning C (2015). Reevaluating carbon fluxes in subduction zones, what goes

down, mostly comes up. *Proceedings of the National Academy of Sciences* 112 (30)

E3997-E4006, https://doi.org/10.1073/pnas.1507889112

Kunz M, Yan J, Cornell E, Domning EE, Yen CE, Doran A, Beavers CM, Treger A, Williams Q,

MacDowell AA (2018) Implementation and application of the peak scaling method for

temperature measurement in the laser heated diamond anvil cell. *Reviews of Scientific Instruments*, 89, 083903

Liu C, Cundari TR, Wilson A (2012) CO_2 reduction on transition metals (Fe, Co, Ni, and Cu) surfaces: in comparison with homogeneous catalysis. *Journal of Physics and Chemistry C*, 116, 9, 5681-5688

Logvinova A, Shatskiy A, Wirth R, Tomilenko AA (2019) Carbonatite melt in type IA gem diamond. *Lithos*, 342-343:463-467, 10.1016/j.lithos.2019.06.010

Mao HK, Xu J, Bell PM (1986) Calibration of the ruby pressure gauge to 800 kbar under quasi-hydrostatic conditions. *J Geophys Res* 91: 4673-4676

McCammon C (2005) The paradox of mantle redox. *Science*, vol. 308, pp. 807-808

Persson E and Ohman E (1929) A high-temperature modification of manganese. *Nature* 124, 333-334

Prescher C, Prakapenka VB (2015) DIOPTAS: a program for reduction of two-dimensional X-ray diffraction data and data exploration. *High Press. Res*. 35:3, 223–230

Rainey ESG and Kavner A (2014) Peak scaling method to measure temperatures in the laser-heated diamond anvil cell and applications to the thermal conductivity of MgO. *Journal of Geophysical Research: Solid Earth*, 119, 8154-8170

Rapoport E and Kennedy G (1966) Phase Diagram of Manganese to 40 kbars. *Journal of Physics and Chemistry of Solids,* vol. 27, pp. 93-98

Santamaria-Perez D, McGuire C, Makhluf A, Kavner A, Chulia-Jordan R, Pellicer-Porres J, Martinez-Garcia D, Doran A, Kunz M, Rodriguez-Hernandez P, Munoz A (2016) Exploring the chemical reactivity between carbon dioxide and three transition metals

(Au, Pt, Re) at high-pressure, high-temperature conditions. *Inorganic Chemistry*, 55, 10793-10799

Sawchuk K, Kamat R, McGuire C, Kavner K (2021) An x-ray diffraction and Raman spectroscopic study of the high-pressure behavior of gaspéite ($Ni_{0.73}Mg_{0.27}CO_3$). *Physics and Chemistry of Minerals*, 48, 7

Solymosi F, (1991) The bonding and structure and reactions of CO_2 absorbed on clean and promoted metals surfaces. *Journal of Molecular Catalysis*, 65, 337-358

Wirth R, Kaminsky F, Matsyuk S, Schreiber A (2009) Unusual micro- and nano- inclusions in diamonds from the Juina area, Brazil. *Earth and Planetary Science Letters* 289, 292-30, doi:10.1016/j.epsl.2009.06.043

Chapter 6 - Conclusions

6.1 Overview

The phase stabilities of volatile-bearing minerals has important implications for the deep Earth chemical system. In this dissertation, I study the behavior and reactions of several carbon- and sulfur-bearing species at deep Earth conditions. I utilize X-ray diffraction, Raman spectroscopy, and infrared spectroscopy techniques to probe the behavior of minerals at high pressures and temperatures. I calculate equations of state, which yield values for bulk modulus, its pressure derivative, and Grüneisen parameters for individual mineral phases. Additionally, I present a series of pioneering experiments that study relative phase stability between carbonates and oxides. Together, this work aids in our understanding of volatile storage in mineral phases at mantle conditions.

The work on the lead sulfate anglesite ($PbSO_4$) produced the most comprehensive high-pressure data set on this mineral to date. Using infrared and Raman spectroscopy in Chapter 2, we observe complex structural evolution with increasing pressure. This evolution includes a kinetically impeded phase transition beginning at 21 GPa, during which the low and high-pressure phases coexist over a large pressure range before the high-pressure phase becomes dominant around 40 GPa. Using X-ray diffraction in Chapter 3, we determine the high-pressure structure to be the $P2_12_12_1$, consistent with previous observations for anglesite and other sulfates. Additionally, we calculate equations of state yielding values of $K_{0T} = 63(3)$ GPa and $K' = 5.9(3)$ for the low pressure phase and $K_{0T} = 67(4)$ GPa and $K' = 4.9(4)$ for the high-pressure phase.

The study on the nickel carbonate, gaspéite ($NiCO_3$), provided insight into carbonate stability in the mantle. High-pressure observations using Raman spectroscopy and X-ray diffraction in Chapter 4 showed that gaspéite undergoes no phase transitions to 50 GPa.

Additionally, equation of state measurements yield values of $K_{0T} = 136(4)$ GPa and $K' = 4.6(3)$. Grüneisen parameters for each of the Raman modes yield values of $\gamma = 1.69(4)$ for the $E_g(T)$ mode, $\gamma = 1.68(3)$ for the $E_g(L)$ mode, $\gamma = 0.42(1)$ for the v_4 mode, and $\gamma = 0.4(1)$ for the v_1 mode. Comparing the behavior of gaspéite with other calcite-structured carbonates reveals an apparent trend: compressibility increases with increasing cation radius, with gaspéite being the least compressible. The addition of nickel, which has the smallest cation radius of the calcite-structured carbonates, may stabilize gaspéite at higher pressures.

The reaction experiments between carbon dioxide and transition metals introduce a new type of diamond anvil cell experiment. In these experiments, CO_2 is loaded into the diamond anvil cell with a transition metal or oxide and the sample is then heated to promote reactions. The products of these reactions inform us of relative phase stability between oxides and carbonates. Reactions between manganese metal and CO_2 at a variety of mantle pressures were found to form the manganese carbonate rhodochrosite ($MnCO_3$). Follow-up studies between manganese oxide and CO_2 also created rhodochrosite. Preliminary work on iron and nickel also found these transition metals prefer to form a carbonate in the presence of CO_2 at mantle conditions. These observations suggest carbonate minerals are likely candidates for storing carbon in the mantle.

6.2 Future Work

Achieving the goal of a complete understanding of the deep Earth volatile cycles will require much more research from the mineral physics community. The work presented in this dissertation advances that goal, but also raises new questions to be answered by future work.

The studies done on anglesite provides insight into the high-pressure structure of baryte group minerals. The measurements presented in this study show that, similar to baryte, anglesite undergoes a phase transition at high pressure to the $P2_12_12_1$ structure. This raises questions about the behavior of other sulfate minerals. Of the baryte-structured sulfates, celestite ($SrSO_4$) is the only mineral that has not been reported to undergo the transition to the $P2_12_12_1$ structure. Future work on celestite may find it also undergoes this phase transition. Additionally, the coexistence of anglesite's low and high-pressure phase for a pressure range of nearly 20 GPa is of interest. This coexistence is likely caused by a kinetic hinderance. A future study should investigate this phase transition under both high pressure and high temperature. It is likely the addition of high temperatures may cause this transition to go forward more rapidly.

The experiments on gaspéite suggested the small cation radius on nickel stabilizes the calcite structure at high pressures. Other calcite-structured carbonates with small cations such as magnesite and spherocobaltite show similar behavior. Future work on other calcite-structured carbonates could prove this relationship between small cation size and high-pressure stability is true. Additionally, our study explored pressures up to 50 GPa and found no phase transitions; studies on other carbonates have found that, at high enough pressures, carbonates either break down or undergo phase transitions. Extending the pressure range beyond 50 GPa may reveal that gaspéite also becomes unstable at higher pressures. Gaspéite, having the smallest cation of all the calcite-structured carbonates, may be the most stable to highest pressures of all the similarly-structured carbonates.

Reaction experiments between carbon dioxide and transition metals show relative phase stability between different minerals at mantle conditions. This is a good first step towards creating mantle phase diagrams, however much more work is needed before that goal can be

achieved.   Systematic studies across numerous pressure steps need to be conducted in order to create phase diagrams of Earth-abundant first-row transition metals and their end-member carbonates and oxides. Ultimately, studying these phase relations will lead to a better understanding of carbon storage in the deep Earth.

The deep Earth's volatile cycle is a complex, multicomponent system. To obtain a complete understanding of it will require a formidable amount of work across many Earth science disciplines. The work presented in this dissertation progresses that goal by providing notable contributions towards our understanding of the stability, behavior, and reactions of volatiles in the deep Earth.